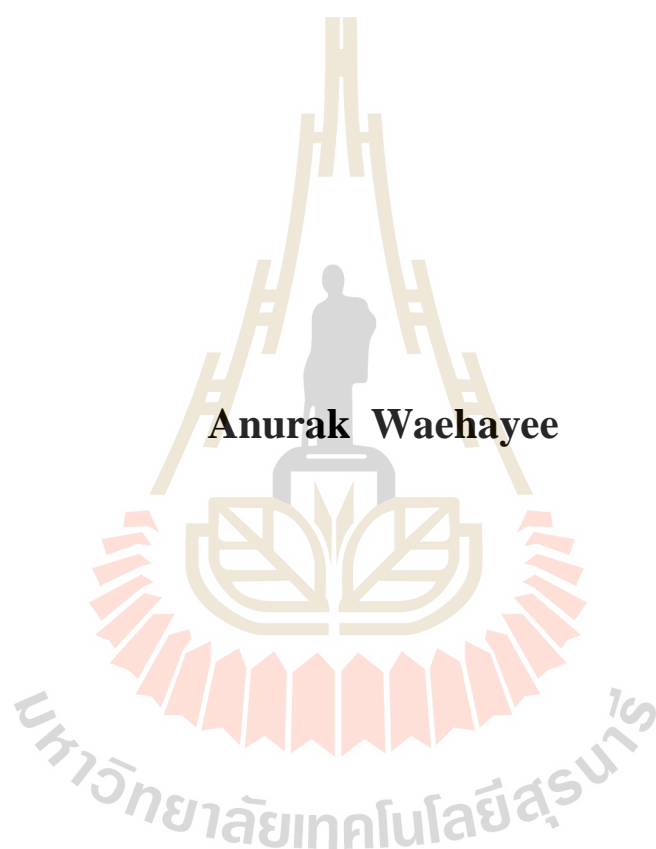


**ELECTRONIC AND PHOTOCATALYTIC PROPERTIES
OF TELLURIUM-CONTAINING PYROCHLORE
OXIDES**



**A Thesis Submitted in Partial Fulfillment of the Requirements for the
Degree of Doctor of Philosophy in Chemistry
Suranaree University of Technology
Academic Year 2018**

สมบัติทางอิเล็กทรอนิกส์และการเร่งปฏิกิริยาเชิงแสงของโฟคลดอร์ออกไซด์ที่มี
เทลลูเรียมเป็นองค์ประกอบ

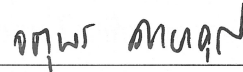


วิทยานิพนธ์นี้เป็นส่วนหนึ่งของการศึกษาตามหลักสูตรปริญญาวิทยาศาสตรดุษฎีบัณฑิต
สาขาวิชาเคมี
มหาวิทยาลัยเทคโนโลยีสุรนารี
ปีการศึกษา 2561

**ELECTRONIC AND PHOTOCATALYTIC PROPERTIES OF
TELLURIUM-CONTAINING PYROCHLORE OXIDES**

Suranaree University of Technology has approved this thesis submitted in partial fulfillment of the requirements for the Degree of Doctor of Philosophy.

Thesis Examining Committee



(Prof. Dr. Jatuporn Wittayakun)

Chairperson



(Asst. Prof. Dr. Theeranun Siritanon)

Member (Thesis Advisor)



(Assoc. Prof. Dr. Sanchai Prayoonpokarach)

Member



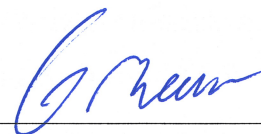
(Dr. Suwit Suthirakun)

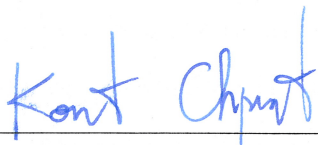
Member



(Dr. Narong Chanlek)

Member




(Assoc. Prof. Ft. Lt. Dr. Kontorn Chamniprasart)

Vice Rector for Academic Affairs
and Internationalization

(Assoc. Prof. Dr. Worawat Meevasana)

Dean of Institute of Science

อนุรักษ์ เวหะยี: สมบัติทางอิเล็กทรอนิกส์และการเร่งปฏิกิริยาเชิงแสงของไพโรคลอโรออกไซด์ที่มีเทลลูเรียมเป็นองค์ประกอบ (ELECTRONIC AND PHOTOCATALYTIC PROPERTIES OF TELLURIUM-CONTAINING PYROCHLORE OXIDES) อาจารย์ที่ปรึกษา: ผู้ช่วยศาสตราจารย์ ดร.ธีรนนท์ ศิริदानนท์, 143 หน้า.

วิทยานิพนธ์นี้มุ่งศึกษาสมบัติทางอิเล็กทรอนิกส์และการเร่งปฏิกิริยาโดยใช้แสงของสารประกอบไพโรคลอโรออกไซด์ที่มีเทลลูเรียมเป็นองค์ประกอบ โดยศึกษาสารประกอบสามกลุ่ม ได้แก่ สารประกอบซีเซียมอะลูมิเนียมเทลลูเรตที่เจือด้วยธาตุรูบิเดียมและโพแทสเซียม สารประกอบซีเซียมเทลลูเรตที่เจือด้วยธาตุแมงกานีส และสารประกอบโพแทสเซียมไนโอเบียมเทลลูเรตที่เจือด้วยธาตุเงิน ทองแดง และดีบุก

สารประกอบซีเซียมอะลูมิเนียมเทลลูเรตที่เจือด้วยธาตุรูบิเดียม และโพแทสเซียมได้ถูกสังเคราะห์ขึ้นด้วยวิธีปฏิกิริยาสถานะของแข็ง ถึงแม้ว่าการแทนที่ ซีเซียมด้วยรูบิเดียมและโพแทสเซียม จะส่งผลให้ขนาดของเซลล์พารามิเตอร์เล็กลงก็ตาม แต่ค่าสภาพต้านทานไฟฟ้ากลับเพิ่มขึ้น การตรวจสอบอย่างละเอียดได้นำไปสู่ความเข้าใจถึงแบบจำลองแถบพลังงานได้มากขึ้น การวิเคราะห์ด้วยเทคนิคสเปกโตรสโกปีโฟโตอิเล็กตรอนด้วยรังสีเอกซ์ ยืนยันว่าตัวอย่างทั้งหมดประกอบด้วยเทลลูเรียมที่ผสมระหว่าง Te^{6+} และ Te^{4+} ซึ่งเป็นจุดกำเนิดของการเป็นสารกึ่งตัวนำชนิดเอ็น ค่าการนำไฟฟ้านั้นขึ้นอยู่กับระยะห่างระหว่างระดับพลังงานของอิเล็กตรอน $5s^2$ ของ Te^{4+} และขอบล่างของแถบการนำไฟฟ้า การมีรูบิเดียมและโพแทสเซียมในโครงสร้างส่งผลให้เกิดความแตกต่างของการนำไฟฟ้า เนื่องจากจะเพิ่มขนาดช่องว่างแถบพลังงาน และขยับขอบล่างของแถบการนำไฟฟ้าขึ้น

สารประกอบซีเซียมเทลลูเรตที่เจือด้วยธาตุแมงกานีส ได้ถูกสังเคราะห์ขึ้นด้วยวิธีปฏิกิริยาสถานะของแข็ง เป็นที่น่าสนใจว่ามีกลไกการทดแทนสองแบบเกิดขึ้น ขึ้นอยู่กับปริมาณของการเจือแมงกานีส การเปลี่ยนกลไกการทดแทนนี้ส่งผลให้การเปลี่ยนแปลงอย่างฉับพลันของแนวโน้มเซลล์พารามิเตอร์และพลังงานกระตุ้นของการนำไฟฟ้า จากผลการทดลองและผลการคำนวณทางทฤษฎีฟังก์ชันนอลความหนาแน่น แสดงให้เห็นว่าสำหรับในสารประกอบซีเซียมเทลลูเรตที่เจือด้วยธาตุแมงกานีสน้อยกว่า 0.33 ($Mn_{0.05-0.3}$) $Te 5s$ ของเทลลูเรียมซ้อนทับกับออร์บิทัล $Mn 3d$ และ $O 2p$ จึงกลายเป็นส่วนหนึ่งของแถบเวเลนซ์ นอกจากนี้ยังพบว่าขนาดของเซลล์พารามิเตอร์มีความสัมพันธ์กับระดับพลังงานที่ต่างกันระหว่างออร์บิทัล $5s^2$ ของเทลลูเรียมและขอบล่างของแถบการนำไฟฟ้า ในขณะที่สารประกอบซีเซียมเทลลูเรตที่เจือด้วยธาตุแมงกานีสถึง 0.33 ($Mn_{0.33}$) ส่งผล

ให้ Te^{4+} หายไป และระดับพลังงานของแถบการนำไฟฟ้าขยับขึ้น จึงเป็นจุดที่เกิดการเปลี่ยนแปลงแนวโน้มของการนำไฟฟ้า ถึงแม้ว่าระดับพลังงานของขอบบนสุดของแถบเวเลนซ์จะขยับขึ้นในสารประกอบซีเซียมเทลลูเรตที่เจือด้วยธาตุแมงกานีสมากกว่า 0.33 ($\text{Mn}_{0.37-0.43}$) เนื่องจากช่องว่างอะตอมออกซิเจนในโครงผลึก ก็ไม่สามารถปรับปรุงค่าการนำไฟฟ้าให้ดีขึ้นได้ จากผลดังกล่าวข้างต้นส่งผลให้สารประกอบซีเซียมเทลลูเรตที่เจือด้วยธาตุแมงกานีสเป็นสารกึ่งตัวนำบริสุทธิ์

ธาตุเงิน ทองแดง และดีบุกถูกเจือในสารประกอบโพแทสเซียมไนโอเบียมเทลลูเรตเพื่อให้เกิดการเปลี่ยนแปลงขนาดช่องว่างของแถบพลังงาน ในขณะที่การเจือทำได้ด้วยวิธีการแลกเปลี่ยนไอออนอย่างง่าย สารประกอบโพแทสเซียมไนโอเบียมเทลลูเรตถูกสังเคราะห์ขึ้นด้วยวิธีปฏิกิริยาสถานะของแข็ง การลดลงของขนาดช่องว่างระหว่างแถบพลังงานนี้เป็นสาเหตุมาจากเกิดการมีส่วนร่วมของออร์บิทัล $4d$ $3d$ และ $5s$ ของ ธาตุเงิน ทองแดง และดีบุก ตามลำดับ ส่งผลให้ระดับขอบบนสุดของแถบเวเลนซ์ขยับขึ้น จากผลดังกล่าวส่งผลให้สารประกอบโพแทสเซียมไนโอเบียมเทลลูเรตที่ถูกเจือด้วยธาตุทองแดง เงิน และดีบุก แสดงประสิทธิภาพในการเป็นตัวเร่งปฏิกิริยาโดยใช้แสงที่ดีกว่าสารประกอบโพแทสเซียมไนโอเบียมเทลลูเรตตามลำดับ เนื่องจากตัวเร่งปฏิกิริยาที่มีขนาดช่องว่างระหว่างแถบพลังงานที่แคบและดูดกลืนแสงช่วงวิสิเบิลได้ดีนั้น สามารถกระตุ้นให้เกิดอิเล็กตรอนในแถบการนำไฟฟ้า และโฮลในแถบเวเลนซ์ได้ง่าย จึงนำไปสู่การสร้าง โมเลกุลที่ไวต่อการเกิดปฏิกิริยาการสลายสีย้อมได้มากขึ้น



สาขาวิชาเคมี

ปีการศึกษา 2561

ลายมือชื่อนักศึกษา อนุรักษ์ แจน:ย์

ลายมือชื่ออาจารย์ที่ปรึกษา อ.ดร.ศิริพร พันธ์

ANURAK WAEHAYEE : ELECTRONIC AND PHOTOCATALYTIC
PROPERTIES OF TELLURIUM-CONTAINING PYROCHLORE OXIDES.
THESIS ADVISOR : ASST. PROF. THEERANUN SIRTANON, Ph.D.
143 PP.

DEFACE PYROCHLOER OXIDES/ELECTRON PROPERTY /BAND
STRUCTURE/PHOTOCATALYST

This thesis focuses on the electronic and photocatalytic properties of tellurium-containing pyrochlore oxides, including (Rb and K)-doped $\text{CsAl}_{0.33}\text{Te}_{1.67}\text{O}_6$, Mn-doped CsTe_2O_6 , and (Ag, Cu, and Sn)-doped KNbTeO_6 .

$\text{Cs}_{1-x}\text{A}_x\text{Al}_{0.33}\text{Te}_{1.67}\text{O}_6$ (A= Rb and K, $x = 0-1$) were successfully synthesized by solid-state reactions. Although replacing Cs with Rb and K results in smaller cell parameters, electrical resistivity decreased. Detailed investigations have led to more understanding of the band structure. X-ray photoelectron spectroscopy (XPS) confirms that all samples contain $\text{Te}^{4+}/\text{Te}^{6+}$ mixed valency which is the origin of their *n*-type conduction. The conductivities were determined by the energy difference between the defect levels originated from Te^{4+} and the bottom of the conduction band. The differences in electronic conductivity are affected by Rb and K content in the structure as they seem to increase the band gap energy and valence band minimum.

$\text{CsMn}_x\text{Te}_{2-x}\text{O}_6$ defect pyrochlore structure were successfully synthesized by solid-state method with $x=0.05-0.43$. Interestingly, there are two substitution schemes depending on the *x* values. The switch between the two schemes results in a sudden change in the cell parameter trend and the activation energy of conduction. Based on

the results from the experiments and the density functional theory calculation, Te 5s states overlap with Mn 3d-O 2p states and become part of the valence band in compounds with $x < 0.33$. In addition, it was found that the unit cell parameters correlate with the energy difference between Te 5s states and conduction band minimum. On the other hand, the disappearance of Te⁴⁺ and lifting of conduction band minimum in the samples with $x \geq 0.33$ cause the switching of activation energy. Although valence band maximum of samples with $x > 0.33$ is raised because of the oxygen vacancies, the conductivities are not improved. As a result, the CsMn_xTe_{2-x}O₆ compounds are considered intrinsic semiconductors.

Ag⁺, Cu²⁺, and Sn²⁺ are substituted in K site of KNbTeO₆ compounds to modify the band gap energy by facile ion exchange method. The KNbTeO₆ parent compound has been successfully prepared by solid state method. The reduction of band gap energy from 3.38 eV in KNbTeO₆ to 2.76 (Ag-doped), 3.21 (Cu-doped), and 2.51 eV (Sn-doped) are attributed to the shift of valence band maximum caused by the additional contribution of Ag 4d, Cu 3d, and Sn 5s states in doped samples. As a result, the Cu²⁺, Ag⁺, and Sn²⁺-doped KNbTeO₆ exhibited higher photocatalytic activity than pure KNbTeO₆ respectively. Because the catalysts have the narrower band gap energy and the stronger light absorption in visible region, they can generate more photoexcited electron-hole pairs and produces higher active species.

School of Chemistry

Academic Year 2018

Student's Signature อรุณรัตน์ วรรณวิทย์

Advisor's Signature อศรินทร์ ศิริสมาน

ACKNOWLEDGEMENTS

I would like to express my sincere thanks to several people who help me to complete my thesis and thereby allowing me to reach my goal of achieving a Ph.D.

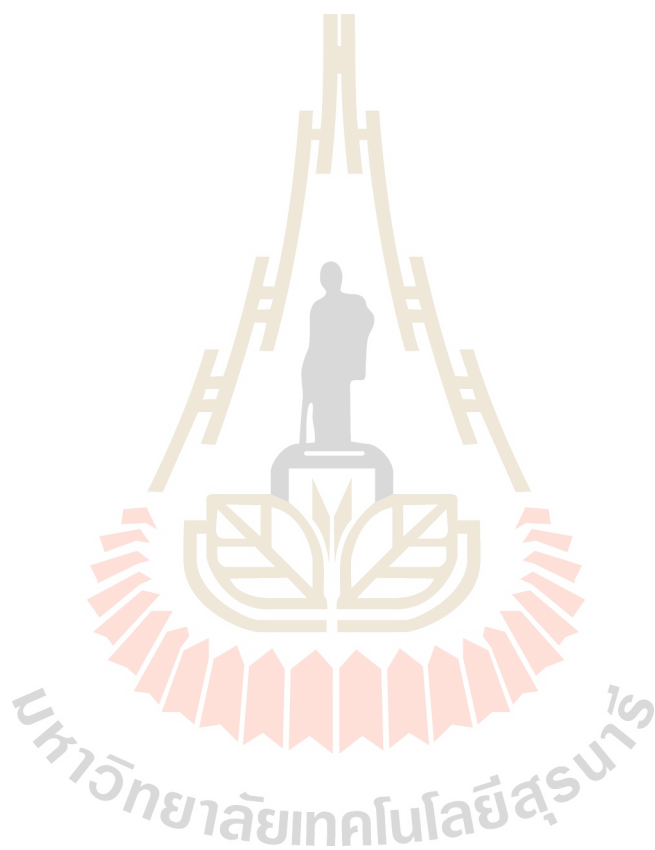
First of all, I would like to thank my thesis advisor, Asst. Prof. Dr. Theeranun Siritanon, for giving me a chance to study at SUT and do interesting research topic. Under her supervision, she was kindly advising and helping me along with my thesis. I appreciate her kind support, suggestion, encouragement and discussion throughout my thesis.

I am thankful to Dr. Suwit Suthirakul, Mr. Thanundorn Kongnok, and Assoc. Prof. Dr. Sirichok Jungthawan for their valuable time on the calculations for my work and kind suggestions. I also would like to acknowledge Dr. Tanachat Eknapakul for teaching me about electronic structure investigation by photoelectron spectroscopy techniques.

I would like to thank people from the School of Chemistry, the School of Physics, the Center for Scientific and Technological Equipment (CSTE), and the Synchrotron Light Research Institute (SLRI). Their help and support for characterization equipment allow my work complete. Particularly, I am grateful to colleagues from solid-state chemistry and hydrogen storage research group at SUT: Arreerat Jiamprasertboon, Nararat Yong, Praphaiphon Pornsuksawang, Sophida Thiangviriya, etc. Their assistance and friendship were really precious.

Last, but not least, I would like to thank my family for their love, support, encouragement, and understanding during my study.

Anurak Wachayee



CONTENTS

	Page
ABSTRACT IN THAI	I
ABSTRACT IN ENGLISH	III
ACKNOWLEDGEMENTS	V
CONTENTS	VI
LIST OF FIGURES	X
LIST OF TABLES	XV
CHAPTER	
I INTRODUCTION	1
1.1 Significance of the study.....	1
1.2 Background.....	2
1.2.1 The structure of defect pyrochlore oxides.....	3
1.2.2 Classification of mixed valence compounds.....	4
1.2.3 Band structure and electronic properties.....	7
1.2.4 Interactions between UV-Visible light and solids.....	13
1.2.5 X-Ray absorption spectroscopy of 3d transition metals.....	15
1.2.6 Oxygen 1s X-Ray absorption spectroscopy.....	18
1.2.7 Photoelectron spectra at valence band.....	19
1.2.9 Photocatalysis	20
1.3 References	24

CONTENTS (Continued)

		Page
IV	ELECTRONIC BAND STRUCTURE AND CONDUCTION MECHANISM OF CsMn_xTe_{2-x}O₆ MIXED VALENCE CUBIC PYROCHLORES	67
4.1	Abstract.....	67
4.2	Introduction	68
4.3	Experiments.....	70
4.3.1	Preparation of CsMn _x Te _{2-x} O ₆	70
4.3.2	Characterizations	70
4.4	Calculations	71
4.5	Results and discussion	72
4.5.1	Crystal structure	72
4.5.2	X-ray absorption near edge structure (XANES) results.....	74
4.5.3	X-ray photoelectron spectroscopy (XPS) results.....	78
4.5.4	Electrical properties.....	80
4.5.5	Electronic structure.....	81
4.5.6	Band structure	84
4.6	Conclusion.....	88
4.7	References.....	89
V	ENHANCEMENT PHOTOCATALYTIC ACTIVITY OF KNbTeO₆ DEFECT PYROCHLORE THROUGH BAND ENGINEERING	96
5.1	Abstract.....	96

LIST OF FIGURES

Figure	Page
1.1 The crystal structures of general pyrochlore (a) and defect pyrochlor (b)	4
1.2 The coordination around the Ga(III) and (b) Ga(I) (a) ion in GaCl ₂	5
1.3 Crystal structure of (C ₃ H ₇ NH ₃) ₄ SbCl ₆ (Cl) ₂	6
1.4 Crystal structure of Ba _{1-x} K _x BiO ₃	7
1.5 The band structure of insulators.....	8
1.6 The band structure of metals.....	9
1.7 Variation in electrical conductivity with temperature for some metals	9
1.8 The band structure of an intrinsic semiconductor.....	10
1.9 The Arrhenius plot of the electrical conductivity for an intrinsic semiconductor	11
1.10 Energy band structures of <i>n</i> -(a) and <i>p</i> -type (b) semiconductor	12
1.11 Arrhenius plots of electrical conductivity for <i>n</i> -(a) and <i>p</i> -type (b) semiconductor	12
1.12 The interactions between the incident light and solids.....	14
1.13 Absorption (a) and Spontaneous emission (b) of light radiation.....	15
1.14 The energy level diagram for <i>K</i> -edge and <i>L</i> _{3,2} -edge transitions of <i>3d</i> transition metals.....	16
1.15 The <i>2p</i> core level XAS spectra for of some <i>3d</i> transition metal oxides (a). The Ti <i>L</i> _{3,2} -edge XAS spectra of V doped LiTi ₂ O ₄ compare with TiO ₂ (Anatase) and Ti ₂ O ₃ as reference spectra (b)	17

LIST OF FIGURES (Continued)

Figure	Page
1.16 Oxygen 1s X-ray absorption edge spectra of 3d transition metal oxides.....	18
1.17 Schematic of photoelectron process	20
1.18 A schematic diagram of a photocatalytic process.....	21
1.19 Scheme for the band structures of common photocatalysts, and potentials of the radical generation	24
2.1 Structure of CsTe ₂ O ₆ (a) and Cs(M,Te) ₂ O ₆ (b)	31
2.2 Band structure of CsTe ₂ O ₆ (a) and cubic Cs(M,Te) ₂ O ₆ pyrochlores (b)	33
2.3 Schematic diagram of energy band structure of KSTO, SnSTO and AgSTO.....	35
2.4 Schematic representation of photocatalytic mechanism of MV over ATTO catalyst.....	36
3.1 XRD patterns of Cs _{1-x} Rb _x Al _{0.33} Te _{1.67} O ₆ and Cs _{1-x} K _x Al _{0.33} Te _{1.67} O ₆	46
3.2 Plots of cell parameters versus Rb and K content	47
3.3 XPS survey spectra of CATO, RATO, and KATO	49
3.4 Cs 3d, Rb 3d, K 2p and Al 1s XPS spectra of Cs _{1-x} Rb _x Al _{0.33} Te _{1.67} O ₆ and Cs _{1-x} K _x Al _{0.33} Te _{1.67} O ₆	50
3.5 XPS Te 3d spectra of CATO, RATO, KATO and CTO	50
3.6 XPS valence band spectra of CsTe ₂ O ₆ and AAl _{0.33} Te _{1.67} O ₆ (A = Cs, Rb, and K) (a) and the close-up of Cs containing samples showing an additional small peak near the Fermi level (b)	53
3.7 The calculated valence band of CsTe ₂ O ₆	54

LIST OF FIGURES (Continued)

Figure	Page
3.8	UV-Vis spectra (a) and extrapolation of the band gap energy (b) of CsTe ₂ O ₆ and AAl _{0.33} Te _{1.67} O ₆ (A = Cs, Rb, and K) 55
3.9	Electronic conductivity of Cs _{1-x} A _x Al _{0.33} Te _{1.67} O ₆ (A = Rb and K) and CsTe ₂ O ₆ samples fitted with Arrhenius equation 57
3.10	Schematic band structures of CsTe ₂ O ₆ and AAl _{0.33} Te _{1.67} O ₆ (A = Cs, Rb, and K) 59
4.1	Powder X-ray diffraction patterns of CsMn _x Te _{2-x} O ₆ 73
4.2	Changes of cell parameters with Mn content..... 74
4.3	Mn L _{3,2} -edge XANES spectra of CsMn _x Te _{2-x} O ₆ 75
4.4	Te L ₃ -edge XANES (a), 1 st derivative spectra (b), and a calibration curve used to estimate average oxidation state (c) of Te in CsMn _x Te _{2-x} O ₆ 76
4.5	XPS survey spectra of CsMn _x Te _{2-x} O ₆ 79
4.6	Cs 3d (a) and (a) O 1s (b) XPS spectra of CsMn _x Te _{2-x} O ₆ 79
4.7	Arrhenius plots of electronic conductivities (a) and the obtained activation energy of conduction (b) 81
4.8	Valence band XPS (a) and XPS close-up near E _F (b) of CsMn _x Te _{2-x} O ₆ 83
4.9	O K-edge spectra (d) and first derivatives (b) of CsMn _x Te _{2-x} O ₆ 83
4.10	Calculated PDOS of the CsMn _{0.25} Te _{1.75} O ₆ system. The energy of the PDOS are plotted with relative to the Fermi energy 84
4.11	The proposed schematic band structures of CsMn _x Te _{2-x} O ₆ comparing CsTe ₂ O ₆ and CsAl _{0.33} Te _{1.67} O ₆ 86

LIST OF FIGURES (Continued)

Figure	Page
4.12	Plots of cell parameters versus activation energy of $\text{CsAl}_{0.33}\text{Te}_{1.67}\text{O}_6$ and $\text{CsMn}_x\text{Te}_{2-x}\text{O}_6$ ($x=0.05-0.33$) 87
5.1	Powder X-ray diffraction patterns of KNTO, AgKNTO, CuKNTO, and SnKNTO..... 102
5.2	The TGA profiles of KNTO, AgKNTO, CuKNTO, and SNKNTO 103
5.3	SEM mages of KNTO (a), AgKNTO (b), CuKNTO (c), and SnKNTO (d) 104
5.4	The energy dispersive X-ray spectroscopy (EDS) elemental mapping images of KNTO, AgKNTO, CuKNTO, and SnKNTO 104
5.5	Survey XPS spectra of KNTO, AgKNTO, CuKNTO, and SNKNTO 105
5.6	K $2p$ (a) and Ag $3d$, Cu $2p$ and Sn $3d$ (b) XPS spectra of KNTO, AgKNTO, CuKNTO, and SNKNTO 106
5.7	Nb $3d$ (a) and Te $3d$ (b) XPS spectra of KNTO, AgKNTO, CuKNTO, and SNKNTO..... 107
5.8	O $1s$ XPS spectra of KNTO, AgKNTO, CuKNTO, and SNKNTO 108
5.9	XPS at Valence band of KNTO, AgKNTO, CuKNTO, and SnKNTO..... 109
5.10	UV-Vis absorption spectra (a), samples color (insert), and Kubelka-Munk plot (b) of KNTO, AgKNTO, CuKNTO, and SnKNTO..... 110
5.11	The photocatalytic activity (a) and the percentage MB degradation after 3 h of UV-Visible light irradiation (b) of KNTO, AgKNTO, CuKNTO, and SnKNTO..... 111

LIST OF FIGURES (Continued)

Figure	Page
5.12 Kinetics plot for MB photodegradation in the presence of KNTO, AgKNTO, CuKNTO, and SnKNTO	112
5.13 Fluorescence spectral of TAOH with visible light irradiated KNTO, AgKNTO, CuKNTO, and SnKNTO suspensions for 3 h of irradiation time ($\lambda_{\text{Ex}} = 315 \text{ nm}$)	114
5.14 The photocatalytic degradation of MB over SnKNTO in the presence of different scavengers	115
5.15 The proposed band potential and mechanism of MB photodegradation over SnKNTO photocatalyst.....	117

LIST OF TABLES

Tables	Page
1.1 Classification of mixed valence compounds.....	7
2.1 The crystallographic site of Te and M in CsTe_2O_6 and $\text{Cs}(\text{M},\text{Te})_2\text{O}_6$	30
2.2 List of Te-containing defect pyrochlores used as photocatalysts for dye degradation.....	37
3.1 Te $3d_{5/2}$ fitting results	51
3.2 Activation energy and R^2 obtained from fitting the electronic conductivity of $\text{Cs}_{1-x}\text{A}_x\text{Al}_{0.33}\text{Te}_{1.67}\text{O}_6$; A = Rb and K and CsTe_2O_6 with Arrhenius equation	57
4.1 Estimated Te^{4+} and Te^{6+} content in $\text{CsMn}_x\text{Te}_{2-x}\text{O}_6$ samples.....	77
5.1 Cell parameter (a) and elemental composition of all compounds	102
5.2 The apparent pseudo first order rate constant (k_{app}), half-life time ($t_{1/2}$) and correlation coefficient (R^2) of KNTO, AgKNTO, CuKNTO, and SnKNTO.....	112

CHAPTER I

INTRODUCTION

1.1 Significance of the study

Oxides are the major family of solid state materials that play important roles in human's lives. At present, several oxide materials have been discovered. They are studied to be used for a wide range of applications such as energy storage, magnetic spintronic, piezoelectric, dielectric and thermoelectrics. Nowadays, many new electronic devices are created to meet the needs of the populations. In such devices, materials with specific properties are required. This research focuses on the electronic and photocatalytic properties, both of which are crucial in many applications.

Many modern electronic devices and applications demand materials with good electrical properties. High electronic conduction obtained from the n-type doping in post-transition metal oxides such as In_2O_3 , SnO_2 , and ZnSnO_3 (Alsac et al., 2013; Cai et al., 2016; Chen et al., 2013) allow them to be widely used. According to Robin and Day classification (Robin and Day, 1968), these materials can be classified as a type III mixed valence compounds which contain two indistinguishable valences resulting in a metallic conduction. While similar materials are known for many of the post transition elements, examples are rare for tellurium. In fact, most of tellurium mixed valence compounds are type I as Te^{4+} and Te^{6+} are in different sites, which results in an insulating property. On the other hand, CsTe_2O_6 contains both Te^{4+} and Te^{6+} in similar, but distinguishable sites, thus it is a type II Te mixed valence oxide. Recently,

it was found that the substitution of Te in CsTe_2O_6 with M (M = various metal cations in +3 and +4 states) in $\text{Cs}(\text{M},\text{Te})_2\text{O}_6$ series gives rise to mixed valence tellurium oxides which leads to *n*-type materials (Siritanon et al., 2009). Investigations of materials in the series have led to an assumption that compounds with smaller unit cells and with appropriate M ion will have higher conductivity. However, there are no direct evidences to support such conclusions. As the only series of semiconducting tellurate oxides where Te plays a role in the electronic conductivity, understanding their electronic structure is crucial in many aspects of solid state chemistry. Therefore, it is the motivation in this work to study electronic properties in defect pyrochlore oxides containing tellurium.

Concerning environmental issues, photocatalysis plays an important role in many aspects because the solar light is a plentiful and green energy source in the reaction. Photocatalysts can degrade hazardous pollutants especially in sewage water and produce H_2 fuel by water splitting. Several Te-containing defect pyrochlore oxides have been studied to show potential as photocatalysts (Jitta et al., 2015). Various strategies have been utilized to achieve better photocatalytic activity and catalyst stability. Because the reaction mechanisms and electronic band structures relating to the photocatalytic performance, in this works, the structure-property relationship especially the electronic conductivity and photocatalytic activity of Te-containing defect pyrochlore oxides ($\text{A}(\text{M},\text{Te})_2\text{O}_6$) are explored.

1.2 Background

This thesis focuses on the investigation of the effects of metal ion substitution on the electronic and photocatalytic properties of tellurium containing defect

pyrochlore oxide. Understanding the relationship between structure, composition and the obtained properties is a key point of the study. The background of crystal and electronic structure are, therefore, crucial to this work. Thus, this part presents basic knowledge of defect pyrochlore structure, classification of mixed valence compounds, band structure, electronic properties, and photocatalysis.

1.2.1 The structure of defect pyrochlore oxides

The general formula of a typical pyrochlore oxide is $A_2B_2O_6O'$ ($A_2B_2O_7$). A wide range of cations can be substituted into A and B sites leading to many different compositions with various properties. The crystallographic structure of pyrochloes is built up from corner sharing BO_6 octahedra and A-O' chains. These oxides crystallize in cubic lattice with $Fd\bar{3}m$ space group and 8 formula per unit cell ($z = 8$). However, the interaction between B_2O_6 network and A_2O' network is weak. In fact, B_2O_6 network acts as the back bone of the structure allowing many possible types of vacancies. Partial vacancies at A position results in $A_{2-x}B_2O_7$. O' site may be entirely vacant to yield $A_2B_2O_6$ while vacancies on both O' and A site give AB_2O_6 (Jitta et al., 2015). Similar to the normal pyrochlore, the AB_2O_6 defect pyrochlore structure is built up of corner sharing BO_6 octahedra, which create networks of hexagonal tunnels. The "A" cation are located in these tunnels (Figure 1.1). In AB_2O_6 , the A cation can be in 8b ($3/8, 3/8, 3/8$), 16d ($1/2, 1/2, 1/2$), or 32e (x, x, x) site, depending on ionic radius. On the other hand, the B cation and O ion are occupied in 16c (0, 0, 0) and 48f ($x, 1/8, 1/8$) site, respectively (Jitta et al., 2015).

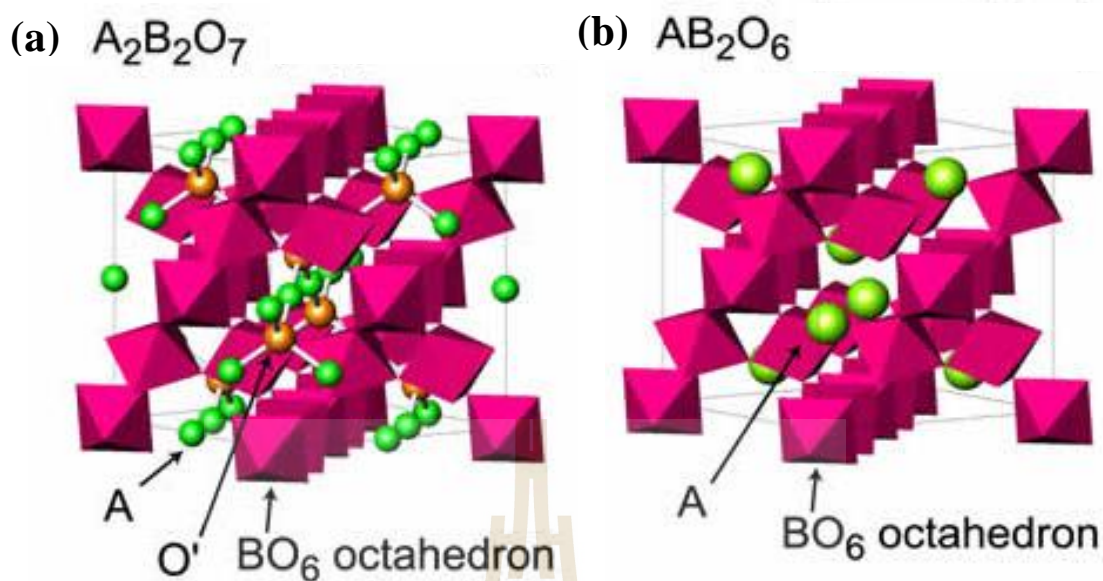


Figure 1.1 The crystal structures of general pyrochlore (a) and defect pyrochlore (b) (Jitta et al., 2015).

1.2.2 Classification of mixed valence compounds

Mixed valence compounds are the compounds that consist of elements with more than one oxidation states. Many elements in the periodic table can possess variable oxidation states. These elements include some of d-block, f-block, lanthanides, actinides, and post-transition elements. Robin and Day (1968) studied and classified mixed valence compounds into three classes based on the difference between the environments surrounding the ions of differing valency (Robin and Day, 1968). Some examples are shown in Table 1.1.

(1) Class I

For class I mixed valence compounds, ions with different oxidation state are in different environments. The compounds in this class are insulators because a high activation energy is required to transfer electrons from site to site. For

examples, in GaCl_2 , Ga(III) and Ga(I) are in tetrahedral and dodecahedral site, respectively (Figure 1.2) (Brown, 1979).

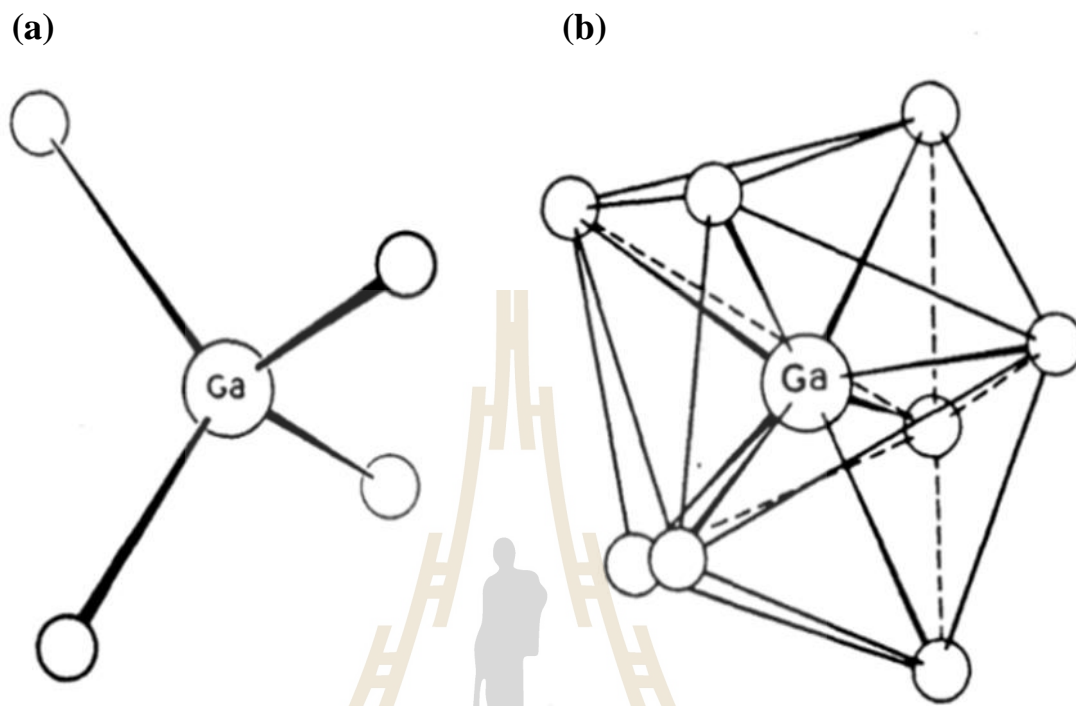


Figure 1.2 The coordination around the Ga(III) (a) and Ga(I) (b) ion in GaCl_2 (Brown, 1979).

(2) Class II

The ions with distinguishable oxidation states in this class are in similar, but not equivalent, environment. The activation energy for electron transfer from site to site is small. Therefore, mixed valence compounds in class II are usually semiconductors. For example, $(\text{C}_3\text{H}_7\text{NH}_3)_4\text{SbCl}_6(\text{Cl})_2$ consists of both Sb(III) and Sb(V) in octahedral site, but the two sites are distinguishable by small differences in bond angles and bond lengths. The crystallographic site of Sb(III) and Sb(V) in $(\text{C}_3\text{H}_7\text{NH}_3)_4\text{SbCl}_6(\text{Cl})_2$ are shown in Figure 1.3 (Brown, 1979).

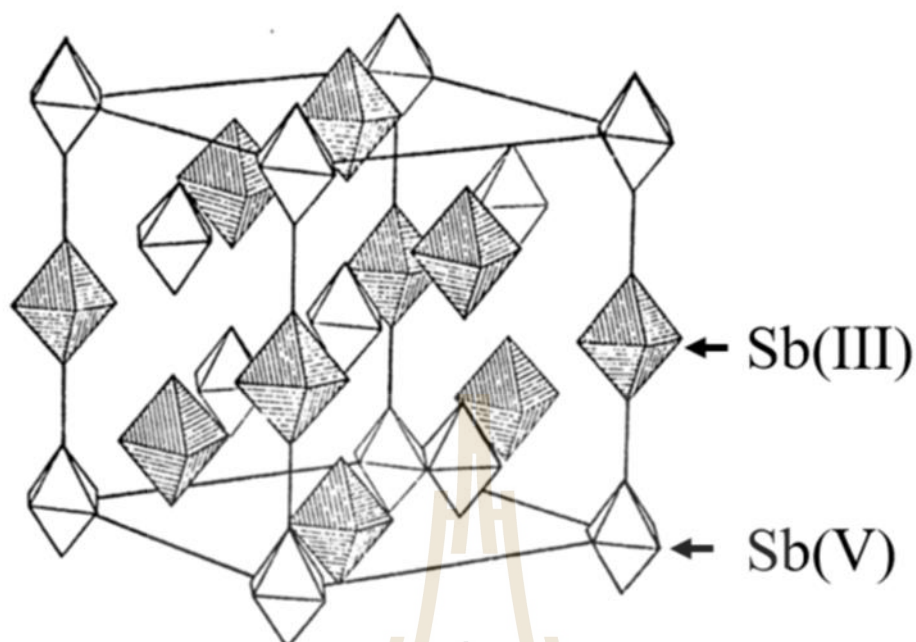


Figure 1.3 Crystal structure of $(C_3H_7NH_3)_4SbCl_6(Cl)_2$ (Brown, 1979).

(3) Class III

For mixed valence compounds in Class III, ions with different oxidation states are in the equivalent site. The mixed valence compounds in class III are often metals or superconductors because electrons do not require activation energy to transfer from site to site. $Ba_{1-x}K_xBiO_3$ is an example in this class and shown in Figure 1. 4. It consists of both Bi(III) and Bi(V) in octahedral site. Electrons can be transferred without activation energy because both ions are in the indistinguishable crystallographic sites. Thus, $Ba_{1-x}K_xBiO_3$ are metallic and, at low enough temperature, superconducting (Kambe et al., 1998).

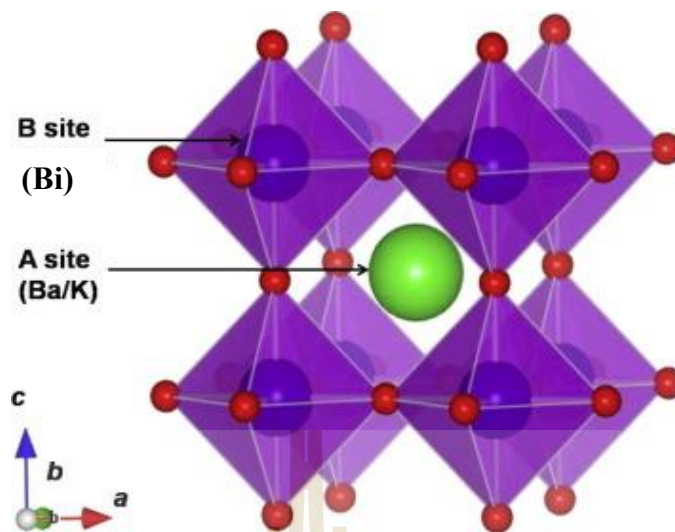


Figure 1.4 Crystal structure of $\text{Ba}_{1-x}\text{K}_x\text{BiO}_3$ (Rubel et al., 2015).

Table 1.1 Classification of mixed valence compounds (Brown, 1979).

Class	Compound	Oxidation states
I	GaCl_2	Ga (I, III)
	Sb_2O_4	Sb (III, VI)
II	$\text{Fe}_4[\text{Fe}(\text{CN})_6]_3 \cdot x\text{H}_2\text{O}$	Fe (II, III)
	$(\text{C}_3\text{H}_7\text{NH}_3)_4\text{SbCl}_6(\text{Cl})_2$ and Cs_2SbCl_6	Sb (III, VI)
	Eu_3S_4	Eu (II, III)
III	(Na_xWO_6) $0.4 < x < 0.9$	W (V, VI)
	LiTi_2O_4	Ti (III, IV)
	$\text{BaBi}_x\text{Pb}_{1-x}\text{O}_3$	Pb (II, IV)

1.2.3 Band structure and electronic properties

The band structures in solid state compounds are built from the overlap of a large number of atomic orbitals. The highest filled band is called the valence

band (VB) and the lowest empty band is called the conduction band (CB) (Atkins et al., 2014; West, 2014). The distance between the top edge of the valence band (E_v), and the bottom edge of the conduction band (E_c) is called the band gap or energy gap (E_g) (Tilley, 2013). Thus, $E_g = E_c - E_v$. E_g determines the electrical properties of solids which can be classified into metals, semiconductors, and insulators (Dann, 2000). The energy of highest filled state in the band structure at a temperature of absolute zero ($T = 0$ K) is known as the Fermi level, which is also another important component in electrical properties of materials (Cox, 1987; West, 2014).

Based on the energy band model, the differences among insulators, semiconductors and metals can be explained. In insulators, the electrons are completely filled in the VB and the band gap is very large. Only a few electrons can accept enough thermal energy to move from the VB into the CB. Therefore, an insulator has very small electronic conductivity (Atkins et al., 2014; West, 2014). The band structure of an insulator is shown in Figure 1.5.

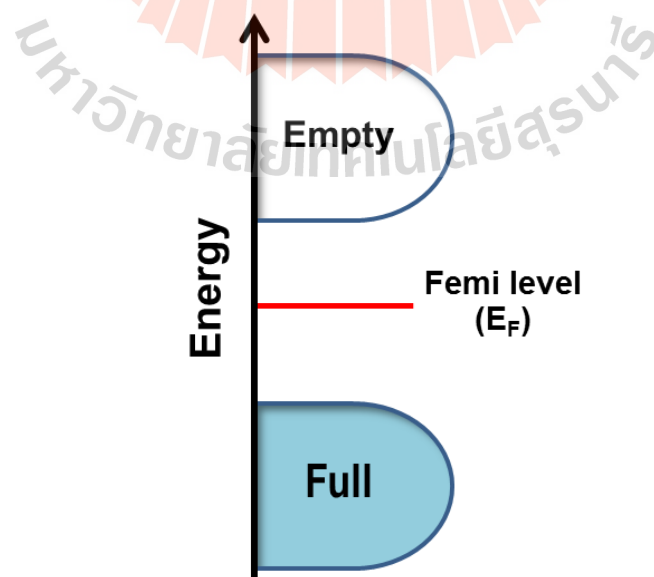


Figure 1.5 The band structure of insulators (Atkins et al., 2014).

Metals are materials with large conductivity. Electrons in highest occupied band is partly filled (Figure 1.6(a)) or the highest filled occupied band and the next lowest unoccupied band overlap in energy (Figure 1.6(b)), therefore the electrons need very small additional energy to move into higher states (Atkins et al., 2014; Dann, 2000). In general, when temperature increases, the conductivity decreases (Figure 1.7). This is due to the drop in electron mobility, which is a result of the electron-phonon collisions obstructing the electrons movement.

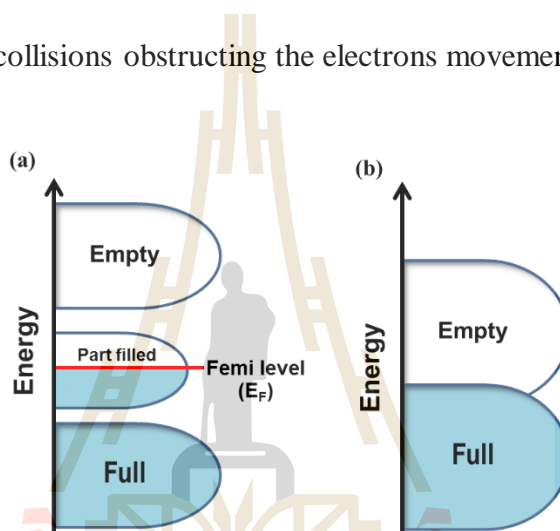


Figure 1.6 The band structure of metals (Atkins et al., 2014; Dann, 2000).

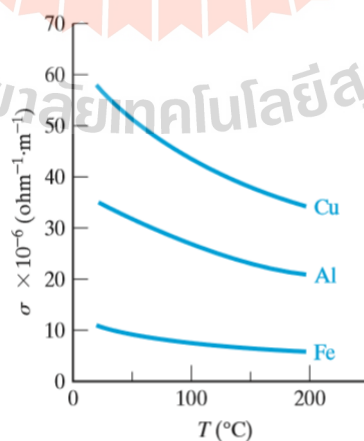


Figure 1.7 Variation in electrical conductivity with temperature for some metals. (West, 2014).

The semiconductors are the border line between insulators and metals. Semiconductors are similar to insulators but with a smaller band gap energy. Semiconductors can be divided into two types: intrinsic and extrinsic. An intrinsic semiconductor has a small band gap and thus small activation energy. Therefore, some electrons can accept enough thermal energy to move into the CB, and leaving holes in the VB as shown in Figure 1.8. The conductivity increases with temperature, as can be explained by Arrhenius equation [1]:

$$\sigma = \sigma_0 e^{-(E_g/2Tk)} \quad [1]$$

where σ , k , and T are electrical conductivity, Boltzmann constant, and temperature (K), respectively. Adding the logarithm to both sides results in Equation [2]:

$$\ln \sigma = \ln \sigma_0 - (E_g/2Tk) \quad [2]$$

which indicates that Arrhenius plot of $\ln \sigma$ versus T^{-1} gives a straight line with a slope of $-E_g/2k$ (Figure 1.9). Therefore, activation energy (E_a) is approximately equal to a half of E_g (Shackelford, 2015; Tilley, 2013).

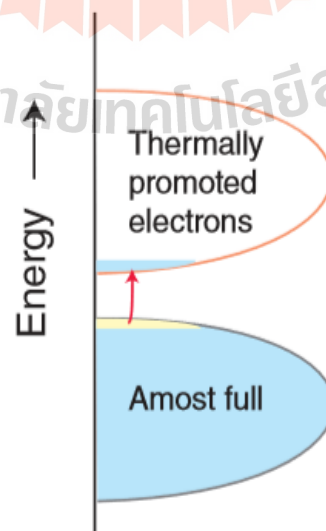


Figure 1.8 The band structure of an intrinsic semiconductor (Atkins et al., 2014).

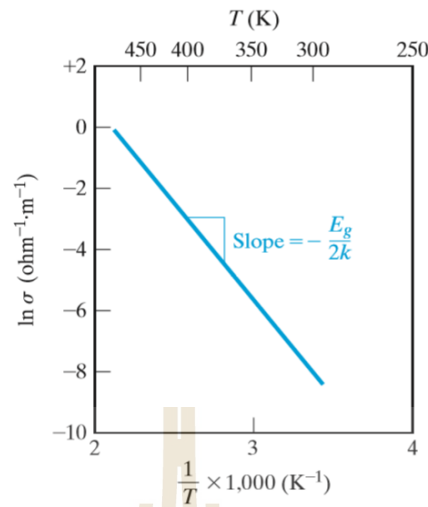


Figure 1.9 The Arrhenius plot of the electrical conductivity for an intrinsic semiconductor (Shackelford, 2015).

The extrinsic semiconductors are created by adding impurity atoms or ions known as dopants. There are two types of extrinsic semiconductors depending on the major charge carriers. Materials are classified as *n*-type and *p*-type semiconductors when the major charge carriers are electrons and hole, respectively (Shackelford, 2015). Band structures of *n*-type and *p*-type semiconductors additionally consist of filled donor level (E_d) below the CB and empty acceptor levels (E_{ac}) over the VB, respectively (Figure 1.10). Similarly, thermal activation involving E_d and E_{ac} in extrinsic semiconductors follows the Arrhenius equation [3]. Adding the logarithm to both sides of Equation [3] give Equation [4].

$$\sigma = \sigma_0 e^{-(E_a/Tk)} \quad [3]$$

$$\ln \sigma = \ln \sigma_0 - (E_a/Tk) \quad [4]$$

E_a is the activation energy, which is a difference between the bottom edge of the CB (E_c) and E_d (*n*-type), or difference between the top edge of the VB (E_v) and E_{ac} (*p*-

type) (Shackelford, 2015; Tilley, 2013). The Arrhenius plot of extrinsic semiconductors are shown in Figure 1.11.

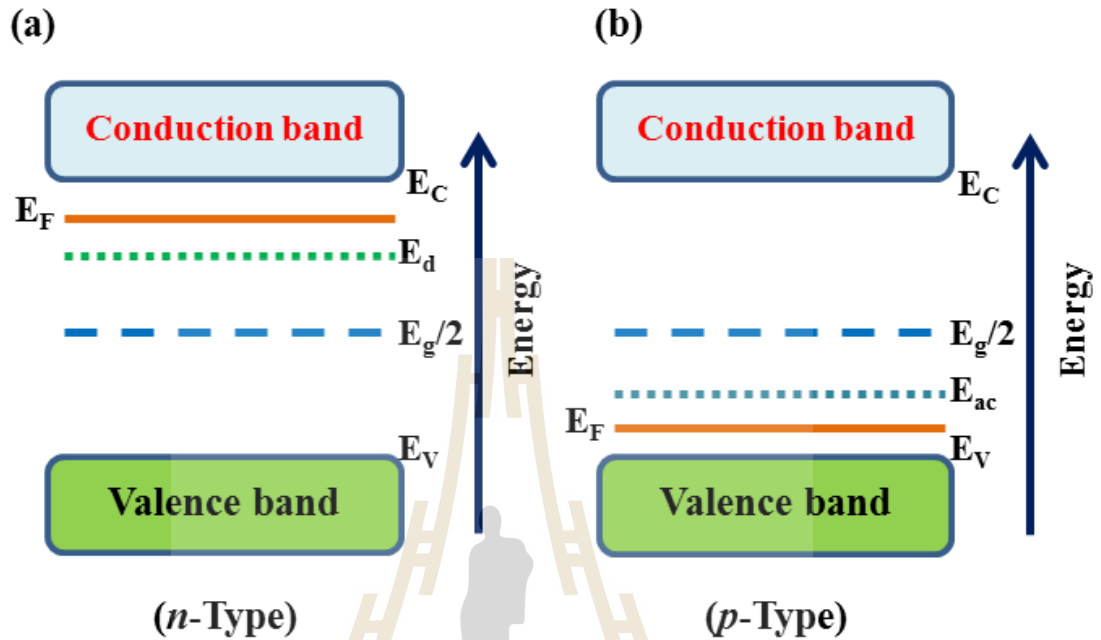


Figure 1.10 Energy band structures of *n*-(a) and *p*-type (b) semiconductor (Tilley, 2013).

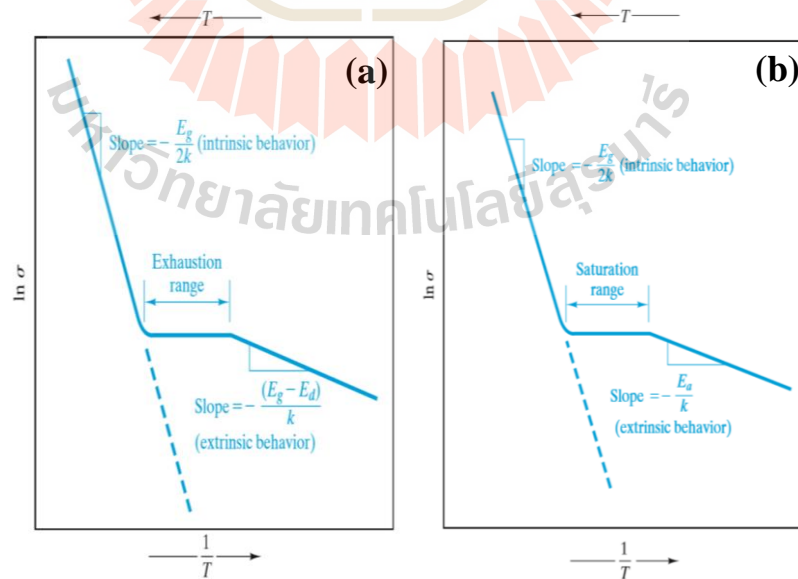


Figure 1.11 Arrhenius plots of electrical conductivity for *n*-(a) and *p*-type (b) semiconductor (Shackelford, 2015).

1.2.4 Interactions between UV-Visible light and solids

The interactions between UV-Visible light and solids can be classified into five processes: absorption, reflection, emission, scattering, and transmission (Figure 1.12). Generally, the absorption and emission are the processes that determine the color in solids (Tilley, 2013). The light that leaves the material is the transmitted light. If the portion of transmitted light is high, the solids are said to be transparent to that wavelength. In addition, some of the incident light may be scattered. The most common scattering process is reflection, which occurs at surfaces. Smooth surfaces reflect light uniformly known as specular reflection. Rough surfaces will reflect incident light in all directions, called diffuse reflection (Tilley, 2013).

The absorption and emission process is useful in investigating the optical properties of solids (Tilley, 2013). The energy in UV-Visible range causes the excitation of electrons, which gives the electronic transition details. If the photon energy is equal to or greater than the E_g , the photon will be absorbed and used to activate electrons in VB to CB. This process is called absorption (Figure 1.13(a)). On the other hand, when electrons are in a high-energy state, they may lose energy by dropping to a lower energy state and simultaneously emit photons. This process is called spontaneous emission (Figure 1.13(b)).

The diffuse reflectance UV-Vis spectra obtained from solids can be used to estimate E_g value using the theory proposed by Kubelka and Munk (Kubelka and Munk, 1931). The Kubelka-Munk equation [5] is applied to an infinite-thick sample at any wavelength.

$$\frac{K}{S} = \frac{(1-R_\infty)^2}{2R_\infty} \equiv F(R_\infty) \quad [5]$$

where R = reflectance, $R_\infty = R_{\text{sample}}/R_{\text{standard}}$, $F(R_\infty)$ is remission or Kubelka-Munk function, S , and K are scattering and absorption coefficients, respectively. In the band structure, bandgap, and absorption coefficient of semiconductors are related through the equation [6]

$$[F(R_\infty)hv]^{1/n} = C(hv - E_g) \quad [6]$$

where C is a proportionality constant and $n = 1/2$ and 2 for direct and indirect allowed transition, respectively. The extrapolation of the highest slope line in the plot of $[F(R_\infty)hv]^{1/n}$ with the corresponding n against hv gives the estimated E_g (Morales et al., 2007).

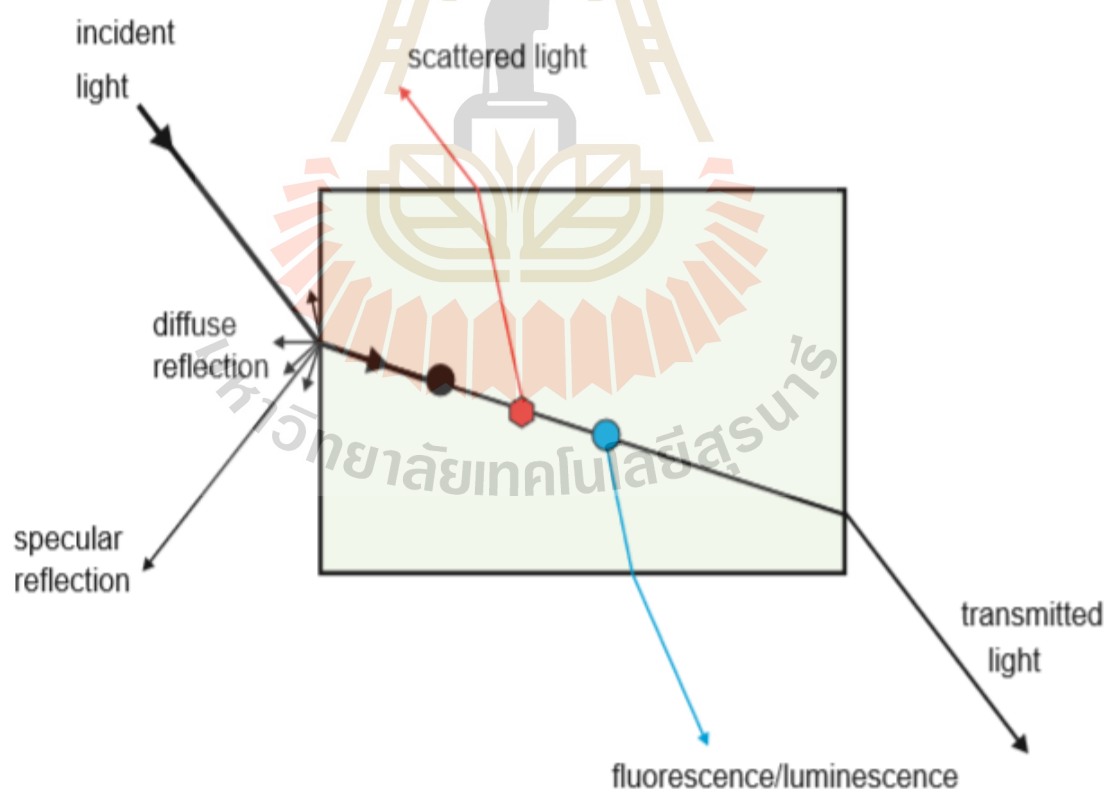


Figure 1.12 The interactions between the incident light and solids (Tilley, 2013).

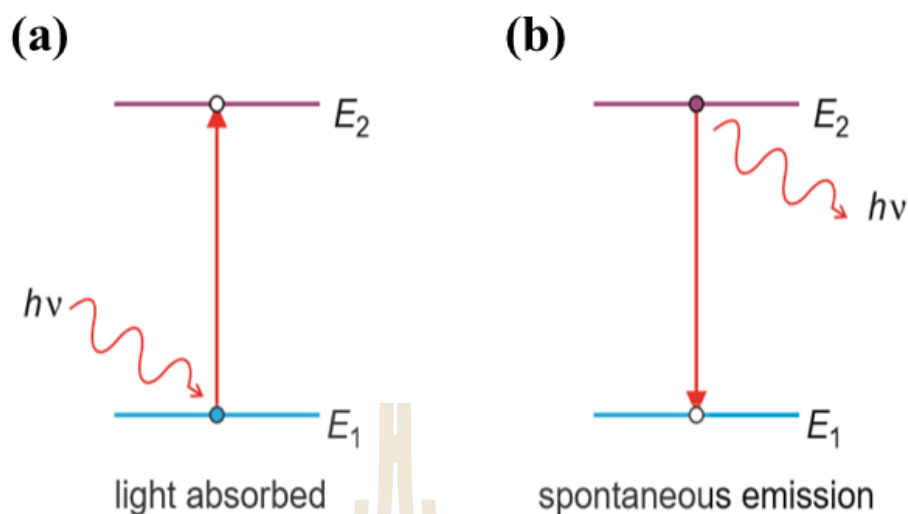


Figure 1.13 Absorption (a) and spontaneous emission (b) of light radiation (Tilley, 2013).

1.2.5 X-Ray absorption spectroscopy of 3d transition metals

X-ray absorption spectroscopy (XAS) has been proven a powerful tool in identifying the oxidation states of ions in the materials. XAS spectra are also capable of giving information about the environment around ions in the structure (Daengsakul et al., 2015; Wongsaprom et al., 2015). XAS spectra of any materials are characteristic of absorbing element with sharp absorption at specific X-ray photon energies. Thus, these sharp absorption are called absorption edges (Schnohr and Ridgway, 2015; Van Bokhoven and Lamberti, 2016).

XAS is based on core-level absorption. When core electrons are ejected to the continuum by required energy (X-ray irradiation) which are dipole allowed transition. The absorption discontinuity is known as the *K*-edge and $L_{3,2}$ -edge when excitations are from 1s and 2p core level, respectively. For 3d transition metals, *L*-

edge spectroscopy is more sensitive to the electronic structure comparing to the K -edge spectroscopy (Haverkort, 2005; Yano and Yachandra, 2009). Figure 1.14 shows typical energy level diagram for K -edge and $L_{3,2}$ -edge transitions of $3d$ transition metals.

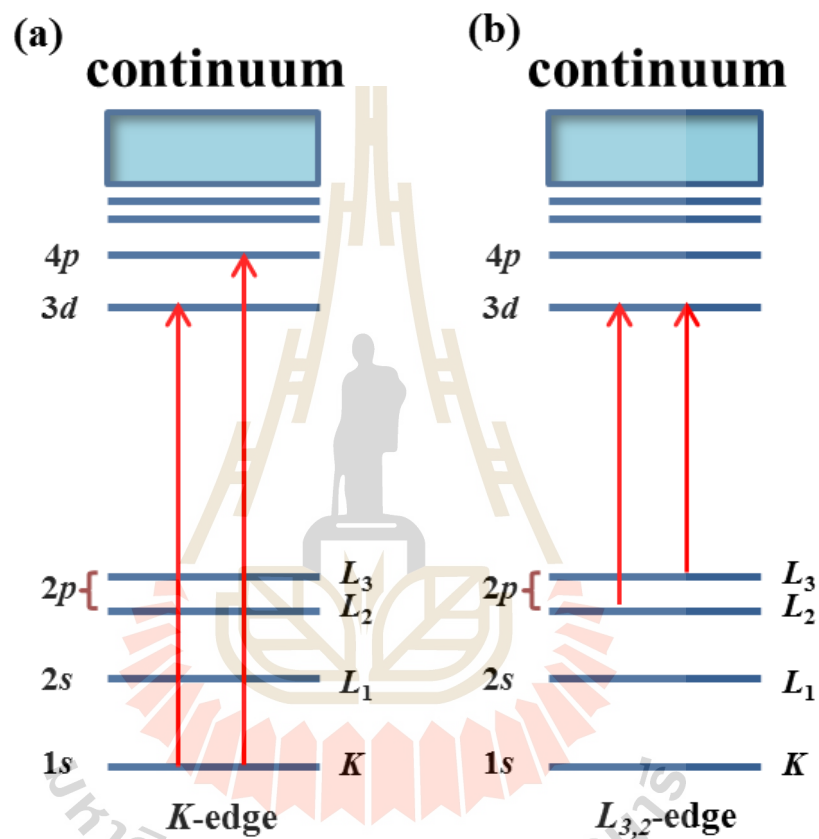


Figure 1.14 The energy level diagram for K -edge and $L_{3,2}$ -edge transitions of $3d$ transition metals (Yano and Yachandra, 2009).

Figure 1.15(a) shows the $2p$ core level XAS spectra for some $3d$ transition metal oxides. The $2p$ to $3d$ excitation of $3d$ transition metals can be found in the 350 to 950 eV energy range (Haverkort, 2005). These spectrum is split into L_3 ($2p_{3/2}$) and L_2 ($2p_{1/2}$) because of the spin-orbit coupling. The distant between the L_3 and

the L_2 edge of late transition metal is larger than early transition metal compounds because the higher charge at nucleus increase the $2p$ spin-orbit coupling constant (Haverkort, 2005). Moreover, each peak is also split into t_{2g} and e_g state due to crystal field effect (Garvie and Craven, 1994). For example, the Ti $L_{3,2}$ -edge XAS spectra of V doped LiTi_2O_4 compare with TiO_2 (anatase) and Ti_2O_3 are shown in Figure 1.15(b) (Chen and Dong, 2015). The L_3 and L_2 edges further split into t_{2g} (A_5 and C_5) and e_g (B_5 and D_5) states because of crystal-field-splitting in $3d$ orbitals. This is octahedral (O_h) crystal-field splitting. The broadening in B_5 peak when increasing V content is due to the Jahn-Teller effect distortion with ΔE_{J-T} energy is split in the e_g band. However, the $L_{3,2}$ -edge XAS spectrum shape and position of $3d$ transition metals can refer to valence state of metal ions (Balasubramanian, 2013; Thakur et al., 2008).

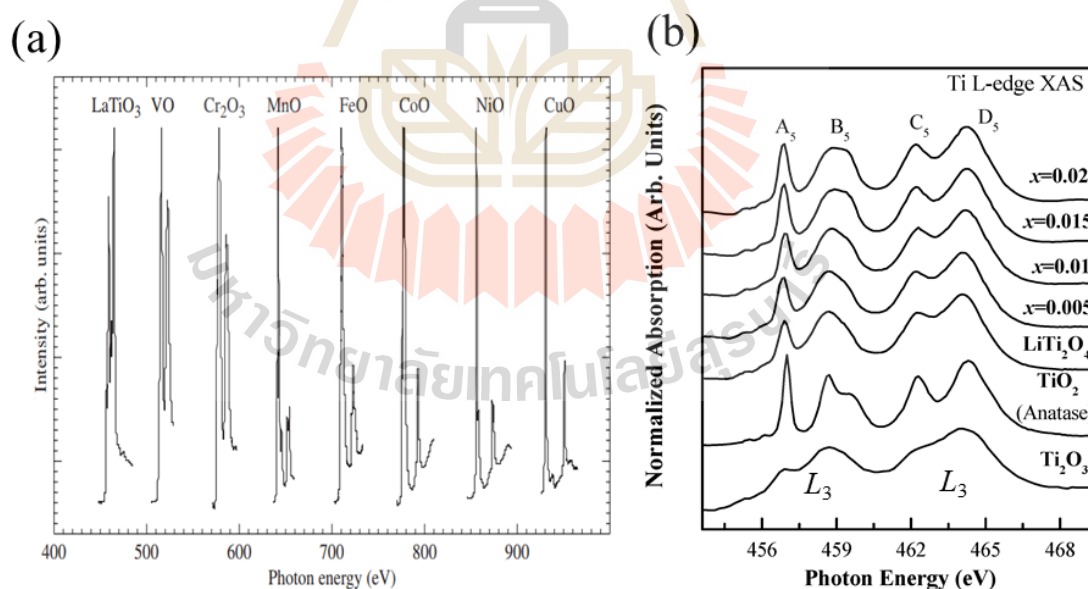


Figure 1.15 The $2p$ core level XAS spectra of some $3d$ transition metal oxides (a). Ti $L_{3,2}$ -edge XAS spectra of V doped LiTi_2O_4 compare with those of TiO_2 (anatase) and Ti_2O_3 (b) (Chen and Dong, 2015; Haverkort, 2005).

1.2.6 Oxygen 1s X-Ray absorption spectroscopy

In oxide materials, O 1s XANES can be used to explain character of electronic band structure (Pellegrin et al., 1997). The O 1s XANES spectra is the absorption edge of 1s to 2p transition in oxygen atom that is directly related to the oxygen *p*-projected states in the conduction band (Balasubramanian et al., 2013). Thus, the oxygen *p* character in unoccupied states of oxides compounds can be explained primarily based on the O 1s XAS spectra. Groot et al. (1989) have studied and reported the O 2p character hybridization of unoccupied state of 3*d*-transition-metal oxides (Figure 1.16). The spectra can be divided into two regions: the first is a double-peaked sharp structure (shade), which is related to the metal 3*d* states; the second is a broader structure at 5 -10 eV above the edge which is related to the metal 4*s* and 4*p* bands (De Groot et al., 1989).

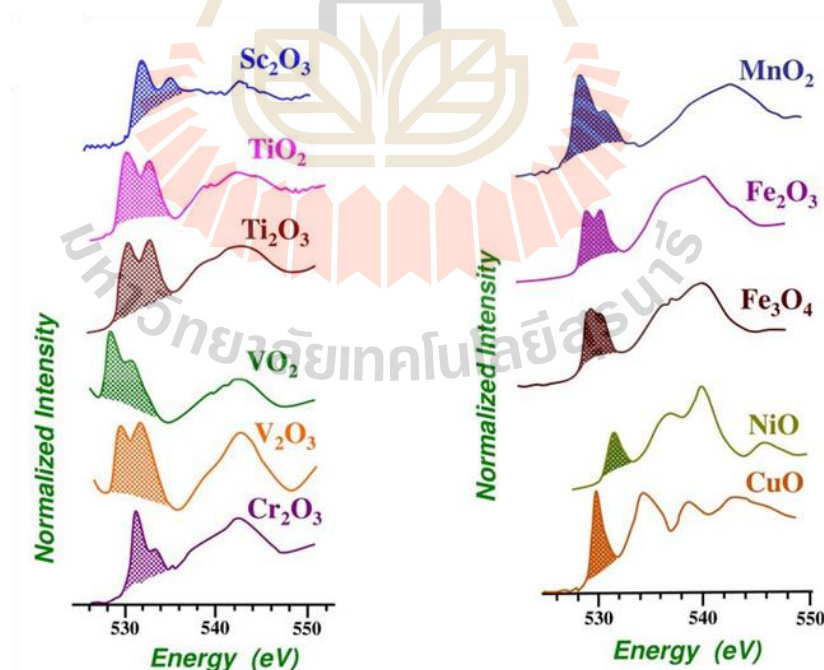


Figure 1.16 Oxygen 1s X-ray absorption edge spectra of 3*d* transition metal oxides (De Groot et al., 1989).

1.2.7 Photoelectron spectra at valence band

Photoelectron spectroscopy makes use of the photoelectric effect with soft X-ray. Al K α (1486.6 eV) X-ray is usually used (Wagner, 2011). When a surface of solid is irradiated with X-ray photons of sufficient energy, $h\nu$, photoelectrons can be ejected from inner shells with a kinetic energy (K.E.) equal to [7]. The schematic of photoelectron process are shown in Figure 1.17.

$$\text{K.E.} = h\nu - \text{B.E.} - \Phi \quad [7]$$

when Φ is the instrument's spectrometer work function and B.E. is the binding energy of the photoelectron (Cox, 1987). The binding energy of electrons in core levels of an atom is unique to each element. The binding energy of core levels depends on formal oxidation states, chemical environments, and lattice sites of atoms. The difference of binding energy is called chemical shift which is the result of exchange potentials exercised on an electron by its environment. The photoelectron spectra in the binding energy range of about 15 eV to 0 eV (Fermi level) is used to probe a valence band (Cox, 1992). In oxides, XPS spectra at valence band can be used to explain the O 2*p* hybridization character in the occupied states near the Fermi level (E_F) (Cox, 1992). Such an application is very useful because the said states significantly influence the materials electronic properties.

XPS valence band has been used to study the electronic structure of materials (Dudric et al., 2014; Falub et al., 2003; Fujimori et al., 1992). Hishida et al. (2013) reported the electronic structure of *p*-type $\text{La}_{1-x}\text{Sr}_x\text{MnO}_3$ using XPS spectra at valence band spectra. They can identify Mn 3*d* and the Mn 3*d*-O 2*p* hybridization character of the occupied states (Hishida et al., 2013). In addition, XPS spectra at valence band can be combined with O *K*-edge XAS to propose electronic band

structure, leading to the deeper understanding of the electronic properties (Zhang et al., 2015).

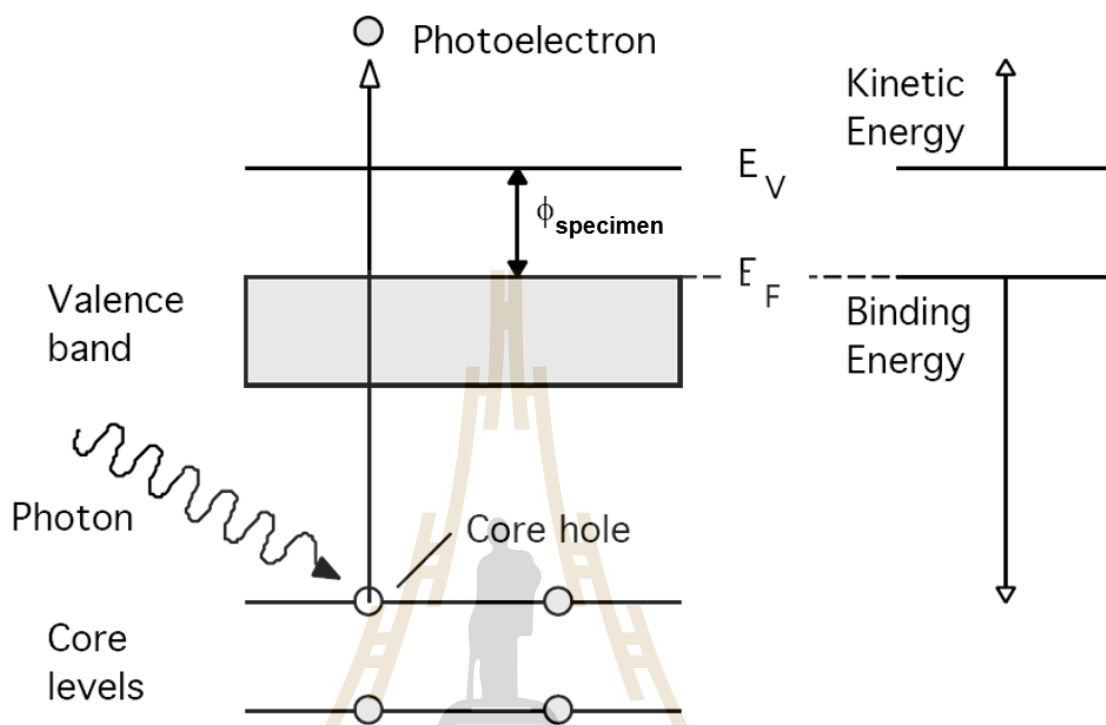


Figure 1.17 Schematic of photoelectron process (Wagner, 2011).

1.2.9 Photocatalysis

Photocatalysis consists of two processes: photoreaction and catalysis.

Photocatalysis is the process in which light is used to activate a substance, called photocatalyst, which modifies the rate of a chemical reaction. The classification of the photocatalysts is the same as that of general catalysts. If the phase of reactants and photocatalysts are the same, the reaction is known as 'homogeneous photocatalysis'. In contrast, heterogeneous photocatalysis is assigned when they have different phases.

The reactions occur on the surface of catalysts as depicted in Figure 1.18 (Aditya et al., 2015). The UV and visible light with the energy equal to or higher

than bandgap ($h\nu \geq E_g$) initiates the excitation of electrons and generates electrons (e^-) and holes (h^+). The electron-hole pairs can combine with surface H_2O and adsorbed O_2 via the redox reaction to form active species. Taking a photodegradation as an example, the active species react with dye molecules and degrade them (Jitta et al., 2015). However, if the recombination of electrons and holes takes place, the redox reaction cannot progress. The competition between separation and recombination of electron-hole pairs determines the photocatalytic efficiency.

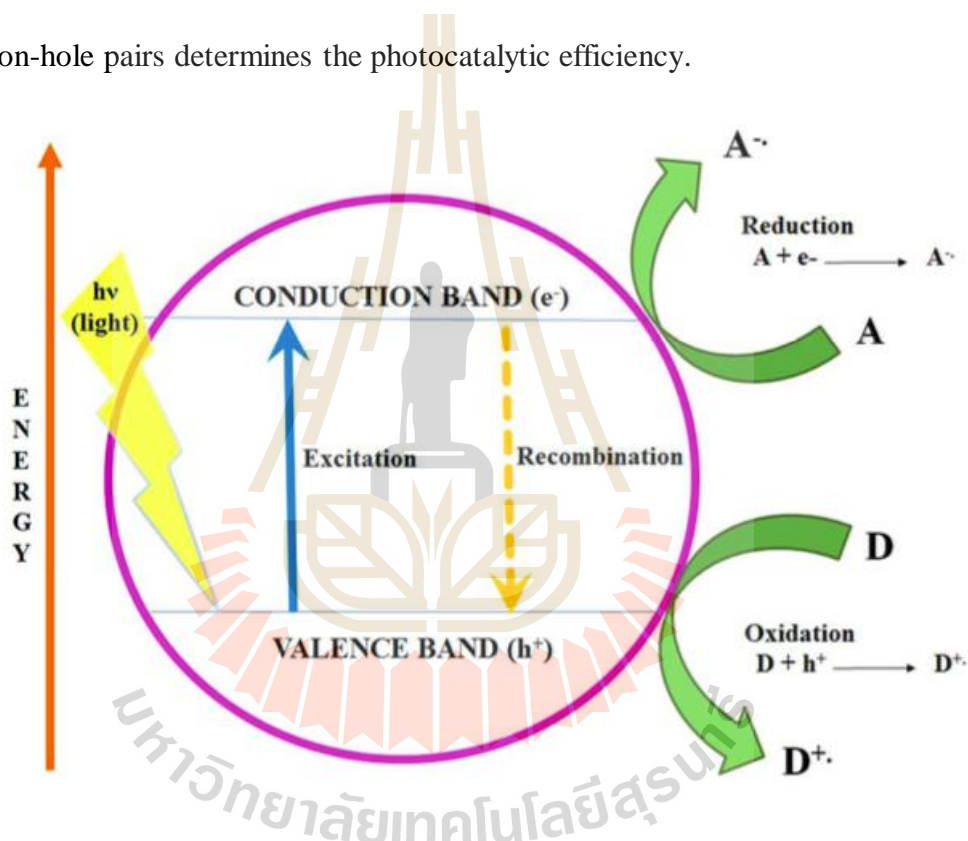


Figure 1.18 A schematic diagram of a photocatalytic process (Aditya et al., 2015).

Semiconducting metal oxides are promising for photocatalytic applications as they have the ability to create charge carriers. Here, we focus on the application in pollutant degradation and water splitting (Jitta et al., 2015).

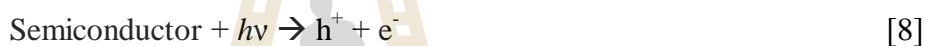
The primary photocatalytic oxidation mechanism includes the following five steps. The details of the mechanism are as follows (Tayade, 2013)

(1) Irradiation

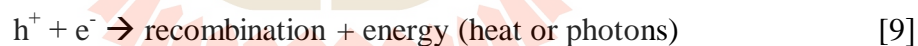
The first step is the light irradiation process for activation and conversion of light energy to chemical energy, thus leading to the generation of e^-/h^+ pairs. The requirement of this step is that the incoming photon have an energy, $h\nu$, of equal to or higher than the semiconductor band gap energy.

(2) Separation and recombination of e^-/h^+ pairs

The photoexcited e^- is transferred into the conduction band, leading to the separation of e^-/h^+ pairs.

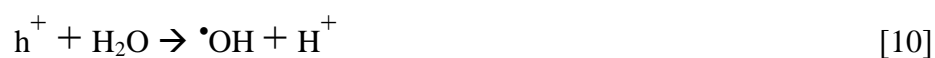


However, the photogenerated e^- and h^+ can recombine in bulk or on the surface of the semiconductor within the short time, by losing energy in the form of heat or photons.



(3) h^+ trapping reactions

In the valence band, the separated h^+ migrates to the surface and is trapped by surface-adsorbed hydroxyl groups or water to produce trapped holes, which is usually explained as a surface-adsorbed hydroxyl radical ($\bullet\text{OH}$). On the other hand, h^+ can also be directly involved in oxidation of pollutant.



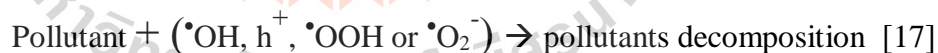
(4) e⁻ trapping reactions

In the conduction band, O₂ often acts as the electron acceptor to trap the photoexcited e⁻, thus protecting the e⁻/h⁺ recombination. In this process, [•]O₂⁻ is formed which can have a variety of reactions to produce active species. H₂O₂ can also produce the highly reactive [•]OH by reduction or cleaving.



(5) The pollutants decomposition

During the overall photochemical process, the photo-generated e⁻/h⁺ and the produced active species such as [•]OH, [•]O₂⁻, [•]OOH and H₂O₂ react with pollutants to decompose them



The essential property for semiconducting metal oxides with high photodegradation efficiency is the appropriate level of VB and CB. This means that the oxidation potential value of the photogenerated h⁺ must be more positive than oxidation potentials of H₂O to generate [•]OH radicals. The reduction potential value of the photogenerated electrons needs to be more negative than reduction potentials of O₂ to reduce absorbed O₂ to [•]O₂⁻. The [•]O₂⁻ and H₂O₂ are, thus, formed. H₂O₂ can transform into [•]OH (Chiu et al., 2019). The CB and VB positions of some

semiconductors and the chemical potential of some chemical reactions are displayed in Figure 1.18. However, pollutant species is also an important factor in choosing the catalysts. The cationic species such as methylene blue (MB) (Houas et al., 2001; Xiang et al., 2013), Malachite green oxalate (MG) (Laid et al., 2015), and RhodamineB (RhB) (Xing et al., 2013) are degraded by reduction process, while the anionic species such as methyl orange (MO) (Wang et al., 2007), Eosin yellow (EY) (Laid et al., 2015), and nitrophenol (Aditya et al., 2015) are degraded by the oxidation process.

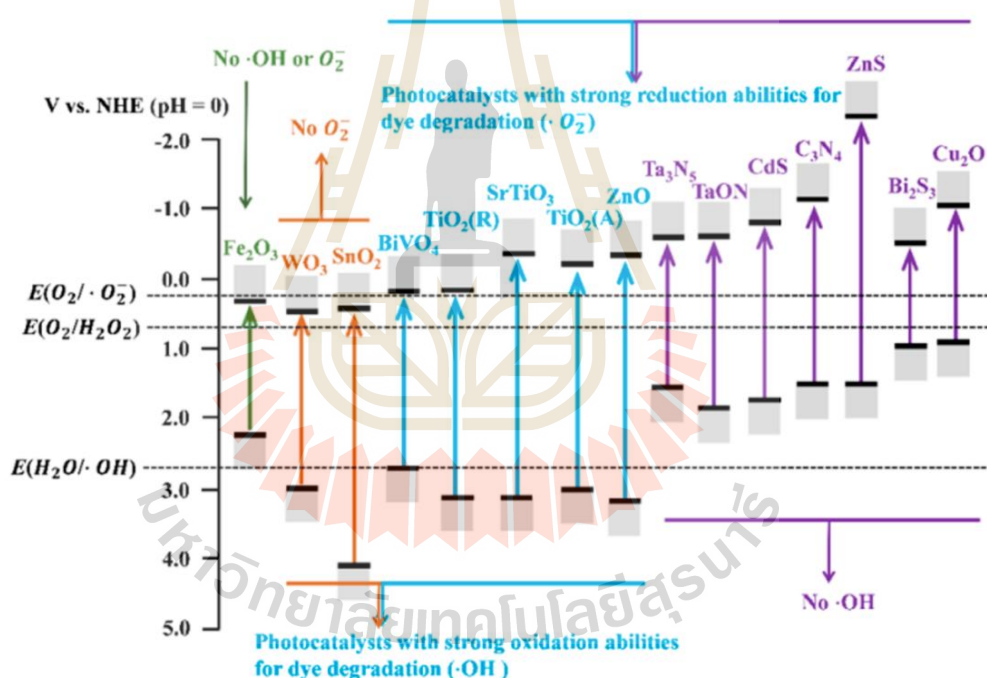


Figure 1.19 Scheme for the band structures of common photocatalysts, and potentials of the radical generation (Chiu et al., 2019).

1.3 References

Aditya, T., Pal, A., and Pal, T. (2015) Nitroarene reduction: A trusted model reaction to test nanoparticle catalyst. **Chemical Communications**. 51: 9410-9431.

- Atkins, P. W., Overton, T. L., Rourke, J. P., Weller, M. T., and Armstrong, F. A. (2014). **Inorganic Chemistry**, 6th eds. Oxford University Press.
- Balasubramanian, P., Nair, H. S., Tsai, H., Bhattacharjee, S., Liu, M., Yadav, R., and Tsai, M. (2013). Valence band electronic structure of $\text{Nd}_{1-x}\text{Y}_x\text{MnO}_3$ using X-ray absorption, photoemission and GGA+U calculations. **Journal of Electron Spectroscopy and Related Phenomena**. 189: 51-55.
- Brown, D. B. (1979). **Mixed-Valence Compounds: Theory and Applications in Chemistry, Physics, Geology, and Biology**. Springer Science & Business Media.
- Chen, C.-L., and Dong, C.-L. (2015). Characterization of the Electronic Structure of Spinel Superconductor LiTi_2O_4 using Synchrotron X-ray Spectroscopy. **In Superconductors-New Developments**. IntechOpen.
- Chiu, Y.-H., Chang, T.-F. M., Chen, C.-Y., Sone, M., and Hsu, Y.-J. (2019). Mechanistic Insights into Photodegradation of Organic Dyes Using Heterostructure Photocatalysts. **Catalysts**. 9(5): 430.
- Cox, P. A. (1987). **The Electronic Structure and Chemistry of Solids**. Oxford Science Publications.
- Cox, P. A. (1992). **Transition Metal Oxides: An Introduction to their Electronic Structure and Properties**, Republished. Oxford University Press.
- Daengsakul, S., Kidkhunthod, P., Soisang, O., Kuenoon, T., Bootchanont, A., and Maensiri, S. (2015). The effect of Gd doping in $\text{La}_{1-x-y}\text{Gd}_x\text{Sr}_y\text{MnO}_3$ compound on nanocrystalline structure by X-ray Absorption Spectroscopy (XAS) technique. **Microelectronic Engineering**. 146: 38-42.
- Dann, S. E. (2000). **Reactions and Characterization of Solids**. Royal Society of

Chemistry.

- De Groot, F., Grioni, M., Fuggle, J., Ghijsen, J., Sawatzky, G., and Petersen, H. (1989). Oxygen 1s x-ray-absorption edges of transition-metal oxides. **Physical Review B**. 40(8): 5715.
- Dudric, R., Vladescu, A., Rednic, V., Neumann, M., Deac, I., and Tetean, R. (2014). XPS study on $\text{La}_{0.67}\text{Ca}_{0.33}\text{Mn}_{1-x}\text{Co}_x\text{O}_3$ compounds. **Journal of Molecular Structure**. 1073: 66-70.
- Falub, M., Tsurkan, V., Neumann, M., Troyanchuk, I., Galakhov, V., Kurmaev, E., and Weitering, H. (2003). Electronic structure of cobalt-doped manganites. **Surface Science**. 532: 488-492.
- Fujimori, A., Hase, I., Nakamura, M., Namatame, H., Fujishima, Y., Tokura, Y., and Fuggle, J. (1992). Doping-induced changes in the electronic structure of $\text{La}_x\text{Sr}_{1-x}\text{TiO}_3$: Limitation of the one-electron rigid-band model and the Hubbard model. **Physical Review B**. 46(15): 9841.
- Garvie, L., and Craven, A. (1994). High-resolution parallel electron energy-loss spectroscopy of Mn $L_{2,3}$ -edges in inorganic manganese compounds. **Physics and Chemistry of Minerals**. 21: 191-206.
- Haverkort, M. W. (2018). **Spin and Orbital Degrees of Freedom in Transition Metal Oxides and Oxide Thin Films Studied by Soft X-ray Absorption Spectroscopy**. arXiv preprint cond-mat/0505214.
- Hishida, T., Ohbayashi, K., Kobata, M., Ikenaga, E., Sugiyama, T., Kobayashi, K., and Saitoh, T. (2013). Empirical relationship between x-ray photoemission spectra and electrical conductivity in a colossal magnetoresistive manganite $\text{La}_{1-x}\text{Sr}_x\text{MnO}_3$. **Journal of Applied Physics**. 113(23): 233702.

- Houas, A., Lachheb, H., Ksibi, M., Elaloui, E., Guillard, C., and Herrmann, J.-M. (2001) Photocatalytic degradation pathway of methylene blue in water. **Applied Catalysis B: Environmental**. 31: 145-157.
- Jitta, R. R., Gundeboina, R., Veldurthi, N. K., Guje, R., and Muga, V. (2015). Defect pyrochlore oxides: as photocatalyst materials for environmental and energy applications a review. **Journal of Chemical Technology & Biotechnology**. 90(11): 1937-1948.
- Kambe, S., Shime, I., Ohshima, S., Okuyama, K., and Sakamoto, K. (1998). Crystal structure and electronic properties of BaBiO_y ($2.5 \leq y \leq 2.9$) and $\text{Ba}_{1-x}\text{La}_x\text{BiO}_3$ ($0 \leq x \leq 0.5$). **Solid State Ionics**. 108(1-4): 307-313.
- Kubelka, P. and Munk, F. (1931). Ein Beitrag zur Optik der Farbanstriche. **Zeitschrift für Technische Physik**. 12: 593-601.
- Laid, N., Bouanimba, N., Zouaghi, R., and Sehili, T. (2015) Comparative study on photocatalytic decolorization of an anionic and a cationic dye using different TiO_2 photocatalysts. **Desalination and Water Treatment**. 57: 19357-19373.
- Morales, A. E., Mora, E. S., and Pal, U. (2007). Use of diffuse reflectance spectroscopy for optical characterization of un-supported nanostructures. **Revista Mexicana de Física**. 53(5): 18-22.
- Pellegrin, E., Tjeng, L., De Groot, F., Hesper, R., Sawatzky, G., Moritomo, Y., and Tokura, Y. (1997). Soft X-ray magnetic circular dichroism study of the colossal magnetoresistance compound $\text{La}_{1-x}\text{Sr}_x\text{MnO}_3$. **Le Journal de Physique IV**. 7(C2): C2-405-C402-408.
- Robin, M. B., and Day, P. (1968). Mixed valence chemistry—a survey and classification. **Advances in Inorganic Chemistry and Radiochemistry**. 10:

247-422.

- Rubel, M. H., Takei, T., Kumada, N., Ali, M., Miura, A., Tadanaga, K., and Moriyoshi, C. (2015). Hydrothermal synthesis of a new Bi-based $(\text{Ba}_{0.82}\text{K}_{0.18})(\text{Bi}_{0.53}\text{Pb}_{0.47})\text{O}_3$ superconductor. **Journal of Alloys and Compounds**. 634: 208-214.
- Schnohr, C. S., and Ridgway, M. C. (2015). **X-ray Absorption Spectroscopy of Semiconductors**. Springer.
- Shackelford, J. F. (2014). **Introduction to Materials Science for Engineers**, 8th Edition. Pearson Upper Saddle River, NJ.
- Siritanon, T., Laurita, G., Macaluso, R. T., Millican, J. N., Sleight, A. W., and Subramanian, M. (2009). First observation of electronic conductivity in mixed-valence tellurium oxides. **Chemistry of Materials**. 21(23): 5572-5574.
- Tayade, R. J. (2013). **Photocatalytic Materials & Surfaces for Environmental Cleanup III: special topic volume with invited peer reviewed papers only**: Trans Tech Publications.
- Thakur, P., Chae, K., Whang, C., Chang, G., Shukla, D., Mollah, S., and Kumar, R. (2008). X-ray Absorption and Emission Spectroscopic Studies of $\text{BiMn}_{2-x}\text{Ti}_x\text{O}_5$ ($0 \leq x \leq 0.5$). **Journal of Korean Physical Society**. 53: 1449.
- Tilley, R. J. D. (2013). **Understanding Solids: The Science of Materials**, 2nd eds. John Wiley & Sons, Ltd.
- Van Bokhoven, J. A., and Lamberti, C. (2016). **X-ray Absorption and X-ray Emission Spectroscopy: Theory and Applications**, Vol. 1. John Wiley & Sons.
- Wagner, J. M.. (2011). **X-ray Photoelectron Spectroscopy: Chemical Engineering Methods and Technology**. Nova Science Publishers Incorporated.

- Wang, W.-D., Huang F.-Q., Liu, C.-M., Lin, X.-P., and Shi, J.-L. (2007). Preparation, electronic structure and photocatalytic activity of the In_2TiO_5 photocatalyst. **Materials Science and Engineering B**. 139:74-80.
- West, A. R. (2014). **Solid State Chemistry and its Applications**, 2nd eds (Student Edition). John Wiley & Sons, Ltd.
- Wongsaprom, K., Sonsupap, S., Maensiri, S., and Kidkhunthod, P. (2015). Room-temperature ferromagnetism in Fe-doped In_2O_3 nanoparticles. **Applied Physics A**. 121(1): 239-244.
- Xiang, X., Xie, L., Li, Z., and Li, F. (2013) Ternary $\text{MgO}/\text{ZnO}/\text{In}_2\text{O}_3$ heterostructured photocatalysts derived from a layered precursor and visible-light-induced photocatalytic activity. **Chemical Engineering Journal**. 221: 222-229.
- Yano, J., and Yachandra, V. K. (2009). X-ray absorption spectroscopy. **Photosynthesis Research**. 102: 241.
- Zhang, K. H., Du, Y., Papadogianni, A., Bierwagen, O., Sallis, S., Piper, L. F., and Chambers, S. A. (2015). Perovskite Sr-Doped LaCrO_3 as a New *p*-Type Transparent Conducting Oxide. **Advanced Materials**. 27(35): 5191-5195.

CHAPTER II

LITERATURE REVIEW

2.1 CsTe₂O₆ and Cs(M,Te)₂O₆-based oxides

CsTe₂O₆ crystallizes in rhombohedral structure (Hamani et al., 2011; Loopstra and Goubitz, 1986). The structure consists of (Te⁴⁺)O₆ octahedra layers located between corner sharing network of (Te⁶⁺)O₆ octahedra layers (Figure 2.1(a)). It is well known that CsTe₂O₆ structure is related to the defect cubic pyrochlore. The major difference between rhombohedral CsTe₂O₆ structure and the Cs(M,Te)₂O₆ cubic pyrochlore is the order-disorder arrangement of the corner sharing (M,Te)O₆ octahedra network (Figure 2.1). The crystallographic site of Te and M in CsTe₂O₆ and Cs(M,Te)₂O₆ are shown in Table 2.1.

Table 2.1 The crystallographic site of Te and M in CsTe₂O₆ and Cs(M,Te)₂O₆ (Siritanon et al., 2011).

Ion	site	Crystallographic site		
		x	y	z
CsTe ₂ O ₆				
Te ⁶⁺	9e	0	0	0.5
Te ⁴⁺	3b	0.5	0	0
Cs(M,Te) ₂ O ₆				
Te	16c	0	0	0
M	16c	0	0	0

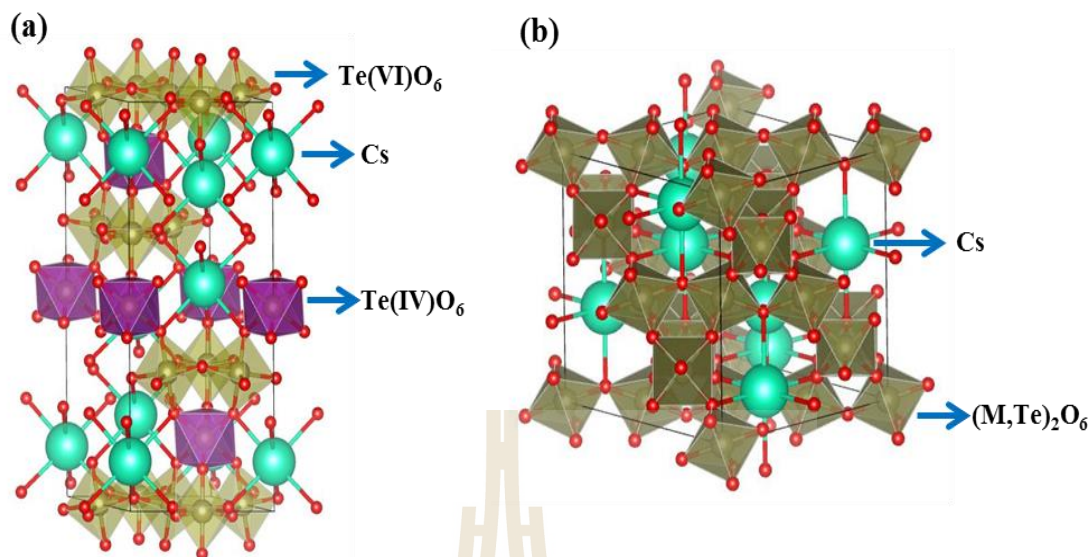


Figure 2.1 Structure of CsTe_2O_6 (a) and $\text{Cs(M,Te)}_2\text{O}_6$ (b) (Siritanon et al., 2009 Siritanon et al., 2011).

CsTe_2O_6 was first prepared from Cs_2CO_3 and TeO_2 by solid state reaction method (Loopstra and Goubitz, 1986). The compound $\text{Cs}(\text{Te}^{4+})_{0.5}(\text{Te}^{6+})_{1.5}\text{O}_6$ can be viewed as a class II mixed valence compound because both Te^{4+} and Te^{6+} are in octahedral sites. However, the difference octahedral size, suitable with ionic radii of both Te^{4+} and Te^{6+} , leads to a splitting of Te 5s band between filled 5s states from Te^{4+} and empty 5s states from Te^{6+} (Figure 2.2(a)). The distance between filled and empty 5s bands is large and consequently low conductivity (Siritanon et al., 2009).

Siritanon et al. (2009) have prepared $\text{Cs(M,Te)}_2\text{O}_6$ ($\text{M} = \text{Al, Cr, Mn, Fe, Co, Ga, Sc, In, Tl, Lu, Tb, Tm, Er, Ho, Ge, Ti, Rh, Ru, Mg, Zn, and Ni}$) by solid state reaction method. These compounds are black in color and show semiconducting behavior. They have concluded that the compounds contain $\text{Te}^{6+}/\text{Te}^{4+}$ mixed valency which leads to an *n*-type materials. Based on the electronic conductivity, the electronic band structure of these materials was proposed as shown in Figure 2.2(b)

(Siritanon et al., 2009). The conduction and valence bands are predominantly Te 5s and O 2p in character, respectively. The conductivity of materials is due to a small amount of Te⁴⁺ defect donor state in this system whose energy is close to the conduction band. However, other factors that affect conductivity of materials in the series are unit cell size and type of M metal as compounds with smaller unit cell and with appropriate M ion have higher conductivity. Li et al. (2011) have studied structure and electrical conductivity of CsAl_xTe_{2-x}O₆. Based on the results, there are two different scenarios of substitution depending on Al content. When Al is lower than 1/3, Al³⁺ replaces Te⁴⁺ resulting in Cs¹⁺(Al³⁺)_x(Te⁴⁺)_{0.5-(3x/2)}(Te⁶⁺)_{1.5+(x/2)}O₆. On the other hand, when x is higher than 1/3, the compounds can be described by (Cs¹⁺)_{1-z}Te⁴⁺_z(Al³⁺)_{1/3+z}(Te⁶⁺)_{5/3-z}O₆. They concluded that the highest electrical conductivity is found in the middle of the range close to CsAl_{0.33}Te_{1.67}O₆ composition, which is a switching point between the two schemes. It was also evidenced that conductivity of the materials in the series is strongly related to cell parameters. Compounds with smaller unit cells tend to have higher electronic conductivity because Te⁴⁺ in the lattice is compressed which raises the energy of the defect states. When the defect states are close to conduction band, activation energy of conduction is decreased and the compounds have higher conductivity.

However, there are no direct evidences on the Te⁴⁺/Te⁶⁺ mixed valency and the proposed band diagrams are not confirmed experimentally. In addition, the role of Cs in the conductivity has never been discussed. To understand electronic behavior on Te-containing defect pyrochlore oxides, this research aims to study effects of K, Rb and Mn substitutions on electronic band structure and related electrical properties of Te-containing defect pyrochlore oxides.

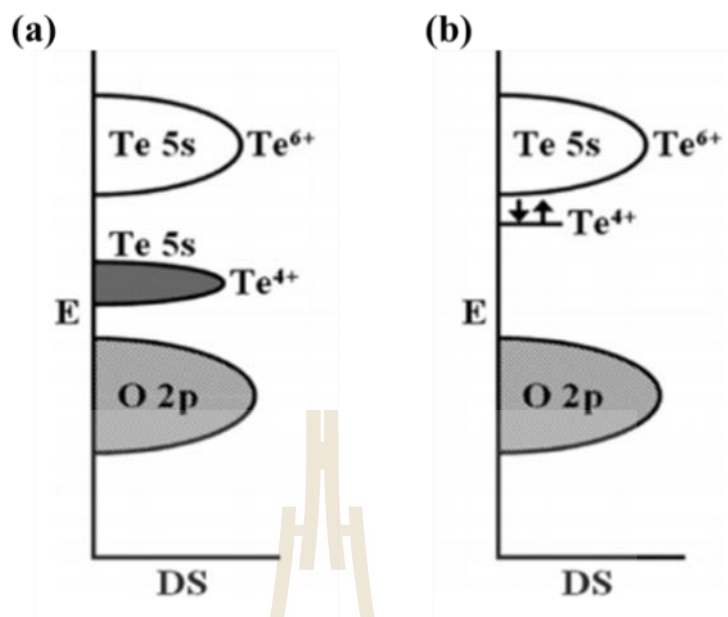


Figure 2.2 Band structure of CsTe_2O_6 (a) and cubic $\text{Cs}(\text{M},\text{Te})_2\text{O}_6$ pyrochlores (b) (Siritanon et al., 2009).

2.2 $\text{ABB}'\text{O}_6$ cubic defect pyrochlores as photocatalysts

The significant characteristics of good photocatalyst oxides are the desired band gap, suitable band potential, high surface area, stability and reusability etc. Many metal oxides have been investigated to have these characteristics. In addition, valence band of metal oxides consisting d^0 and d^{10} metal ions such as NaTaO_3 , Li_2TiO_3 , $\text{La}_2\text{Sn}_2\text{O}_7$ and some of $\text{ABB}'\text{O}_6$ cubic defect pyrochlores, valence bands are usually formed with O 2p orbitals, which lies approximately +3.0 V vs normal hydrogen electrode (NHE). Thus, the valence band potential is more positive than the redox potentials of $\bullet\text{OH}$ radical generation. It is well known that $\bullet\text{OH}$ radical is a very powerful chemical oxidant in the photocatalytic oxidation of organic pollutants.

Several W-containing cubic defect pyrochlores have been investigated as candidates for photocatalytic application such as AMWO_6 (A= Rb and Cs; M= Nb

and Ta), KSbWO_6 , KNbWO_6 , $\text{KFe}_{0.33}\text{W}_{1.67}\text{O}_6$, and $\text{KTi}_{0.5}\text{W}_{1.5}\text{O}_6$ (Ikeda et al., 2004; Jitta et al., 2015; Ravi et al., 2014; Zeng et al. 2018). Substitution of K^+ by other cations such as Ag^+ , Sn^{2+} , Cu^{2+} , Bi^{3+} , Sm^{3+} , Eu^{3+} , and Gd^{3+} on KMWO_6 cubic defect pyrochlores results in the decrease of the bandgap energy (Guje et al., 2016; Ravi et al., 2013; Ravi et al., 2013). The bandgap energy reduction is one strategy to improve photocatalytic efficiency of catalysts. In addition, substitutions of oxygen by nitrogen and sulfur similarly lead to a decrease in the bandgap energy (Marschall et al., 2011; Reddy et al., 2013). Ravi et al (Ravi et al., 2014) reported N, Sn-doped $\text{KTi}_{0.5}\text{W}_{1.5}\text{O}_6$ and their uses in the photodegradation of methylene blue and Rhodamine B. The $\text{KTi}_{0.5}\text{W}_{1.5}\text{O}_6$ parent compound (KTW) was prepared by a sol-gel method. The N-doped $\text{KTi}_{0.5}\text{W}_{1.5}\text{O}_6$ (NKTW) was prepared by heating the mixture of a parent compound and urea ($\text{CO}(\text{NH}_2)_2$). On the other hand, ion exchange method was used to prepare Sn-doped $\text{KTi}_{0.5}\text{W}_{1.5}\text{O}_6$ (SnKTW). The overlapping of N $2p$ and Sn $5s$ states with O $2p$ states lifts the band edge of the valence band and reduce E_g value. The results show that the photocatalytic activity of SnKTW is higher than NKTW and KTW respectively. It is due to a change in its valence band position. The bandgap energy (E_g) decrease from 3.03 eV (KTW) to 2.83 and 2.28 eV for NKTW and SnKTW respectively.

In addition, Te-containing pyrochlore oxides are also reported for photocatalytic dye degradation (Guje et al., 2016; Guje et al., 2015; Venkataswamy et al., 2018). Ravi et al. (Guje et al., 2015) reported Ag and Sn-doped KSbTeO_6 . The KSbTeO_6 parent compound was prepared by a solid state method. On the other hand, Ag and Sn-doped KSbTeO_6 were prepared by ion exchange method with AgNO_3 and SnCl_2 solution respectively. They are used in the methylene blue photodegradation.

The mixing of Ag 4d and Sn 5s states with O 2p states lifts the band edge of the valence band leading to a reduction in E_g value as shown in Figure 2.3. As a consequence, the photocatalytic activity of AgSTO is higher than SnSTO and KSTO respectively. Thus, the photodegradation performance of cubic defect pyrochlore shows clear correlation with the band gap energy. Catalysts with lower band gap energies show higher efficiency.

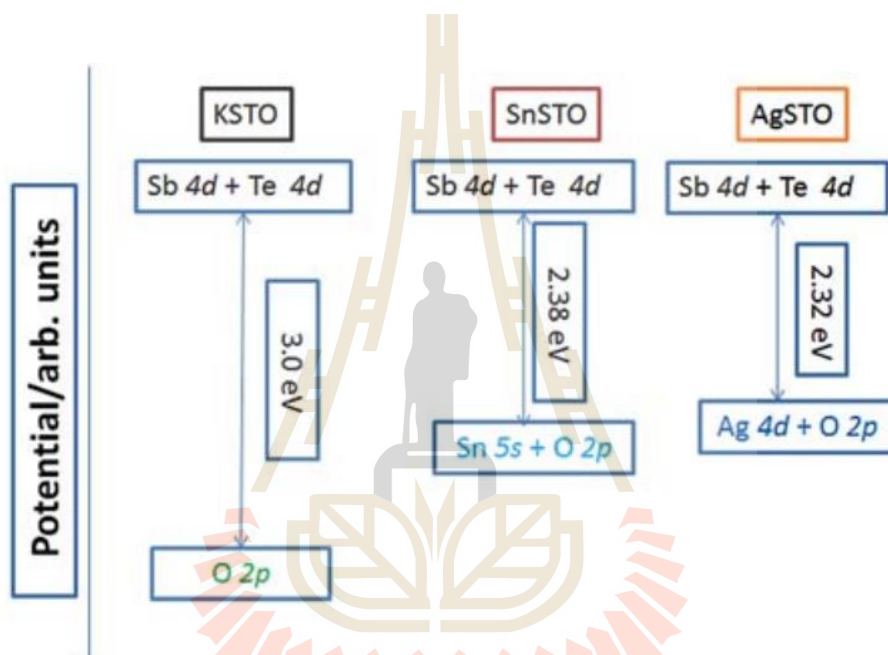


Figure 2.3 Schematic diagram of energy band structure of KSTO, SnSTO and AgSTO (Guje et al., 2015).

Photocatalytic efficiency and photodegradation mechanism of cubic defect pyrochlores oxides have been investigated (Guje et al., 2016; Guje, et al., 2015). Venkataswamy et al. (Venkataswamy et al., 2018) have prepared KTaTeO_6 nanoparticle (KTTO) and Ag doped KTaTeO_6 (ATTO) with defect pyrochlore structure by solid-state and ion-exchange methods, respectively. The results show that substituting K^+ with Ag^+ decrease the bandgap energy (E_g) from 2.47 eV (KTTO) to

2.14 eV for ATTO. The red shift of the absorption edge of ATTO was due to the overlap of Ag 4d states with O 2p states (Figure 2.4). Degradation of methyl violet (MV) and solar water splitting reactions of KTTO and ATTO were investigated. In both cases, ATTO showed higher photocatalytic activity than KTTO. Besides the lower E_g , the higher surface area, more surface hydroxyl groups, and stronger light absorption in visible region were additional factors for the high activity observed in ATTO.

The active species in the photocatalytic degradation of MV was detected by using benzoquinone (BQ, 2 mM), ammonium oxalate (AO, 2 mM), and iso-propanol (IPA, 2 mM) as scavengers. The concentration of generated h^+ was much less than those of $\bullet O_2^-$ and $\bullet OH$ species. Therefore, it was concluded that $\bullet O_2^-$ and $\bullet OH$ are the main active species in the photocatalytic degradation of MV (Venkataswamy et al., 2018). The mechanism of photodegradation of MV is shown in Figure 2.4. The other Te-containing defect pyrochlores used as photocatalysts for dye degradation are listed in Table 2.2.

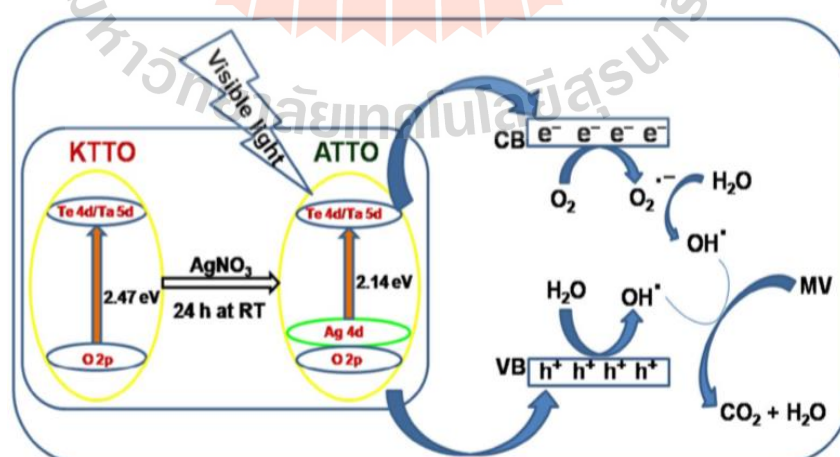


Figure 2.4 Schematic representation of photocatalytic mechanism of MV over ATTO catalyst (Venkataswamy et al., 2018).

Table 2.2 List of Te-containing defect pyrochlores used as photocatalysts for dye degradation.

Catalayst	Bandgap (eV)	Dye degraded	Reference
$\text{KAl}_{0.33}\text{Te}_{1.67}\text{O}_6$	2.09		
$\text{KCr}_{0.33}\text{Te}_{1.67}\text{O}_6$	1.25	MB and MV	(Guje et al., 2015)
$\text{KFe}_{0.33}\text{Te}_{1.67}\text{O}_6$	1.92		
$\text{KSn}_{0.5}\text{Te}_{1.5}\text{O}_6$	2.95		
$\text{AgSn}_{0.5}\text{Te}_{1.5}\text{O}_6$	2.30		
$\text{Cu}_{0.5}\text{Sn}_{0.5}\text{Te}_{1.5}\text{O}_6$	2.44	MB and MV	(Guje et al., 2016)
$\text{Sn}_{0.5}\text{Sn}_{0.5}\text{Te}_{1.5}\text{O}_6$	2.80		
$\text{KTi}_{0.5}\text{Te}_{1.5}\text{O}_6$	2.96		
$\text{AgTi}_{0.5}\text{Te}_{1.5}\text{O}_6$	2.55	MB and MV	(Guje et al., 2016)
$\text{Sn}_{0.5}\text{Ti}_{0.5}\text{Te}_{1.5}\text{O}_6$	2.40		

However, several researches have investigated that Nb-containing pyrochlore oxides are good photocatalysts such as $\text{K}_2\text{Nb}_2\text{O}_6$, CsNbWO_6 and Sn-doped KNbWO_6 (Jitta et al., 2015; Zeng et al. 2018). Yin et al. (2004) have compared photocatalytic activity of Nb-containing and Ta-containing photocatalyst and found that the Nb-containing oxide show higher photocatalytic activity than Ta-containing one because charge carriers in Nb can migrate easier (Yin et al., 2004). Moreover Sergio et al. (2018) have studied crystal structure of KNbTeO_6 , KNbWO_6 , and KSbWO_6 . The possess of interleaved $\text{K}_2\text{O}'$ network in KNbWO_6 , leads to the presence of water molecules within crystal lattice, which pushes K^+ close to 16c sites. On the other hand, extra H_2O molecules are absent in KNbTeO_6 and KSbWO_6 and the K^+ ions are along 32e sites. From the structure data, they have forecasted that K^+ in KNbTeO_6 and

KSbWO₆ are easier to exchange with other ions than KNbWO₆ (Sergio et al., 2018). Thus in this part, the current work focuses on synthesis and photocatalytic activity of KNbTeO₆ and Ag⁺, Cu²⁺ and Sn²⁺ doped KNbTeO₆.

2.3 References

- Guje, R., Gundeboina, R., Kadari, R., Sreenu, K., Reddy, C., Malathi, M., and Vithal, M. (2016). Synthesis, characterization and photocatalytic activity studies of tellurium containing defect pyrochlores, MSn_{0.5}Te_{1.5}O₆ (M= K, Ag, Cu_{0.5} and Sn_{0.5}). **Indian Journal of Chemistry**. 55A: 1174-1181.
- Guje, R., Gundeboina, R., Reddy, J. R., Veldurthi, N. K., Kurra, S., and Vithal, M. (2016). Synthesis, Characterization and Photocatalytic Activity of Ag⁺ and Sn²⁺-Doped KTi_{0.5}Te_{1.5}O₆. **Photochemistry and Photobiology**. 92(2): 223-230.
- Guje, R., Ravi, G., Palla, S., Rao, K. N., and Vithal, M. (2015). Synthesis, characterization, photocatalytic and conductivity studies of defect pyrochlore KM_{0.33}Te_{1.67}O₆ (M= Al, Cr and Fe). **Materials Science and Engineering: B**. 198: 1-9.
- Guje, R., Shrujana, P., Veldurthi, N. K., Gundeboina, R., Kappera, N. R., and Muga, V. (2015). Synthesis, characterisation and photocatalytic activity of Ag⁺-and Sn²⁺-substituted KSbTeO₆. **Chemical Papers**. 69(2): 269-278.
- Hamani, D., Mirgorodsky, A., Masson, O., Merle-Méjean, T., Colas, M., Smirnov, M., and Thomas, P. (2011). Crystal chemistry peculiarities of Cs₂Te₄O₁₂. **Journal of Solid State Chemistry**. 184(3): 637-643.
- Ikeda, S., Itani, T., Nango, K., and Matsumura, M. (2004). Overall water splitting on

- tungsten-based photocatalysts with defect pyrochlore structure. **Catalysis Letters**. 98(4): 229-233.
- Jitta, R. R., Guje, R., Veldurthi, N. K., Prathapuram, S., Velchuri, R., and Muga, V. (2015). Preparation, characterization and photocatalytic studies of N, Sn-doped defect pyrochlore oxide $\text{KTi}_{0.5}\text{W}_{1.5}\text{O}_6$. **Journal of Alloys and Compounds**. 618: 815-823.
- Jitta, R. R., Gundeboina, R., Veldurthi, N. K., Guje, R., and Muga, V. (2015). Defect pyrochlore oxides: as photocatalyst materials for environmental and energy applications-a review. **Journal of Chemical Technology & Biotechnology**. 90(11): 1937-1948.
- Li, J., Siritanon, T., Stalick, J. K., Sleight, A. W., and Subramanian, M. (2011). Structural studies and electrical properties of Cs/Al/Te/O phases with the pyrochlore structure. **Inorganic Chemistry**. 50(12): 5747-5754.
- Loopstra, B., and Goubitz, K. (1986). The structures of four caesium tellurates. **Acta Crystallographica Section C**. 42(5): 520-523.
- Marschall, R., Mukherji, A., Tanksale, A., Sun, C., Smith, S. C., Wang, L., and Lu, G. Q. M. (2011). Preparation of new sulfur-doped and sulfur/nitrogen co-doped CsTaWO_6 photocatalysts for hydrogen production from water under visible light. **Journal of Materials Chemistry**. 21(24): 8871-8879.
- Sergio, M., Falcón, H., Fernández-Díaz, M., and Alonso, J. (2018). The Crystal Structure of Defect $\text{KBB}'\text{O}_6$ Pyrochlores (B, B': Nb, W, Sb, Te) Revisited from Neutron Diffraction Data. **Crystals**. 8(10): 368.
- Ravi, G., Palla, S., Veldurthi, N. K., Reddy, J., Padmasri, H., and Vithal, M. (2014). Solar water-splitting with the defect pyrochlore type of oxides $\text{KFe}_{0.33}\text{W}_{1.67}\text{O}_6$

- and $\text{Sn}_{0.5}\text{Fe}_{0.33}\text{W}_{1.67}\text{O}_6 \cdot x\text{H}_2\text{O}$. **International Journal of Hydrogen Energy**. 39(28): 15352-15361.
- Ravi, G., Shrujana, P., Palla, S., Reddy, J., Guje, R., Velchuri, R., and Vithal, M. (2014). Enhanced photoactivity in nitrogen-doped $\text{KM}_{0.33}\text{W}_{1.67}\text{O}_6$ (M= Al and Cr). **Micro & Nano Letters**. 9(1): 11-15.
- Ravi, G., Veldurthi, N. K., Palla, S., Velchuri, R., Pola, S., Reddy, J. R., and Vithal, M. (2013). Synthesis, characterization and photocatalytic activity of $\text{KAl}_{0.33}\text{W}_{1.67}\text{O}_6$ and $\text{Sn}_{0.5}\text{Al}_{0.33}\text{W}_{1.67}\text{O}_6 \cdot x\text{H}_2\text{O}$. **Photochemistry and Photobiology**. 89(4): 824-831.
- Ravi, G., Veldurthi, N. K., Prasad, M. D., Muniratnam, N., Prasad, G., and Vithal, M. (2013). Preparation, optical, and photocatalytic studies of defect pyrochlores: $\text{KCr}_{0.33}\text{W}_{1.67}\text{O}_6$ and $\text{A}_x\text{Cr}_{0.33}\text{W}_{1.67}\text{O}_6 \cdot n\text{H}_2\text{O}$. **Journal of Nanoparticle Research**. 15(9): 1939.
- Reddy, J., Ravi, G., Veldurthi, N. K., Velchuri, R., Pola, S., Vithal, M., and Sreedhar, B. (2013). Sol-Gel Synthesis and Photocatalytic Study of Visible Light Active N-Doped KSbWO_6 . **Zeitschrift für Anorganische und Allgemeine Chemie**. 639(5): 794-798.
- Siritanon, T., Laurita, G., Macaluso, R. T., Millican, J. N., Sleight, A. W., and Subramanian, M. (2009). First observation of electronic conductivity in mixed-valence tellurium oxides. **Chemistry of Materials**. 21(23): 5572-5574.
- Siritanon, T., Li, J., Stalick, J., Macaluso, R., Sleight, A., and Subramanian, M. (2011). $\text{CsTe}_2\text{O}_{6-x}$: Novel Mixed-Valence Tellurium Oxides with Framework-Deficient Pyrochlore-Related Structure. **Inorganic Chemistry**. 50: 8494-501.
- Siritanon, T., Sleight, A., and Subramanian, M. (2011). Compositionally controlled

- rhombohedral to cubic phase transition in $\text{CsTe}_{2-x}\text{W}_x\text{O}_6$ related to pyrochlore structure. **Materials Research Bulletin**. 46(12): 2494-2496.
- Uma, S., Singh, J., and Thakral, V. (2009). Facile room temperature ion-exchange synthesis of Sn^{2+} incorporated pyrochlore-type oxides and their photocatalytic activities. **Inorganic Chemistry**. 48(24): 11624-11630.
- Venkataswamy, P., Reddy, C. S., Gundeboina, R., Sadanandam, G., Veldurthi, N. K., and Vithal, M. (2018). Nanostructured KTaTeO_6 and Ag-doped KTaTeO_6 Defect Pyrochlores: Promising Photocatalysts for Dye Degradation and Water Splitting. **Electronic Materials Letters**. 14(4): 446-460.
- Yin, J., Zou, Z., and Ye, J. (2004). Possible role of lattice dynamics in the photocatalytic activity of $\text{BaM}_{1/3}\text{N}_{2/3}\text{O}_3$ ($\text{M} = \text{Ni}, \text{Zn}$; $\text{N} = \text{Nb}, \text{Ta}$). **The Journal of Physical Chemistry**. 108(26): 8888-8893.
- Xu, Z., Chen, Y., Jiao, S., Fang, Z., Wang, B., Pang, G., and Feng, S. (2018). Sn-Doped defect pyrochlore oxide $\text{KNbWO}_6 \cdot \text{H}_2\text{O}$ microcrystals and their photocatalytic reduction of CO_2 . **New Journal of Chemistry**. 42(8): 5753-58.

CHAPTER III

ELECTRICAL PROPERTIES OF $AAl_{0.33}Te_{1.67}O_6$ (A = K, Rb, AND Cs) MIXED VALENCE PYROCHLORES

3.1 Abstract

To study the effects of K, Rb and Cs on electronic properties of tellurium containing defect pyrochlore oxide, $Cs_{1-x}A_xAl_{0.33}Te_{1.67}O_6$ (A = K and Rb) were prepared by solid state method. The substitution of Cs with smaller Rb and K reduces cell parameters of the compounds but does not affect the overall structure. The conductivities at 300 K vary from 0.1 S.cm in $CsAl_{0.33}Te_{1.67}O_6$ to 3×10^{-5} and 3×10^{-7} S.cm in $RbAl_{0.33}Te_{1.67}O_6$ and $KAl_{0.33}Te_{1.67}O_6$, respectively. X-ray photoelectron spectroscopy (XPS) confirms that all samples contain Te^{4+}/Te^{6+} mixed valency which is the origin of their *n*-type conduction. To understand the large differences in electronic conductivities, UV-Vis spectra, XPS spectra at valence band region and activation energies of conduction are used to proposed the band structure diagrams which suggest that the conductivities were determined by the energy difference between the defect levels originated from Te^{4+} and the bottom of conduction band. Such differences are affected by Rb and K content in the structure as they seem to increase the band gap energy and lower the top of valence band.

3.2 Introduction

The structures and properties of oxides containing heavy post transition elements are interesting. The presence of diffused *s* orbitals results in wide conduction bands and low carrier mobility, thus giving rise to good electronic conductivity (Kawazoe et al., 2000). Some well-known examples include In_2O_3 , ZnSnO_3 , and $\text{Ba}_{1-x}\text{K}_x\text{BiO}_3$ (Cai et al., 2016; Noguchi and Sakata, 1980; Sato et al., 1991). However, tellurium is one of post transition element but the electron conduction in tellurium oxides are very rare. The only clear examples are series of defect pyrochlores with general formula $\text{Cs}(\text{M},\text{Te})_2\text{O}_6$; $\text{M} = 2+, 3+$ and $4+$ cations which show *n*-type semiconducting behavior due to $\text{Te}^{4+}/\text{Te}^{6+}$ mixed valency (Siritanon et al., 2009).

It has been investigated that $\text{CsAl}_{0.33}\text{Te}_{1.67}\text{O}_6$ shows relatively high conductivity comparing to $\text{Cs}(\text{M},\text{Te})_2\text{O}_6$ series (Siritanon et al., 2009). Li et al. (Li et al., 2011) concluded that the conductivity comes from small deviations from stoichiometry which results in small amount of Te^{4+} producing mixed valence compounds. Therefore, the *n*-type behavior of compounds in these series is explained by the presence of donor defect levels from Te^{4+} . In addition, type of M cations in $\text{Cs}(\text{M},\text{Te})_2\text{O}_6$ affects the conductivity of the compounds as small M cation reduces M/Te-O distance thus destabilizes Te^{4+} in the structure and increase their energy level. Moreover, some M cations can provide orbitals with appropriate energy to overlap with Te 5*s* at conduction band which increases the conductivity. Nevertheless, the role of Cs in the structure remains unclear. Thus, the objectives of this work are to deepen the understanding of these series of oxides and to study the effects of cations at Cs position on the electronic properties of the compounds in $\text{Cs}_{1-x}\text{A}_x\text{Al}_{0.33}\text{Te}_{1.67}\text{O}_6$; $\text{A} =$

Rb and K series.

3.3 Experiments

3.3.1 Preparation of $\text{Cs}_{1-x}\text{A}_x\text{Al}_{0.33}\text{Te}_{1.67}\text{O}_6$; A = Rb and K (x = 0.0, 0.2, 0.4, 0.8, and 1.0)

All samples were prepared by solid state reaction. The reactants were CsNO_3 (Sigma-Aldrich, 99+%), RbNO_3 (Acros Organic, 99.8%), KNO_3 (Carlo Erba, 99+%), Al_2O_3 (Acros organic, 99+ %, for Rb-doped series), $\text{Al}(\text{OH})_3$ (Acros Organic, 99.9%, for K-doped series) and TeO_2 (Acros Organic, 99+%). Stoichiometric mixtures of the reactants were weighed and ground in an agate mortar and heated to 500°C for 5 h. After that, the samples were reground and sintered at 625°C for 12 h in air.

3.3.2 Characterizations and Electrical properties

Powder X-ray diffraction (XRD) patterns were recorded by a Bruker D2 Phaser diffractometer (Cu $K\alpha$ radiation, $\lambda = 1.5406 \text{ \AA}$) for phase identification. The X-ray Photoelectron Spectra (XPS) of Cs 3*d*, Rb 3*d*, K 2*p*, Al 1*s*, Te 3*d* and valence band (VB) were recorded by a PHI5000 VersaProbe II XPS instruments (ULVAC-PHI, Japan) (Monochromatic X-ray of Al $K\alpha = 1486.6 \text{ eV}$) at SUT-NANOTEC-SLRI joint research facility, Synchrotron Light Research Institute (SLRI), Thailand. The binding energies drift due to charging effects were corrected using the position of the C1*s* as a reference at 284.8 eV (Howng et al., 1980; Lv et al., 2016). Agilent UV-Vis-NIR spectrophotometer modeled Carry 5000 was used for optical diffuse reflectance spectroscopy (DRS). The diffuse reflectance (%R) spectra were recorded in the wavelength range of 200-2000 nm with the double beam mode.

Band gap energy was obtained by extrapolation of the plot of $(Kh\nu)^{1/2}$ versus photon energy ($h\nu$), where K is reflectance transformed according to Kubelka–Munk function $[K = (1 - R)^2/2(R)]$, where $R = (\%R_{\text{sample}}/\%R_{\text{standard}})$ (Guje et al., 2015; Morales et al., 2007). The electrical conductivities of all sintered samples were measured from 300 to 673 K by four-probe method using Keysight B2901A source/measure unit.

3.4 Calculations

The density of states (DOS) were calculated based on density functional theory (DFT) using the Vienna *ab initio* simulation package (VASP) (Fuchs et al., 2007; Kresse and Hafner, 1993) employing the Perdew, Burke, Ernzerhof (PBE) exchange-correlation function implemented with the projector augmented-wave method (PAW) (Blöchl, 1994; Kresse and Joubert, 1999). Γ -centered $3 \times 3 \times 2$ Monkhorst-Pack k-mesh was used for the Brillouin zone integrations. The cutoff energy for plane-wave basis sets was set at 520 eV. Structural relaxation was performed until the force on each ion is less than 0.01 eV/Å.

3.5 Results and discussions

3.5.1 Crystal Structure

Powder X-ray diffraction patterns (XRD) of all samples were recorded for phase identification as shown in Figure 3.1. All diffraction peaks of $AA_{0.33}Te_{1.67}O_6$; (A= Cs, Rb and K) can be indexed as AB_2O_6 cubic defect pyrochlore with $Fd\bar{3}m$ space group and no impurity is observed (Subramanian et al., 1983). Based on defect pyrochlore structure, the lattice is built up of $(Al,Te)_2O_6$ corner sharing octahedral creating hexagonal tunnel. The A cations (Cs, Rb, and K) are situated in

these tunnels. Comparing to $A_2B_2O_7$ ($A_2B_2O_6O'$) pyrochlore, AB_2O_6 defect pyrochlore structure has vacancies at A and O' sites. In addition, there are few possibilities of crystallographic sites for A cations. The XRD patterns in this work suggest that they are at the normal 8b position but small deviation from this ideal position, like the 32e position, is also possible.

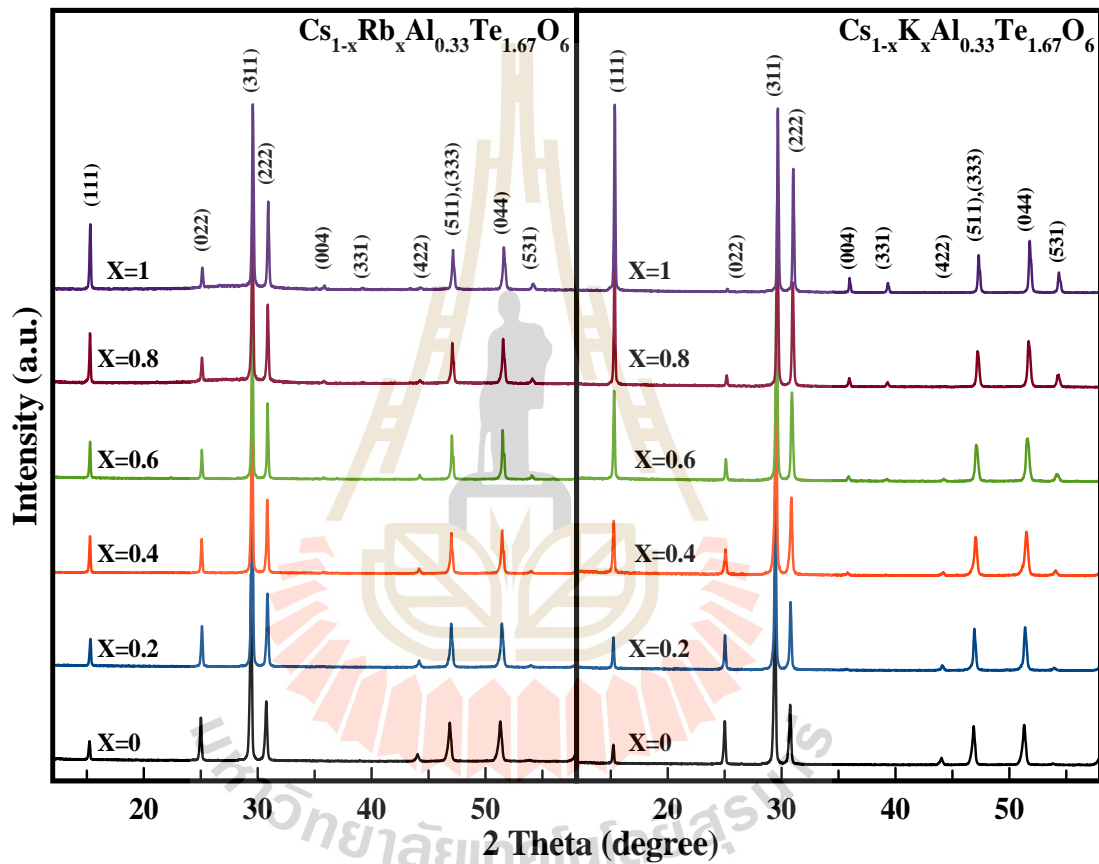


Figure 3.1 XRD patterns of $Cs_{1-x}Rb_xAl_{0.33}Te_{1.67}O_6$ and $Cs_{1-x}K_xAl_{0.33}Te_{1.67}O_6$.

It is worth to note that the disorder of A cation in AB_2O_6 defect pyrochlore from 8b to 32e position results in a nonlinear of plot cell parameter versus the ionic radii of A cation when increasing of cell parameters in $AA_{0.33}W_{1.67}O_6$; A = Cs, Rb, and K (Thorogood et al., 2009). On the other hand, such disorder is not observed in this work although the samples are quite similar. Figure 3.2 displays plots

of cell parameter versus the substituting content. As both K^+ (1.51 Å) and Rb^+ (1.61 Å) are smaller than Cs^+ (1.74 Å), increasing their content results in smaller cell parameters (Shannon et al.,1976; Shannon et al.,1969). However, Castro and Rasines (Castro et al., 1989) have reported that the changing of A cations has a much smaller effect on the cell parameters comparing to changing the B cations, because the main network of the AB_2O_6 structure is created by the B_2O_6 octahedral network.

Thus, it is concluded that replacing Cs with Rb and K do not change the general structure and crystallographic sites for A cations. Additionally, the amount of Rb and K can be varied from zero to one forming a complete series of solid solution.

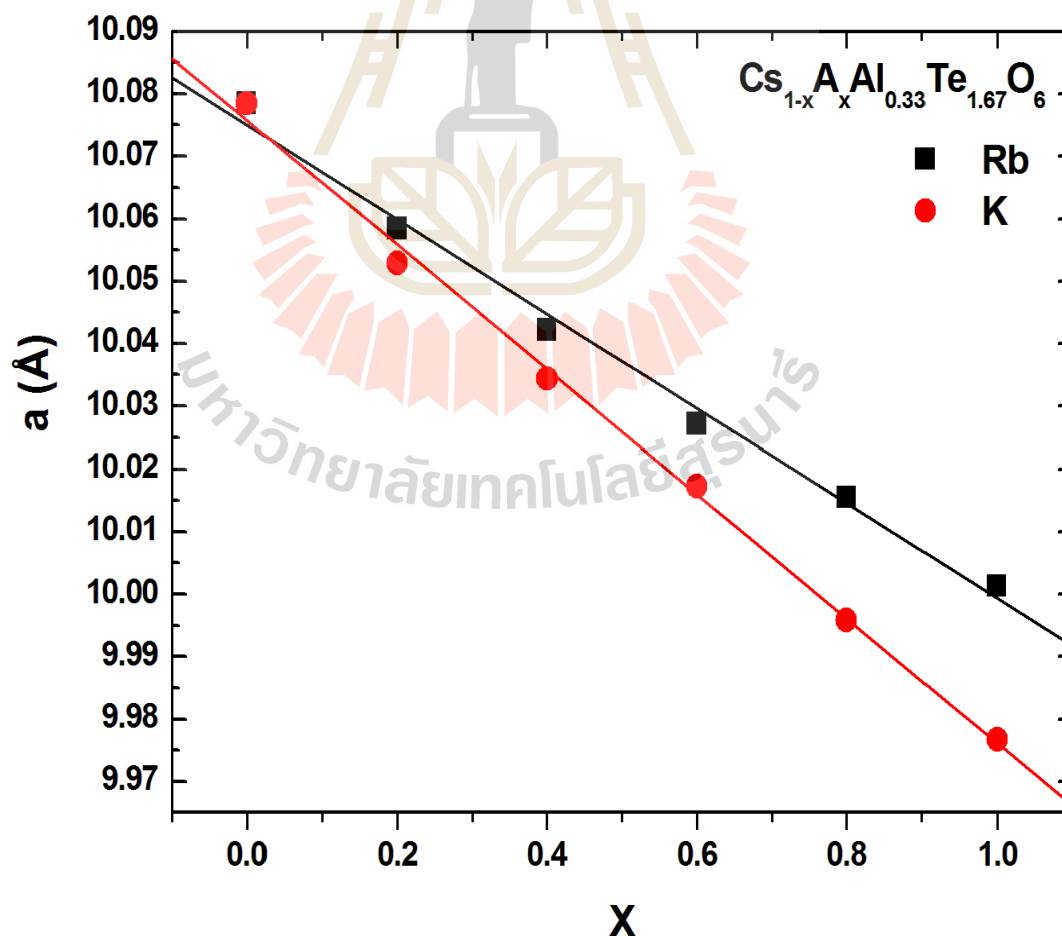


Figure 3.2 Plots of cell parameters versus Rb and K content.

3.5.2 X-ray photoelectron spectroscopy (XPS) results

The XPS survey spectra of CsAl_{0.33}Te_{1.67}O₆ (CATO), RbAl_{0.33}Te_{1.67}O₆ (RATO), and KAl_{0.33}Te_{1.67}O₆ (KATO) show in Figure 3.3 agree well with elemental composition of each compound. The XPS spectra of Cs 3*d*, Rb 3*d*, K 2*p*, and Al 1*s* show semi-quantitative results on the composition of the prepared samples (Figure 3.4). The intensity of Cs 3*d* peaks in both series decreases while the intensity of Rb 3*d* and K 2*p* peaks increase with increasing Rb and K content, respectively. On the other hand, the intensity of Al 1*s* is unchanged. The trend in peak intensity of each element in the samples agrees well with their nominal composition and the starting composition of the prepared samples. In addition, the obtained binding energies of Cs 3*d*, Rb 3*d*, K 2*p*, and Al 1*s* are close to those reported in literature (Atuchin et al., 2012; Guo et al., 2012; Kumar et al., 2015; Marschall et al., 2011; Ravi et al., 2013; Van den Berghe et al., 2000).

Te 3*d* XPS spectra were also investigated to probe oxidation states of Te in the samples. Figure 3.5 show Te 3*d* XPS spectra of CATO, RATO and KATO comparing to that of CsTe₂O₆ (CTO). These spectra are fitted using two Gaussian-Lorentzian peaks; one represents Te⁴⁺ at lower binding energy and the other represents Te⁶⁺. For comparison, Te 3*d* spectrum of (CTO), a known compound which contains both Te⁴⁺ and Te⁶⁺ is also shown. The Te 3*d*_{5/2} binding energies of the observed Te⁶⁺ are close to the reported values (Sathiya et al., 2013). However, the binding energies of Te⁴⁺ in AAl_{0.33}Te_{1.67}O₆ (A = K, Rb, and Cs) are slightly lower than most reported values for Te⁴⁺ (Sathiya et al., 2013; Tan et al., 2004) but are higher than Te(0) or Te²⁻ states (Sartz et al., 1971). The chemical environments affect the binding energy. Thus, Te⁴⁺ in these samples, which is compressed in octahedral, are expected

to be different from that of Te^{4+} in TeO_2 standard. In fact, our values are close to that reported in $\text{Gd}_2(\text{Ti}_{2-y}\text{Te}_y)\text{O}_7$ pyrochlores which similarly contain compressed Te^{4+} (Heredia et al., 2010). The binding energy and peak area of each peak are summarized in Table 3.1.

In addition, $\text{Te } 3d_{5/2}$ XPS results reveal the presence of Te^{4+} in all samples with similar peak areas suggesting that Rb and K substituted samples contain a similar amount of defect. However, the presence of Te^{4+} in the cubic pyrochlore samples is very low. The presence of a small amount of Te^{4+} is a result of a small deviation in stoichiometry as reported by Li et al. (Li et al., 2011) who concluded that the nominal $\text{CsAl}_{0.33}\text{Te}_{1.67}\text{O}_6$ was actually $\text{CsAl}_{0.30}\text{Te}_{1.70}\text{O}_6$. The small amount of Te^{6+} must then be reduced to Te^{4+} to maintain charge neutrality.

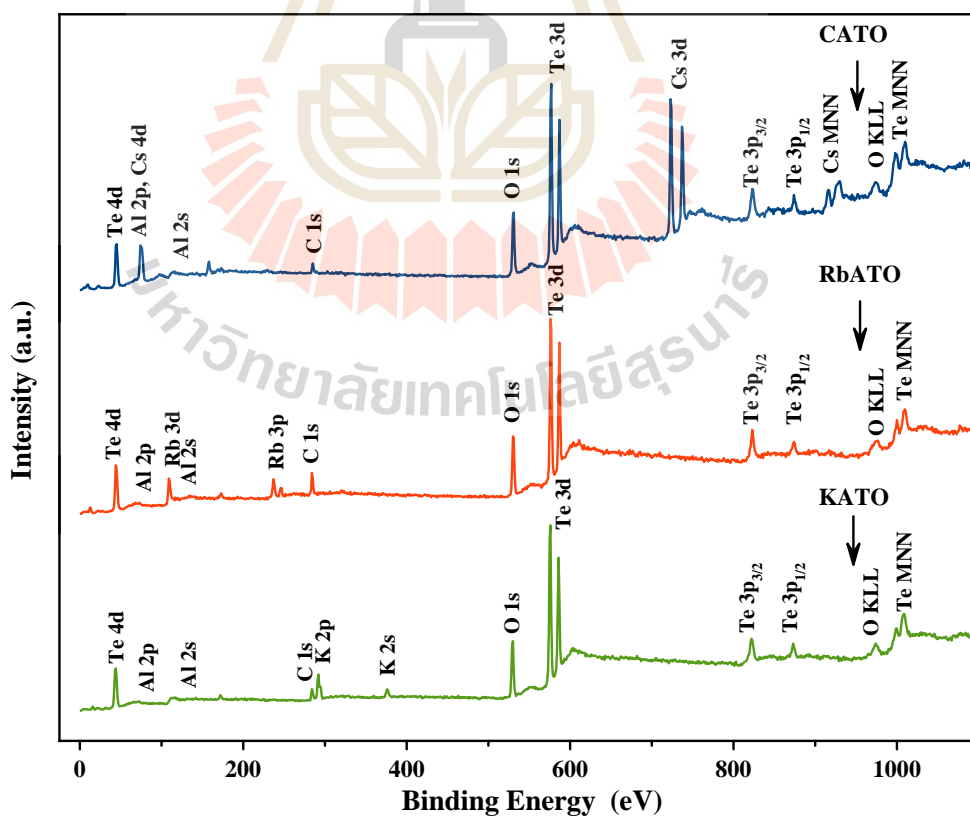


Figure 3.3 XPS survey spectra of CATO, RbATO, and KATO.

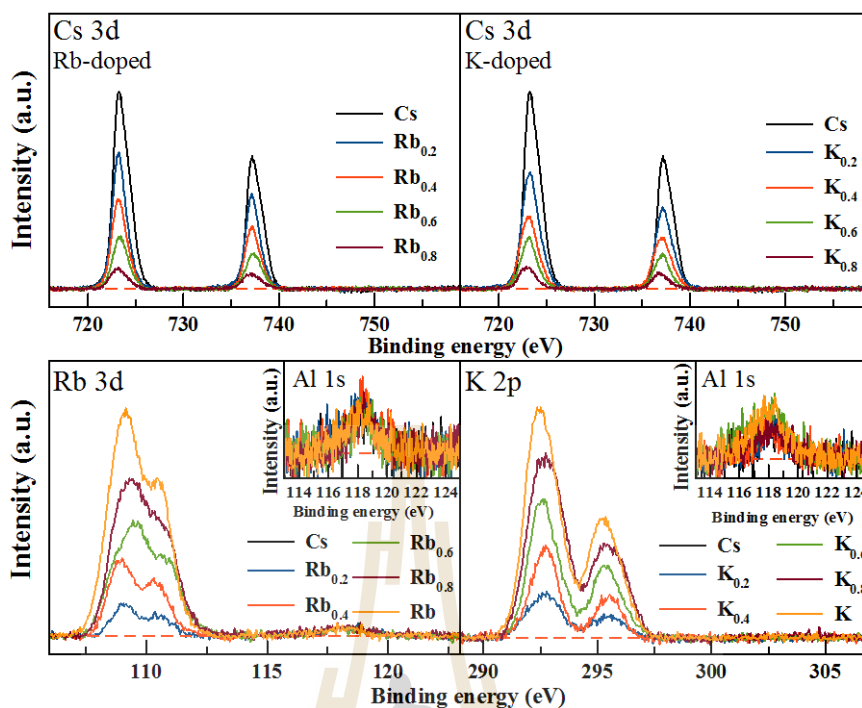


Figure 3.4 Cs 3d, Rb 3d, K 2p and Al 1s XPS spectra of $\text{Cs}_{1-x}\text{Rb}_x\text{Al}_{0.33}\text{Te}_{1.67}\text{O}_6$ and $\text{Cs}_{1-x}\text{K}_x\text{Al}_{0.33}\text{Te}_{1.67}\text{O}_6$.

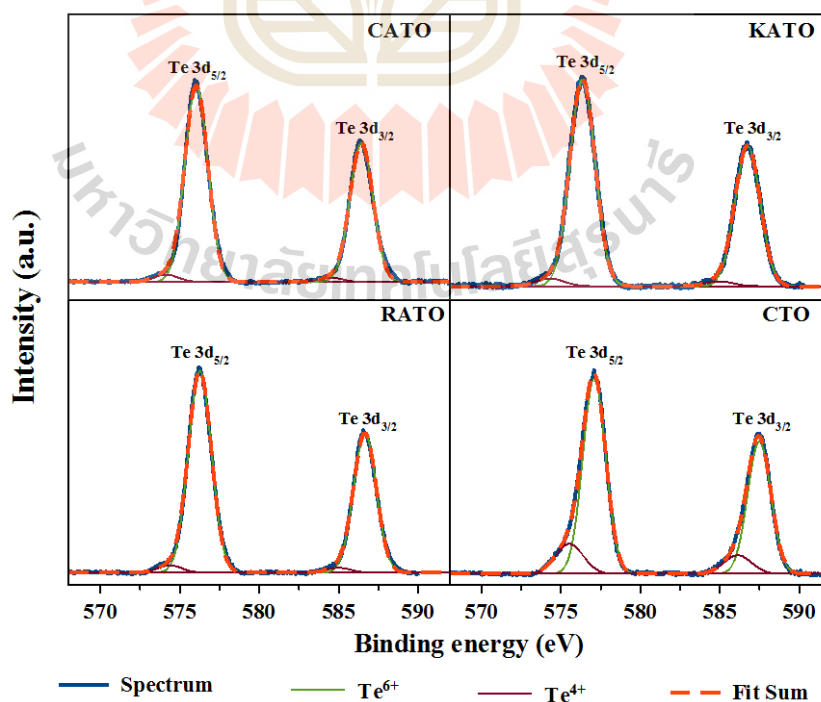


Figure 3.5: XPS Te 3d spectra of CATO, RATO, KATO and CTO.

Table 3.1 Te $3d_{5/2}$ fitting results.

Comp. (X)	Te ⁶⁺		Te ⁴⁺		Ratio of Te ⁶⁺ : Te ⁴⁺ (1.67)	R ²
	B.E.	FWHM	B.E.	FWHM		
	(eV)	(eV)	(eV)	(eV)		
0	576.03	1.70	574.12	1.62	1.62:0.05	0.9983
Rb-doped						
0.2	576.25	1.72	574.19	1.68	1.61:0.06	0.9991
0.4	576.27	1.79	574.22	1.78	1.62:0.05	0.9987
0.6	576.28	2.00	574.25	1.86	1.62:0.05	0.9994
0.8	576.36	1.90	574.28	1.68	1.60:0.07	0.9992
1.0	576.40	1.85	574.28	1.80	1.60:0.07	0.9995
K-doped						
0.2	576.28	1.89	574.29	1.68	1.61:0.06	0.9993
0.4	576.32	1.79	574.33	1.72	1.60:0.07	0.9995
0.6	576.32	1.84	574.34	1.61	1.60:0.07	0.9982
0.8	576.35	2.02	574.43	1.99	1.60:0.07	0.9987
1.0	576.42	1.97	574.46	1.87	1.61:0.06	0.9992
CsTe₂O₆						
-	577.07	1.72	575.50	2.00	1.66:0.44	0.9981
(Te ⁶⁺ _{1.5} : Te ⁴⁺ _{0.5})						

3.5.3 Electronic structure

Figure 3.6(a) show XPS spectra at valence band region that gives useful information about the electronic structure of the samples. Almost all semiconductor oxides consisting of d^0 and d^{10} metal ions, valence bands are usually formed with O $2p$ orbitals (Scaife, 1980). The outstanding feature of the spectra is the position of alkali p orbitals which is at about 10, 13, and 17 eV for Cs $5p$, Rb $4p$, and K $3p$, respectively. The positions of these states are similar to values in other reports (Atuchin et al., 2012; Slobodin et al., 2005; Van den Berghe et al., 2000). Rb $4p$ and K $3p$ bands are quite separated from O $2p$ near the top of the valence band and should not have many contributions in it. Thus, the spectral feature and position of the valence band in Rb and K containing samples are very similar. This also implies that the effects from different bond distances and angles are insignificant, if any. The spectra of two samples containing Cs are similar although there are some differences as both samples contain quite a different composition and the crystal structure. As Cs $5p$ bands are clearly overlapping with O $2p$, Cs is believed to contribute to the valence band. The overlapping between Cs $5p$ and O $2p$ in the valence band is observed in many oxides (Waghmode et al., 2003; Yang et al., 2014). The contribution from Cs $5p$ in the valence band causes the shift in its position comparing to the other two samples with no Cs. In addition, the spectral shape of CTO valence band is different from others and there is another small peak on top of the valence band maximum (VBM) (Figure 3.6(b)).

To understand the electronic structure, the band structure calculation of CTO was performed. The valence band of CTO may be divided into three regions (Figure 3.7). The small peaks at VBM consist of O $2p$ and Te $5s$ orbitals. The wide

region about -1 to -6 eV is a feature of O 2*p* with a small contribution from Te 4*d* orbital and the sharp peak at about -6 to -8 eV is formed mainly by Cs 5*p* orbital with some contribution from Te 5*p*. These main features of the valence band are compared to the obtained XPS spectra. It is interesting to note that the small peak above VBM is not observed in XPS spectra of the $\text{AAI}_{0.33}\text{Te}_{1.67}\text{O}_6$ series. However, as proposed by Li et al (Li et al., 2011) and estimated from Te 3*d*_{5/2} spectra, $\text{AAI}_{0.33}\text{Te}_{1.67}\text{O}_6$ samples should contain only about 3% of Te^{4+} which is very little comparing to 25% in CTO. Thus, it is difficult to see Te 5*s* state at VBM of $\text{AAI}_{0.33}\text{Te}_{1.67}\text{O}_6$. In addition, the different structure may lead to the different position of Te 5*s* state.

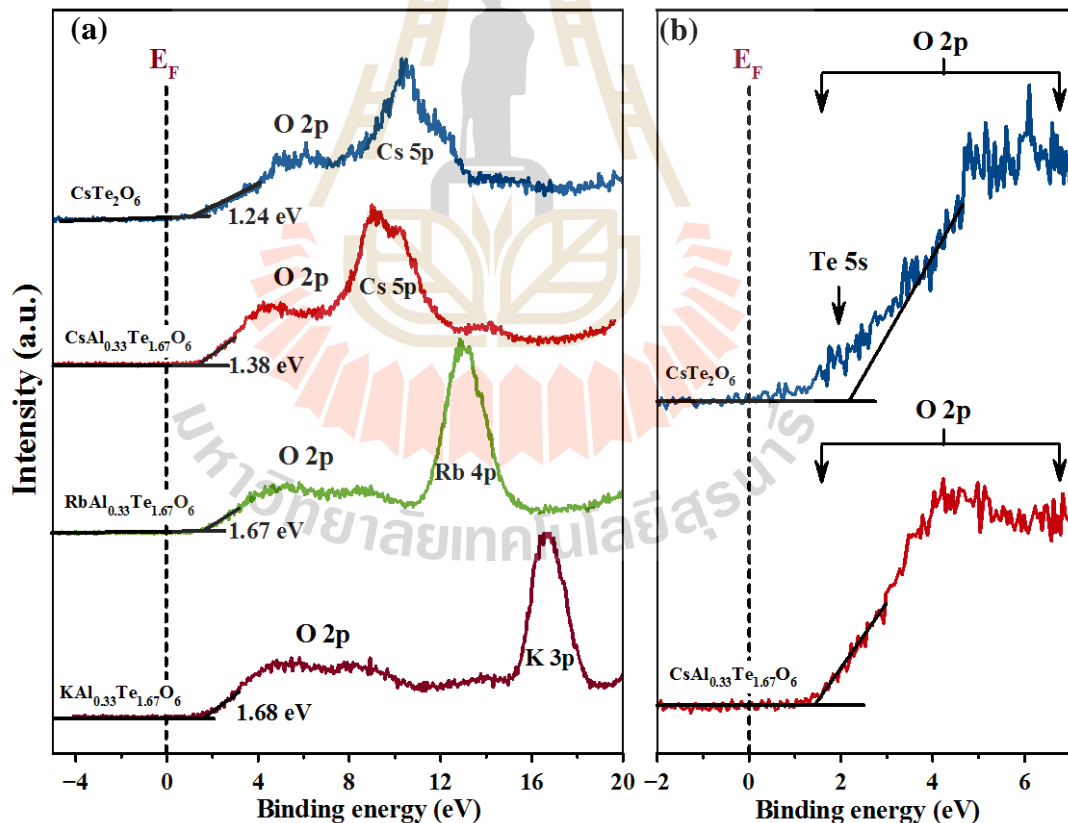


Figure 3.6 XPS valence band spectra of CsTe_2O_6 and $\text{AAI}_{0.33}\text{Te}_{1.67}\text{O}_6$ ($A = \text{Cs, Rb, and K}$) (a) and the close-up of Cs containing samples showing an additional small peak near the Fermi level (b).

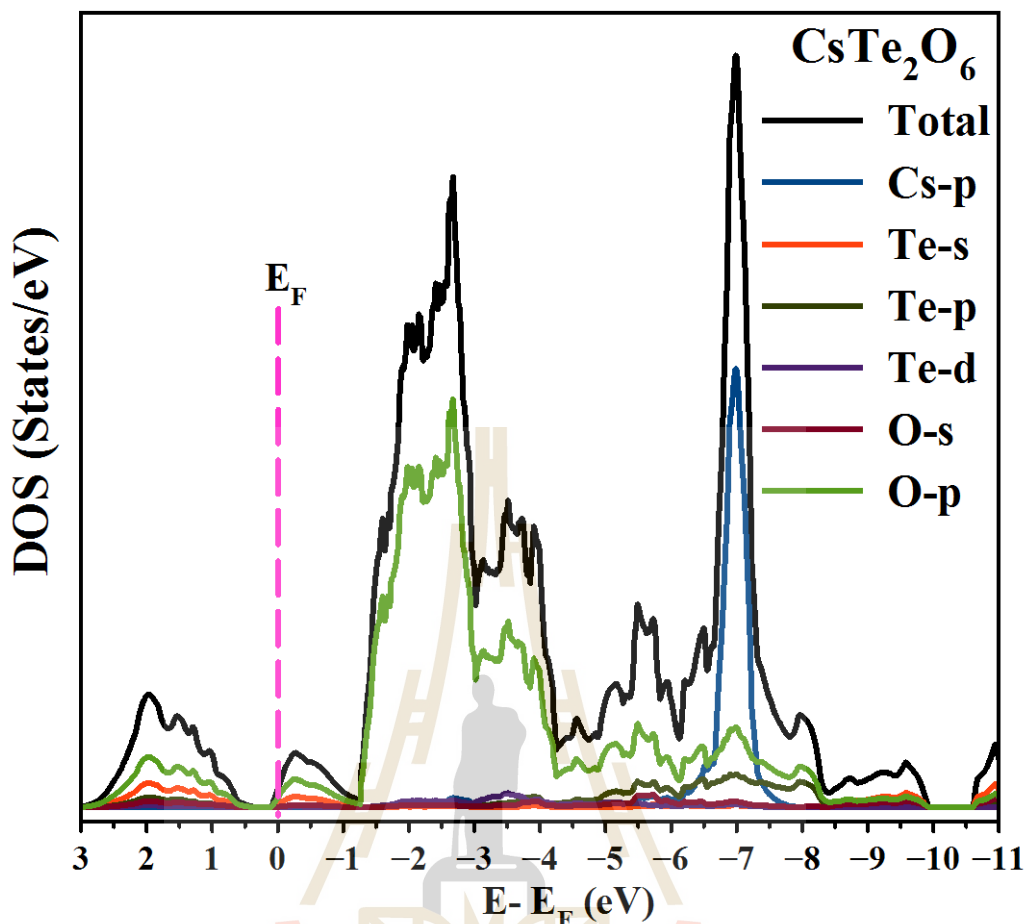


Figure 3.7 The calculated valence band of CsTe_2O_6 .

3.5.4 Optical property

The UV-Vis absorption spectra of CTO and $\text{AAAl}_{0.33}\text{Te}_{1.67}\text{O}_6$ ($A = \text{Cs}$, Rb, and K) and the band gap energy obtained from the extrapolations are shown in Figure 3.8. Although Cs_2O , TeO_2 , and TeO_3 have large band gap and white color, the band gap of CTO is only about 1.4 eV and the compound is dark brown. This small band gap is a result of Te^{4+} and Te^{6+} intervalence charge transfer (IVCT) which gives rise to the absorption in a visible region corresponding to the transition from $\text{Te}^{4+} 5s^2$ to $\text{Te}^{6+} 5s^0$. Even though there are very few reports about $\text{Te}^{4+}/\text{Te}^{6+}$ charge transfer, a similar mechanism is widely studied in other mixed valence systems including those

with post-transition cations like Sb, Sn, Tl (Atkinson and Day, 1969; Mizoguchi et al., 2013).

The UV-Vis spectra of $\text{AAI}_{0.33}\text{Te}_{1.67}\text{O}_6$ series are different from that of CTO although the compounds also contain $\text{Te}^{4+}/\text{Te}^{6+}$ mixed valency. However, Te^{4+} and Te^{6+} in $\text{AAI}_{0.33}\text{Te}_{1.67}\text{O}_6$ are in the same crystallographic sites while those in CTO are in the different ones. As λ_{max} of absorption should be directly related to the energy difference between $\text{Te}^{4+}5s^2$ and $\text{Te}^{6+}5s^0$, the higher similarity of the environment around Te^{4+} and Te^{6+} in $\text{AAI}_{0.33}\text{Te}_{1.67}\text{O}_6$ results in absorptions at a longer wavelength. The very broad and strong absorption centering at long wavelengths of $\text{AAI}_{0.33}\text{Te}_{1.67}\text{O}_6$ is associated with IVCT of Te^{4+} and Te^{6+} similar to the diffuse reflectance spectra of $\text{BaSn}_{1-x}\text{Sb}_x\text{O}_3$ containing $\text{Sb}^{3+}/\text{Sb}^{5+}$ (Mizoguchi et al., 2013).

Thus, it is concluded that the band gap energy obtained from the extrapolations (Figure 3.8(b)) of CTO and $\text{AAI}_{0.33}\text{Te}_{1.67}\text{O}_6$ refer to energies of intervalence charge transfer from $\text{Te}^{4+}5s^2$ to $\text{Te}^{6+}5s^0$ and the transition of valence band (O $2p$) to conduction band, respectively.

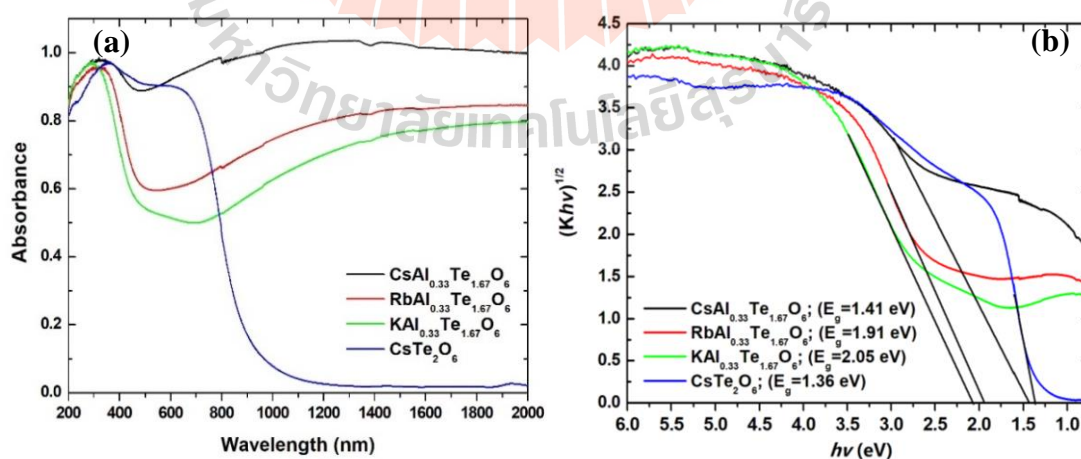


Figure 3.8 UV-Vis spectra (a) and extrapolation of the band gap energy (b) of CsTe_2O_6 and $\text{AAI}_{0.33}\text{Te}_{1.67}\text{O}_6$ (A = Cs, Rb, and K).

3.5.5 Electrical properties

Electronic conductivity of $\text{Cs}_{1-x}\text{A}_x\text{Al}_{0.33}\text{Te}_{1.67}\text{O}_6$ ($\text{A} = \text{Rb}$ and K) decrease with increasing A content. The effect is very significant as room temperature conductivity of $\text{KAl}_{0.33}\text{Te}_{1.67}\text{O}_6$ and $\text{RbAl}_{0.33}\text{Te}_{1.67}\text{O}_6$ are 10^3 and 10^5 times lower than that of $\text{CsAl}_{0.33}\text{Te}_{1.67}\text{O}_6$ (0.1 S.cm), respectively (Figure 3.9). The conductivity of CsTe_2O_6 is too low to be measured at room temperature. The conductivity of all samples are plotted based on Arrhenius' equation: $\sigma = Ae^{(-E_a/kT)}$ where A is pre-exponential constant, k is Boltzmann constant, E_a is activation energy, and T is absolute temperature as shown in Figure 3.9. The activation energy are calculated and summarized in Table 3.2. It is obvious that the lower Cs content, the higher the activation energy. Interestingly, Siritanon et al. (Siritanon et al., 2009) have reported that the Arrhenius plot of $\text{Cs}(\text{M},\text{Te})_2\text{O}_6$ are not linear in temperature range 50-300 K and concluded that the samples exhibit variable range hopping conduction as the plots of log conductivity vs. $1/T^{1/4}$ are linear. Therefore, the samples have different conduction processes at different temperatures. In fact, crossover from variable range hopping conduction to thermally activated band conduction from low to high temperatures have been reported in many systems (Han et al., 2012; Okutan et al., 2005) which is believed to be the case here.

In addition, $\text{CsAl}_x\text{Te}_{2-x}\text{O}_6$ and $\text{RbAl}_x\text{Te}_{2-x}\text{O}_6$ were prepared and their conductivities were measured as shown in Figure A4. The conductivity of both series exhibit similar dependence on Al content which is also in agreement with the previous work (Li et al., 2011). Therefore, it is reasonable to conclude that the amount of defect (Te^{4+}) are similar. If the number of Te^{4+} is similar, the difference in conductivity must be related to Te^{4+} energy level relative to the conduction band.

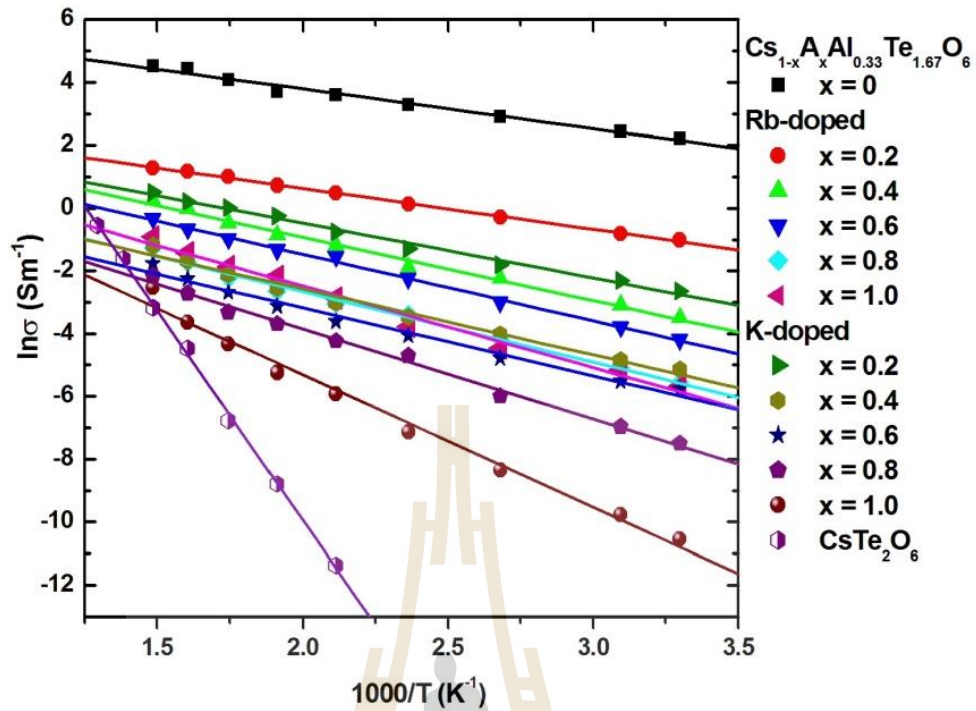


Figure 3.9 Electronic conductivity of $\text{Cs}_{1-x}\text{A}_x\text{Al}_{0.33}\text{Te}_{1.67}\text{O}_6$ ($\text{A} = \text{Rb}$ and K) and CsTe_2O_6 samples fitted with Arrhenius equation.

Table 3.2 Activation energy and R^2 obtained from fitting the electronic conductivity of $\text{Cs}_{1-x}\text{A}_x\text{Al}_{0.33}\text{Te}_{1.67}\text{O}_6$; $\text{A} = \text{Rb}$ and K and CsTe_2O_6 with Arrhenius equation.

x	E_a (eV)	R^2	x	E_a (eV)	R^2
0	0.108	0.9854	CsTe_2O_6	1.15	0.9987
Rb-doped			K-doped		
0.2	0.113	0.9985	0.2	0.151	0.9914
0.4	0.174	0.9921	0.4	0.180	0.9856
0.6	0.183	0.9972	0.6	0.186	0.9855
0.8	0.194	0.9919	0.8	0.247	0.9934
1.0	0.224	0.9870	1.0	0.364	0.9888

3.5.6 Band structure

When Cs is replaced by Rb and K in $\text{Cs}_{1-x}\text{A}_x\text{Al}_{0.33}\text{Te}_{1.67}\text{O}_6$, although the same number of Al and Te^{4+} are present as observed from XPS, the samples containing Rb and K have much less conductivity despite the smaller cell parameters. To explain the large differences in electrical conductivities of $\text{AAI}_{0.33}\text{Te}_{1.67}\text{O}_6$ and CsTe_2O_6 (CTO), the schematic band structure diagrams are proposed using the band gap energy obtained from UV-Vis results and the VBM position obtained from XPS valence band spectra (Figure 3.10). From the figure, the difference between Fermi energy level and the bottom of the conduction band (E_d) is obtained. In general, the band diagrams of these four samples represent their semiconducting behavior. However, the activation energies of conduction indicate that their behavior are different. The activation energy of conduction of CTO (1.15 eV) (Figure 3.9) is in the same order with its band gap energy suggesting the intrinsic semiconducting behavior. The conductivity of this sample is small because it required large energy to activate electrons from valence band to conduction band. It is worth noting that E_d and the activation energy of conduction in CTO are significantly different which indicates that there is no defect level at the Fermi energy level (E_F). On the other hand, the activation energies of $\text{AAI}_{0.33}\text{Te}_{1.67}\text{O}_6$ are close to E_d and much smaller than their band gap energy which suggests the presence of defect levels close to the conduction band within the band gap. The presence of such defect levels is a characteristic of *n*-type semiconductors which agrees well with the negative Seebeck coefficients (Siritanon et al., 2009). E_d in these three samples indicate the position of defect levels relative to conduction band minimum (CBM) which determines conductivity of the samples.

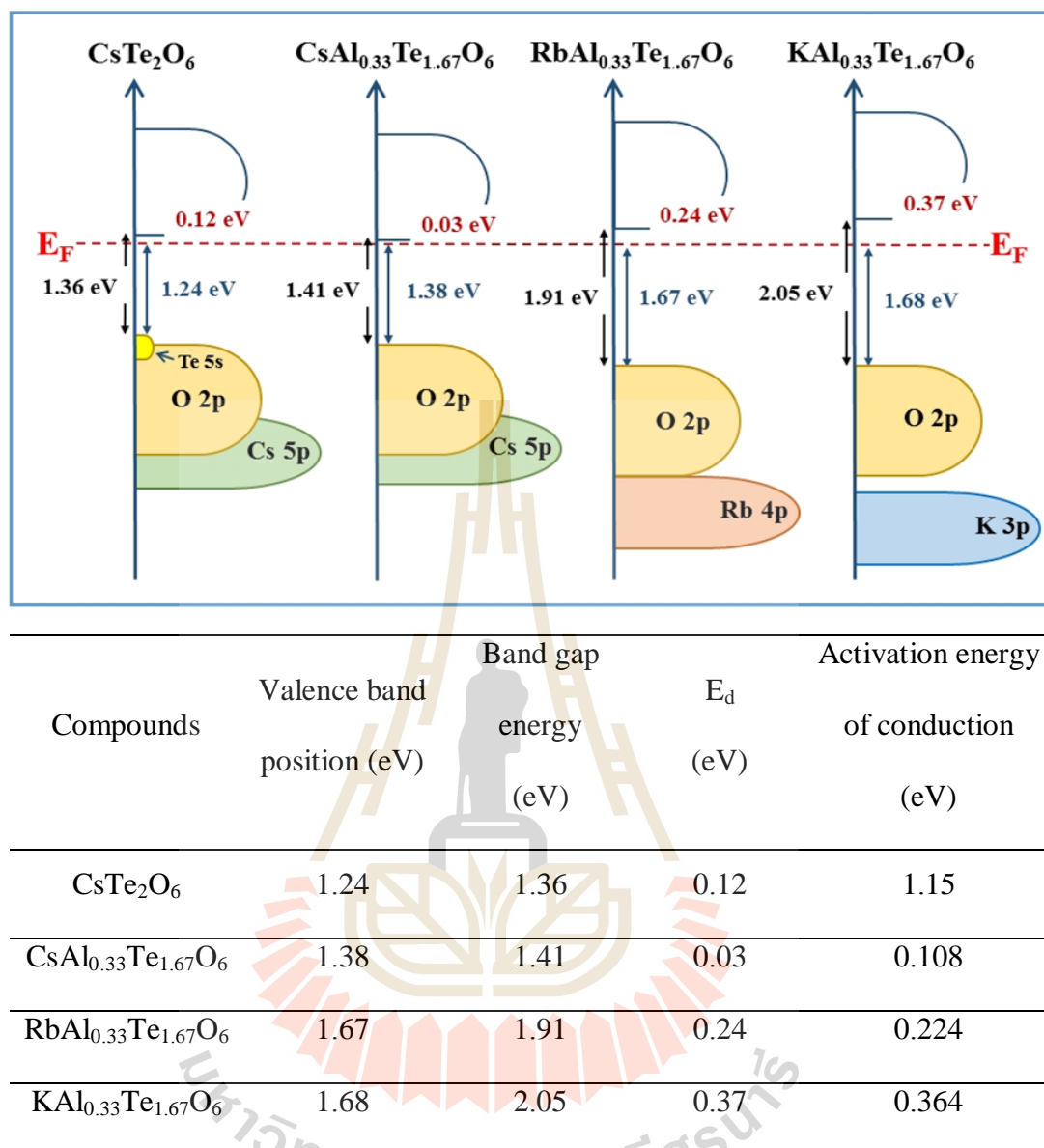


Figure 3.10 Proposed schematic band structures of CsTe_2O_6 and $\text{AAl}_{0.33}\text{Te}_{1.67}\text{O}_6$ (A = Cs, Rb, and K).

Overall, substitutions Cs with Rb and K have two effects on the band diagram; lowering the VBM and lifting the CBM leading to the increases in the band gap energy. Without the presence of Cs, VBM of both RATO and KATO is about 0.3 eV lower in energy. However, the band gap differences between the samples are 0.5-

0.6 eV. Two factors that might affect valence and conduction band edge position are the degree of overlapping and the relative energy level of Al 3s/Te 5s to O 2p, Te/Al-O bond distance and Te/Al-O-Te/Al bond angle (Frاند et al., 1995). As previously reported, replacing with smaller cation at A site of AB₂O₆ defect pyrochlore which leads to a change in the B-O bond distance and B-O-B bond angle (Garcia-Martin et al., 1991; Thorogood et al., 2009). Nevertheless, the combination of VBM lowering and CBM lifting when Cs is replaced with Rb and K result in larger Ed and consequently lower conductivity.

3.6 Conclusion

The series of Cs_{1-x}A_xAl_{0.33}Te_{1.67}O₆ (A = K and Rb) with defect pyrochlore structure have been successfully prepared by solid state reaction. The electrical conductivity of all samples have been measured. Evidences from XPS confirm the Te⁴⁺/Te⁶⁺ mixed valency. Although containing similar Te⁴⁺/Te⁶⁺ mixed valency, the samples with Rb and K are significantly less conductive. To clarify the large differences in electronic conductivities, UV-Vis spectra, XPS spectra at valence band region, and activation energies of conduction are used to proposed the band structure diagrams. The band diagrams indicate that the samples are *n*-type semiconductor. The conductivities were determined by the energy difference between the defect levels originated from Te⁴⁺ and CBM. Such differences are affected by Rb and K content in the structure as they seem to increase the band gap energy by lowering the top of valence band. Additionally, replacing Cs with Rb and K increases energy difference between the defect levels and CBM which consequently result in lower electrical conductivity.

3.7 References

- Atkinson, L., and Day, P. (1969). Charge transfer in mixed-valence solids. Part IV. Electronic spectra of hexachloroantimonates (III, V). **Journal of the Chemical Society A: Inorganic, Physical, Theoretical**. 2423-2431.
- Atuchin, V., Kesler, V., Meng, G., and Lin, Z. (2012). The electronic structure of RbTiOPO₄ and the effects of the A-site cation substitution in KTiOPO₄-family crystals. **Journal of Physics: Condensed Matter**. 24(40): 405503.
- Blöchl, P. E. (1994). Projector augmented-wave method. **Physical Review B**. 50(24): 17953.
- Cai, S., Li, Y., Chen, X., Ma, Y., Liu, X., and He, Y. (2016). Optical and electrical properties of Ta-doped ZnSnO₃ transparent conducting films by sol-gel. **Journal of Materials Science: Materials in Electronics**. 27(6): 6166-6174.
- Castro, A., Rasines, I., and Turrillas, X. (1989). Synthesis, X-ray diffraction study, and ionic conductivity of new AB₂O₆ pyrochlores. **Journal of Solid State Chemistry**. 80(2): 227-234.
- Frand, G., Bohnke, O., Lacorre, P., Fourquet, J., Carré, A., Eid, B., Theobald, J., and Gire, A. (1995). Tuning of Metal/Insulator Transition around Room Temperature of Perovskites Sm_{1-x}Nd_xNiO₃. **Journal of Solid State Chemistry**. 120(1): 157-163.
- Fuchs, F., Furthmüller, J., Bechstedt, F., Shishkin, M., and Kresse, G. (2007). Quasiparticle band structure based on a generalized Kohn-Sham scheme. **Physical Review B**. 76(11): 115109.
- Garcia-Martin, S., Veiga, M., Jerez, A., and Pico, C. (1991). Novel defect pyrochlores M_{0.5}Tl_{0.5}(NbTe)O₆: Preparation and structural characterization. **Materials**

Research Bulletin. 26(8): 789-795.

Guje, R., Ravi, G., Palla, S., Rao, K. N., and Vithal, M. (2015). Synthesis, characterization, photocatalytic and conductivity studies of defect pyrochlore $\text{KM}_{0.33}\text{Te}_{1.67}\text{O}_6$ (M= Al, Cr and Fe). **Materials Science and Engineering: B.** 198: 1-9.

Guo, C., Yin, S., Dong, Q., and Sato, T. (2012). Near-infrared absorption properties of Rb_xWO_3 nanoparticles. **CrystEngComm.** 14(22): 7727-7732.

Han, M., Jiang, K., Zhang, J., Yu, W., Li, Y., Hu, Z., and Chu, J. (2012). Structural, electronic band transition and optoelectronic properties of delafossite $\text{CuGa}_{1-x}\text{Cr}_x\text{O}_2$ ($0 \leq x \leq 1$) solid solution films grown by the sol-gel method. **Journal of Materials Chemistry.** 22(35): 18463-18470.

Heredia, A., García, M. Q., Mazariego, J. P., and Escamilla, R. (2010). X-ray diffraction and Raman spectroscopy on $\text{Gd}_2(\text{Ti}_{2-y}\text{Te}_y)\text{O}_7$ prepared at high pressure and high temperature. **Journal of Alloys and Compounds.** 504(2):446-451.

Howng, W.-Y., and Thorn, R. (1980). Investigation of the electronic structure of $\text{La}_{1-x}(\text{M}^{2+})_x\text{CrO}_3$, Cr_2O_3 and La_2O_3 by X-ray photoelectron spectroscopy. **Journal of Physics and Chemistry of Solids.** 41(1): 75-81.

Kawazoe, H., Yanagi, H., Ueda, K., and Hosono, H. (2000). Transparent *p*-type conducting oxides: design and fabrication of pn heterojunctions. **MRS Bulletin.** 25(8): 28-36.

Kresse, G., and Hafner, J. (1993). Ab initio molecular dynamics for open-shell transition metals. **Physical Review B.** 48(17): 13115.

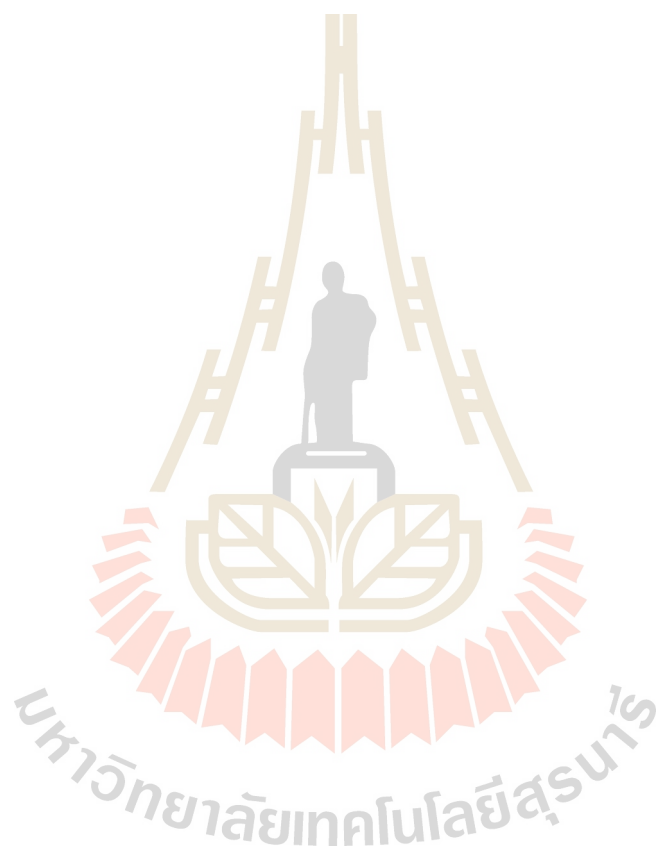
Kresse, G., and Joubert, D. (1999). From ultrasoft pseudopotentials to the projector

- augmented-wave method. **Physical Review B**. 59(3): 1758.
- Kumar, S., Prakash, R., Kumar, V., Bhalerao, G., Choudhary, R., and Phase, D. (2015). Surface and spectral studies of Eu^{3+} doped $\alpha\text{-Al}_2\text{O}_3$ synthesized via solution combustion synthesis. **Advanced Powder Technology**. 26(4): 1263-1268.
- Li, J., Siritanon, T., Stalick, J. K., Sleight, A. W., and Subramanian, M. (2011). Structural studies and electrical properties of Cs/Al/Te/O phases with the pyrochlore structure. **Inorganic Chemistry**. 50(12): 5747-5754.
- Lv, Y., Yao, W., Zong, R., and Zhu, Y. (2016). Fabrication of Wide-Range-Visible Photocatalyst $\text{Bi}_2\text{WO}_{6-x}$ nanoplates via Surface Oxygen Vacancies. **Scientific Reports**. 6: 19347.
- Marschall, R., Mukherji, A., Tanksale, A., Sun, C., Smith, S. C., Wang, L., and Lu, G. Q. M. (2011). Preparation of new sulfur-doped and sulfur/nitrogen co-doped CsTaWO_6 photocatalysts for hydrogen production from water under visible light. **Journal of Materials Chemistry**. 21(24): 8871-8879.
- Mizoguchi, H., Chen, P., Boolchand, P., Ksenofontov, V., Felser, C., Barnes, P. W., and Woodward, P. M. (2013). Electrical and optical properties of Sb-doped BaSnO_3 . **Chemistry of Materials**. 25(19): 3858-3866.
- Morales, A. E., Mora, E. S., and Pal, U. (2007). Use of diffuse reflectance spectroscopy for optical characterization of un-supported nanostructures. **Revista Mexicana de Física**. 53(5): 18-22.
- Noguchi, S., and Sakata, H. (1980). Electrical properties of undoped In_2O_3 films prepared by reactive evaporation. **Journal of Physics D: Applied Physics**. 13(6):1129.

- Okutan, M., Bakan, H. I., Korkmaz, K., and Yakuphanoglu, F. (2005). Variable range hopping conduction and microstructure properties of semiconducting Co-doped TiO₂. **Physica B: Condensed Matter**. 355(1-4): 176-181.
- Ravi, G., Veldurthi, N. K., Palla, S., Velchuri, R., Pola, S., and Reddy, J. R. (2013). Synthesis, characterization and photocatalytic activity of KAl_{0.33}W_{1.67}O₆ and Sn_{0.5}Al_{0.33}W_{1.67}O₆.xH₂O. **Photochemistry and Photobiology**. 89(4): 824-831.
- Sartz, W. E., Wynne, K. J., and Hercules, D. M. (1971). X-ray photoelectron spectroscopic investigation of Group VIA elements. **Analytical Chemistry**. 43(13): 1884-1887.
- Sathiya, M., Ramesha, K., Rousse, G., Foix, D., Gonbeau, D., Guruprakash, K., Prakash, A. S., Doublet, M. L., and Tarascon, J.-M. (2013). Li₄NiTeO₆ as a positive electrode for Li-ion batteries. **Chemical Communications**. 49(97): 11376-11378.
- Sato, H., Ido, T., Tajima, S., Yosida, M., Tanabe, K., and Uchida, S. (1991). Superconducting and normal states of Ba_{1-x}K_xBiO₃ studied by high quality thin films. **Physica C: Superconductivity**. 185: 1343-1344.
- Scaife, D. J. (1980). Oxide semiconductors in photoelectrochemical conversion of solar energy. **Solar Energy**. 25(1): 41-54.
- Shannon, R. D. (1976). Revised effective ionic radii and systematic studies of interatomic distances in halides and chalcogenides. **Acta Crystallographica Section A**. 32(5): 751-767.
- Shannon, R. T., and Prewitt, C. T. (1969). Effective ionic radii in oxides and fluorides. **Acta Crystallographica Section B**. 25(5): 925-946.
- Siritanon, T., Laurita, G., Macaluso, R. T., Millican, J. N., Sleight, A. W., and

- Subramanian, M. (2009). First observation of electronic conductivity in mixed-valence tellurium oxides. **Chemistry of Materials**. 21(23): 5572-5574.
- Slobodin, B., Surat, L., Zubkov, V., Tyutyunnik, A., Berger, I., Kuznetsov, M., Perelyaeva, L., Shein, I., Ivanovskii, A., Shulgin, B., Solomonov, V., Svensson, G., Forslund, B., and Sayagués, M. (2005). Structural, luminescence, and electronic properties of the alkaline metal-strontium cyclotetranadates $M_2Sr(VO_3)_4$, (M= Na, K, Rb, Cs). **Physical Review B**. 72(15): 155205.
- Subramanian, M., Aravamudan, G., and Rao, G. S. (1983). Oxide pyrochlores-a review. **Progress in Solid State Chemistry**. 15(2): 55-143.
- Tan, G., Zhang, X., and Chen, Z. (2004). Colossal magnetoresistance effect of electron-doped manganese oxide thin film $La_{1-x}Te_xMnO_3$ (x= 0.1 and 0.15). **Journal of Applied Physics**. 95(11): 6322-6324.
- Thorogood, G. J., Kennedy, B. J., Peterson, V. K., Elcombe, M. M., Kearley, G. J., Hanna, J. V., and Luca, V. (2009). Anomalous lattice parameter increase in alkali earth aluminium substituted tungsten defect pyrochlores. **Journal of Solid State Chemistry**. 182(3): 457-464.
- Van den Berghe, S., Laval, J.-P., Gaudreau, B., Terryn, H., and Verwerft, M. (2000). XPS investigations on cesium uranates: mixed valency behaviour of uranium. **Journal of Nuclear Materials**. 277(1): 28-36.
- Waghmode, S. B., Vetrivel, R., Hegde, S. G., Gopinath, C. S., and Sivasanker, S. (2003). Physicochemical investigations of the basicity of the cation exchanged ETS-10 molecular sieves. **The Journal of Physical Chemistry B**. 107(33): 8517-8523.

Yang, Y., Su, X., Pan, S., Zhang, M., Wang, Y., Han, J., and Yang, Z. (2014). Crystal growth and calculation of the electronic band structure and density of states of $\text{Li}_3\text{Cs}_2\text{B}_5\text{O}_{10}$. **CrystEngComm**. 16(10): 1978-1984.



CHAPTER IV

ELECTRONIC BAND STRUCTURE AND CONDUCTION

MECHANISM OF $\text{CsMn}_x\text{Te}_{2-x}\text{O}_6$ MIXED VALENCE

CUBIC PYROCHLORES

4.1 Abstract

To study the effects of M cations on structure and electronic properties of $\text{Cs}(\text{M},\text{Te})_2\text{O}_6$ mixed valence compounds, series of oxides with the general formula $\text{CsMn}_x\text{Te}_{2-x}\text{O}_6$ have been prepared by solid state method. The substitution of Te in CsTe_2O_6 with 2.5% Mn ($x = 0.05$) changes the structure from rhombohedral to cubic phase. Based on the XPS and XANES, it indicates that there are two substitution schemes depending on the x values. When x is lower than 0.33, Mn^{3+} replaces Te^{4+} . On the other hand, for samples with $x > 0.33$, Te^{6+} are replaced by a mixture of Mn^{3+} and Mn^{4+} . The switching between these two schemes occurs at around $x = 0.30-0.33$ which results in a change in the trend of the cell parameter and electronic conductivity. To explain the electronic properties, simple schematic band structure diagrams of the samples were proposed based on experimental results and DFT calculations. Although the number of Te^{4+} in $\text{CsMn}_x\text{Te}_{2-x}\text{O}_6$ ($x < 0.33$) is higher but its energy level is lower comparing to n -type $\text{Cs}(\text{Al},\text{Te})_2\text{O}_6$ with Te 5s donor states. In these samples, Te 5s states overlap with Mn 3d and O 2p states at the top of the valence band instead of behaving like a donor level near the conduction band.

However, it was founded that the unit cell parameters correlation with the energy levels of Te 5s states. When the cell parameter is small, Te^{4+} is destabilized in the lattice causing its energy level and conductivity of the sample to increase. Although samples with $x > 0.33$ contain oxygen vacancies and $\text{Mn}^{3+}/\text{Mn}^{4+}$ mixed valency, they do not show any improvement in the conductivity. Thus, the $\text{CsMn}_x\text{Te}_{2-x}\text{O}_6$ compounds exhibit intrinsic semiconducting behavior and have much lower conductivity.

4.2 Introduction

The development of new materials for modern electronic devices becomes typical issues for sustainable development of human society. The many applications of materials, such as thermoelectric, solar cell, and transparent conductors, etc., gain attention in both science and engineering research fields. These applications are strongly related to the electrical properties (Mikami et al., 2005; Wenas et al., 1991; H. Zhang et al., 2015). Among all solid-state materials, oxides containing post-transition elements have attracted great attention. Particularly, the *n*-type doping in post-transition metal oxides such as In_2O_3 , SnO_2 , ZnSnO_3 , and BaBiO_3 (Alsac et al., 2013; Cai et al., 2016; Chen et al., 2013; Sato et al., 1991) which show high conductivity due to the presence of diffused *s* orbitals which results in wide conduction bands and low carrier mobility (Kawazoe et al., 2000). However, the lists of such examples are scarce for Sb and Te oxides despite being in the same row and the electron conduction of tellurium oxides are very rare. One important example for tellurium containing oxides with relatively high conductivity is $\text{Cs}(\text{M},\text{Te})_2\text{O}_6$ series reported in 2009 (Siritanon et al., 2009). It has been concluded that the conductivity

stems from $\text{Te}^{4+}/\text{Te}^{6+}$ mixed valency in the compounds (Li et al., 2011). Small amount of Te^{4+} in the lattice caused by a slight deviation from stoichiometry generates donor states close to the conduction band leading to the *n*-type character.

One crucial structural factor that allows the high conductivity is the cubic symmetry of the unit cell where both Te^{4+} and Te^{6+} occupy the same crystallographic site leading to a class II mixed valency according to Robin and Day's classification (Robin and Day, 1968). In fact, it was postulated that the hypothetical cubic CsTe_2O_6 itself could be metallic (Siritanon et al., 2009). However, the actual rhombohedral CsTe_2O_6 contains long $\text{Te}^{4+}\text{-O}$ and shorter $\text{Te}^{6+}\text{-O}$. The longer $\text{Te}^{4+}\text{-O}$ bond means that Te^{4+} states are stabilized and their energy level is too low. The conductivity of CsTe_2O_6 is therefore very low (cannot be measured at room temperature). The substitution of small M cation at Te site not only changes the rhombohedral CsTe_2O_6 to cubic $\text{Cs}(\text{M},\text{Te})_2\text{O}_6$ but also determines the cell parameter and hence Te-O bond distance. It is generalized that the smaller unit cell, e.g. the shorter Te-O bond, destabilizes Te^{4+} donor level moving it closer to the conduction band edge and results in higher conductivity. Among all compounds in the series, only $\text{Cs}(\text{Al},\text{Te})_2\text{O}_6$ has been extensively studied (J. Li et al., 2011). While the small Al^{3+} causes donor states in $\text{CsAl}_{0.33}\text{Te}_{1.67}\text{O}_6$ to have high energy level, the number of such states are very low. To the best of our knowledge, the only $\text{Cs}(\text{M},\text{Te})_2\text{O}_6$ related compounds that form cubic structure with high content of Te^{4+} is $\text{Cs}(\text{W},\text{Te})_2\text{O}_6$. However, the compounds show no measurable electronic conductivity (Siritanon et al., 2011).

In this work, we will study the electrical properties of Mn doped CsTe_2O_6 with different concentrations of manganese. To understand the structure-property relationships of mixed valence tellurium containing oxides, we studied the electronic

structure using both X-ray absorption and X-ray photoelectron spectroscopy (Hishida et al., 2013; Zhang et al., 2015; H. Zhang et al., 2015). It is the purpose of this work to explore $\text{Cs}(\text{M},\text{Te})_2\text{O}_6$ related compounds with $\text{M} = \text{Mn}$. Mn is chosen because our preliminary results indicated that the cubic pyrochlore structure can be achieved with various Mn content. Therefore, $\text{Cs}(\text{Mn},\text{Te})_2\text{O}_6$ would be the second series of compounds with cubic structure and higher Te^{4+} content. This work supplies a theoretical and experimental knowledge for the doping approach in order to have control over the electronic properties of new tellurium oxide materials.

4.3 Experiments

4.3.1 Preparation of $\text{CsMn}_x\text{Te}_{2-x}\text{O}_6$

The solid-state reaction method was used to prepare $\text{CsMn}_x\text{Te}_{2-x}\text{O}_6$ series. Stoichiometric amounts of CsNO_3 (Sigma-Aldrich, 99+%), Mn_2O_3 (Sigma-Aldrich, 99%), and TeO_2 (Acros Organic, 99+%) were ground in an agate mortar and heated at 550°C for 5 h. After that, the samples were reground and sintered at 625°C for 24 h in air.

4.3.2 Characterizations

Powder X-ray diffraction patterns were recorded by a Bruker D2 Phaser diffractometer (Cu $K\alpha$ radiation, $\lambda = 1.5406 \text{ \AA}$) for phase identification. X-ray absorption near edge structure (XANES) and X-ray photoelectron spectroscopy (XPS) experiments were carried out at Synchrotron Light Research Institute, Thailand. The Te L_3 -edge spectrum was obtained at the BL5.2: SUT-NANOTEC-SLRI XAS Beamline using transmission modes. The Mn $L_{3,2}$ -edge and O K-edge spectra were

obtained at the BL3.2Ua: PES (Photoelectron Emission Spectroscopy) using total electron yield modes (TEY). The XPS of Mn $2p$, Te $3d$ and valence band (VB) were recorded by a PHI5000 VersaProbe II XPS Instruments (ULVAC-PHI, Japan) (Monochromatic X-ray of Al $K\alpha$, 1486.6 eV) at BL5.3: SUT-NANOTEC-SLRI. The C $1s$ at 284.8 eV was used as a reference for the binding energies drift due to charging effects. The electrical conductivities of all sintered samples were measured from 298 to 673 K by a four-probe method using a Keysight B2901A source/measure unit.

4.4 Calculations

To further explore the electronic structures of the $\text{CsMn}_x\text{Te}_{2-x}\text{O}_6$ cubic pyrochlores, the projected density of states (PDOS) of the $\text{CsMn}_{0.25}\text{Te}_{1.75}\text{O}_6$ system was calculated. The model was taken from the Rietveld-refined experimental unit cell of CsTe_2O_6 containing 8 Cs cations, 16 Te cations, and 48 O anions which corresponds to eight CsTe_2O_6 formula unit ($\text{Cs}_8\text{Te}_{16}\text{O}_{48}$) (Siritanon et al., 2011). Then, the $\text{CsMn}_{0.25}\text{Te}_{1.75}\text{O}_6$ model system was achieved by replacing two Te ions with two Mn ions. The foreign Mn ions are expected to statistically distribute at the Te sites which yield nonequivalent lattice configurations with different total energies. While the other lower energy configurations may exist, it is expected that the overall electronic structures are not affected by the positions of the two Mn ions.

The calculated electronic structures reported herein were carried out using spin-polarized density functional theory (DFT+U) with periodic model as implemented in Vienna Ab Initio Simulation Package (VASP 5.3) (Kresse and Furthmüller, 1996; G. Kresse and Hafner, 1993). Dudarev's approach (Kresse and Hafner, 1993) was used for DFT+U calculations to correct for the self-interaction

error inherent in current exchange-correlation functionals DFT when applied to transition metals with tightly localized *d* electrons, such as Mn in the $\text{CsMn}_{0.25}\text{Te}_{1.75}\text{O}_6$ model system. It is known that the proper value of *U* parameter varies from systems to systems and also depends on the interested properties of the system. There have been several studies reported the use of *U* value in the range of 4.0 to 5.5 eV for studying various properties of bulk and surfaces of MnO_2 (Dudarev et al., 1998; L. Li et al., 2015; Sun et al., 2011; Tompsett et al., 2012; Tompsett et al., 2013). In this work, the *U* value of 4.0 eV was chosen for Mn *3d* electrons as it was used to properly describe the electronic structures of stoichiometric and reduced MnO_2 systems (Sun et al., 2011). Exchange correlation is described within the generalized gradient approximation with the Perdew-Burke-Ernzerhof functional (Perdew et al., 1996). The ultrasoft pseudopotential with the projector augmented wave method was chosen to represent the inner core potentials and treated the Cs *5s5p6s*, Te *5s5p*, Mn *3s3p3d4s*, and O *2s2p* as valence electrons (Blöchl, 1994; Kresse and Joubert, 1999). Their wave functions were expanded in the plane-wave basis with a cutoff energy of 400 eV. The tetrahedron smearing method with Bloch corrections with a gamma-centered *k*-point of $3 \times 3 \times 3$ were used to produce the PDOS. Using a denser $5 \times 5 \times 5$ *k*-mesh yields a negligible difference of the PDOS results.

4.5 Results and discussion

4.5.1 Crystal Structure

Figure 4.1 shows the powder X-ray diffraction patterns of all prepared $\text{CsMn}_x\text{Te}_{2-x}\text{O}_6$ samples which indicate that all diffraction peaks can be indexed as AB_2O_6 cubic defect pyrochlore with $\text{Fd}\bar{3}m$ space group. Not that the single phase

compound was achieved for composition with $x = 0.05 - 0.43$. Lower or higher Mn content resulted in impurities. In this defect pyrochlore lattice, hexagonal tunnels are created by corner-sharing network of (Mn/Te) O_6 octahedra. The Cs cations occupy the position in these tunnels (Subramanian et al., 1983). However, it is interesting that only 2.5% of Mn is enough to disrupt the ordering of Te^{4+} and Te^{6+} in rhombohedral $CsTe_2O_6$. As reported earlier, substituting Te with W could also alter the symmetry of the structure but at least 10% W content was required (Siritanon et al., 2011). The shift of the diffraction peaks suggest that Mn is incorporated into the lattice. In addition, the lattice parameters were carefully calculated by Le Bail refinement with the use of NaCl internal standard. As illustrated in Figure 4.2, the relationship between cell parameters and Mn content form two linear lines with a different slope. This observation suggests that there are two different mechanisms of the Mn substitution with the switching point around $x = 0.33-0.37$.

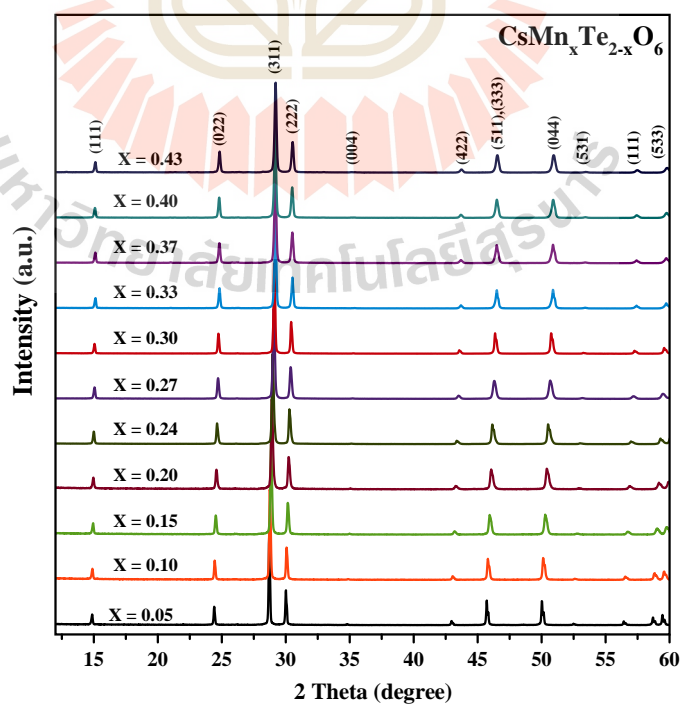


Figure 4.1 Powder X-ray diffraction patterns of $CsMn_xTe_{2-x}O_6$.

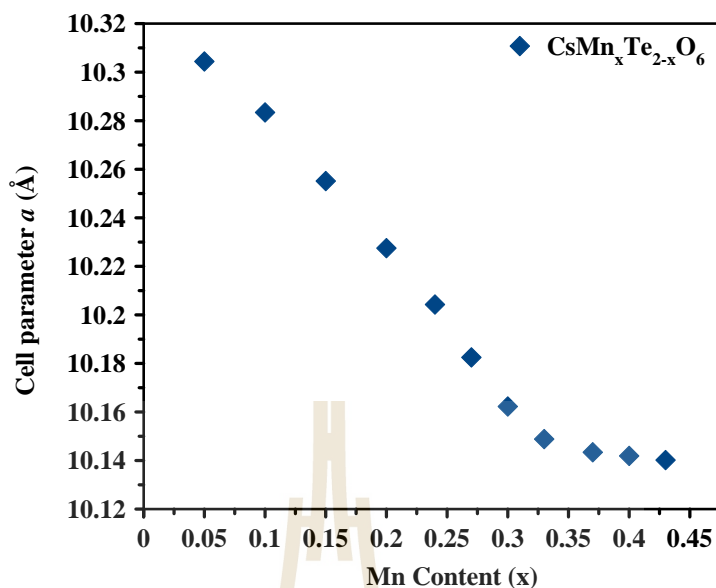


Figure 4.2 Changes of cell parameters with Mn content.

4.5.2 X-ray absorption near edge structure (XANES) results

As Mn with more than one oxidation states can occur in oxides. The oxidation states of Mn in the samples and substitution mechanisms were investigated by XANES. Figure 4.3 show the Mn $L_{3,2}$ -edge XANES spectra of the samples. The spectra correspond to Mn $2p \rightarrow 3d$ allowed transition and are split into Mn L_3 ($2p_{3/2}$) and Mn L_2 ($2p_{1/2}$) because of the spin-orbit coupling (Garvie and Craven, 1994; Sultan et al., 2015). Each peak is further split into t_{2g} (denoted A and C in Figure 4.3) and e_g state (denoted B and D in Figure 4.3) due to crystal field effect. These complex spectra feature gives valuable information on Mn in the samples. First of all, the energy position of Mn L_3 -edge peak of all samples align well with that of Mn^{3+} indicating that Mn^{3+} is a major component (Arun et al., 2018). The small shoulder is observed in Mn L_3 -edge spectrum of the sample with $x > 0.33$ which indicates the presence of Mn^{4+} (Arun et al., 2018; Thakur et al., 2008). Furthermore, the intensities

of the split peaks reflect the total unoccupy of Mn 3d states which can additionally imply the valence situation of Mn (Asokan et al., 2009; Shukla et al., 2008; Thakur et al., 2008). The ratio of unoccupied e_g states to unoccupied t_{2g} states is higher in Mn^{4+} than in Mn^{3+} (Asokan et al., 2009; Garvie and Craven, 1994). Thus, the increases of B/A and D/C ratio indicate the increase of Mn^{4+} content. In this case, the Mn L_2 -edge regions clearly shows splitting into two features which can be identified to t_{2g} and e_g state. It is clear that the intensity of e_g region is higher than t_{2g} in sample with $x > 0.33$ which reflects the increase in the e_g unoccupied state and the positive charge of Mn ion. Thus, based on the area and position of Mn L -edge peak, it is clear that sample with $x > 0.33$ contain $\text{Mn}^{3+}/\text{Mn}^{4+}$ mixed valency. It is interesting to note that this mixed valency appears at the same switching point observed in XRD patterns (Figure 4.2).

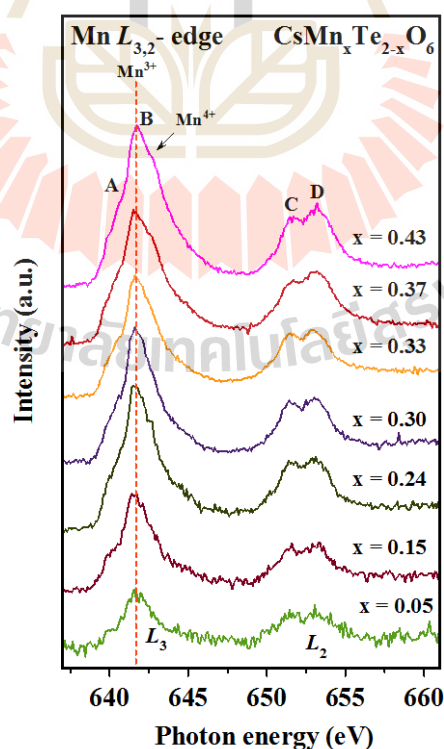


Figure 4.3 Mn $L_{3,2}$ -edge XANES spectra of $\text{CsMn}_x\text{Te}_{2-x}\text{O}_6$.

The Te L_3 -edge XANES spectra were collected to study Te oxidation states (Figure 4.4(a)). With the use of a calibration curve constructed from edge energies of TeO_2 (Te^{4+}), CsTe_2O_6 (mixed $\text{Te}^{4+}/\text{Te}^{6+}$) and KTaTeO_6 (Te^{6+}) (Figure 4.4(b)), the $\text{Te}^{4+}/\text{Te}^{6+}$ ratio in the samples were estimated as summarized in Table 4.1. It is obvious that for samples with $x = 0.05 - 0.33$, Te^{4+} is replaced by Mn^{3+} leading to the decrease of Te^{4+} content while Te^{6+} content increase. One could represent the substitution situation for these samples with the general formula $\text{Cs}^{1+}(\text{Mn}^{3+})_x(\text{Te}^{4+})_{0.5-(3x/2)}(\text{Te}^{6+})_{1.5+(x/2)}\text{O}_6$. Although the ionic radius of Mn^{3+} (0.645 Å) is much smaller than that of Te^{4+} (0.97 Å) and larger than that of Te^{6+} (0.56 Å) (Shannon, 1976; Shannon and Prewitt, 1969), this formula is in agreement with the significant reduction in unit cell parameters of the samples with $x \leq 0.33$.

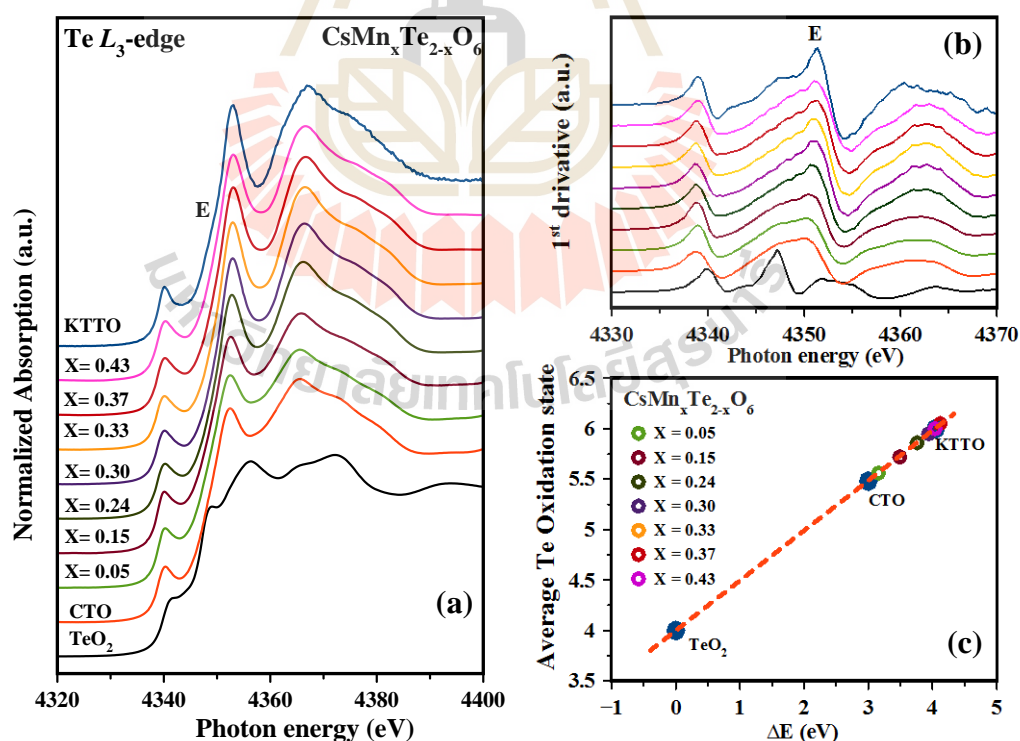


Figure 4.4 Te L_3 -edge XANES (a), 1st derivative spectra (b) and a calibration curve used to estimate average oxidation state (c) of Te in $\text{CsMn}_x\text{Te}_{2-x}\text{O}_6$.

The obtained results as summarized in Table 1 suggest that Te^{6+} was replaced by Mn in the samples with $x > 0.33$. As results from Mn $L_{3,2}$ -edge XANES suggest that these samples contain $\text{Mn}^{3+}/\text{Mn}^{4+}$ mixed valency, they must have a different mechanism for charge compensation. The most probable mechanism here is the formation of oxygen vacancies. Thus, the charge compensation mechanism of compounds with $x = 0.37-0.43$ may be represented with the general formula $\text{Cs}^{1+}(\text{Mn}^{3+/4+})_x(\text{Te}^{6+})_{2-x}\text{O}_{6-\delta}$. This would also lead to a less significant change in the cell parameters as observed in Figure 4.2. It was previously reported that the AB_2O_6 defect cubic pyrochlore structure including CsTe_2O_6 , can accumulate some oxygen vacancies (Groult et al., 1982; Siritanon et al., 2011). Note that the $\text{Te}^{4+}/\text{Te}^{6+}$ contents calculated from this proposed formula agree well with the numbers estimated from the calibration curve (Table 4.1).

Table 4.1 Estimated Te^{4+} and Te^{6+} content in $\text{CsMn}_x\text{Te}_{2-x}\text{O}_6$ samples.

Mn content	ΔE (eV)	Valence	Te Content		Ideal Te Content*	
			Te^{6+}	Te^{4+}	Te^{6+}	Te^{4+}
0.00 (CTO)	3.00	5.48	1.48	0.52	1.50	0.50
0.05	3.16	5.56	1.52	0.43	1.52	0.43
0.15	3.49	5.72	1.59	0.26	1.57	0.28
0.24	3.76	5.86	1.63	0.13	1.62	0.14
0.30	3.94	5.95	1.65	0.05	1.65	0.05
0.33	4.12	6.05	1.70	-0.03	1.67	0.00
0.37	4.12	6.05	1.66	-0.03	1.63	0.00
0.43	4.04	6.00	1.57	0.00	1.57	0.00

*calculated from $\text{Cs}^{1+}(\text{Mn}^{3+})_x(\text{Te}^{4+})_{0.5-(3x/2)}(\text{Te}^{6+})_{1.5+(x/2)}\text{O}_6$ for $x = 0.05-0.33$ and from $\text{Cs}^{1+}(\text{Mn}^{3+/4+})_x(\text{Te}^{6+})_{2-x}\text{O}_{6-\delta}$ for $x > 0.33$.

4.5.3 X-ray photoelectron spectroscopy (XPS) results

XPS was used to further study the elemental composition and oxidation states of elements (Figure 4.5). The Mn $2p$ and Te $3d$ XPS were recorded to support XANES results, which indicate that the same conclusion (see Figure B1-B2 and Table B1). Cs $3d$ and O $1s$ XPS spectra are shown in Figure 4.6. The obtained Cs $3d$ binding energies at ~ 723.5 eV are characteristics of Cs^+ and are similar to previous reports (Marschall et al., 2011; Van den Berghe et al., 2000). The shoulder at slightly higher binding energy (~ 724.8 eV) is observed in Cs $3d$ spectra of the sample with $x > 0.33$ but its energy is still within a range of Cs^+ (723.5-725.1 eV) (Van den Berghe et al., 2000; Wahoud et al., 2014). Thus, these shoulders may suggest a presence of Cs^+ in different environments, such as Cs^+ in the vicinity of the oxygen vacancies or hydroxyl (Podgornov et al., 2000). O $1s$ spectra could be deconvoluted into three parts which correspond to lattice oxygen (O_L), oxygen vacancies (V_o), and adsorbed oxygen (O_A) respectively (Dudric et al., 2014; Rahimnejad et al., 2014; Wang et al., 2017). The higher V_o content is obtained in samples with $x > 0.33$ suggesting the presence of more oxygen vacancies which is consistent with the proposed formula. As change in unit cell parameter and previously discussed XANES data suggest the change of substitution mechanism which could be a reason behind this.

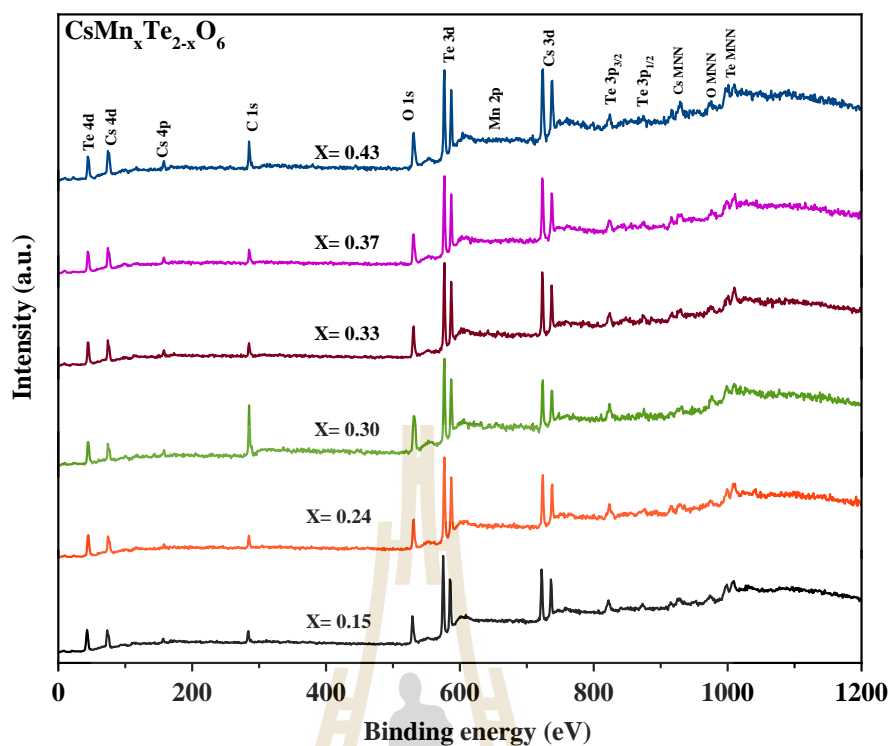


Figure 4.5 XPS survey spectra of $\text{CsMn}_x\text{Te}_{2-x}\text{O}_6$.

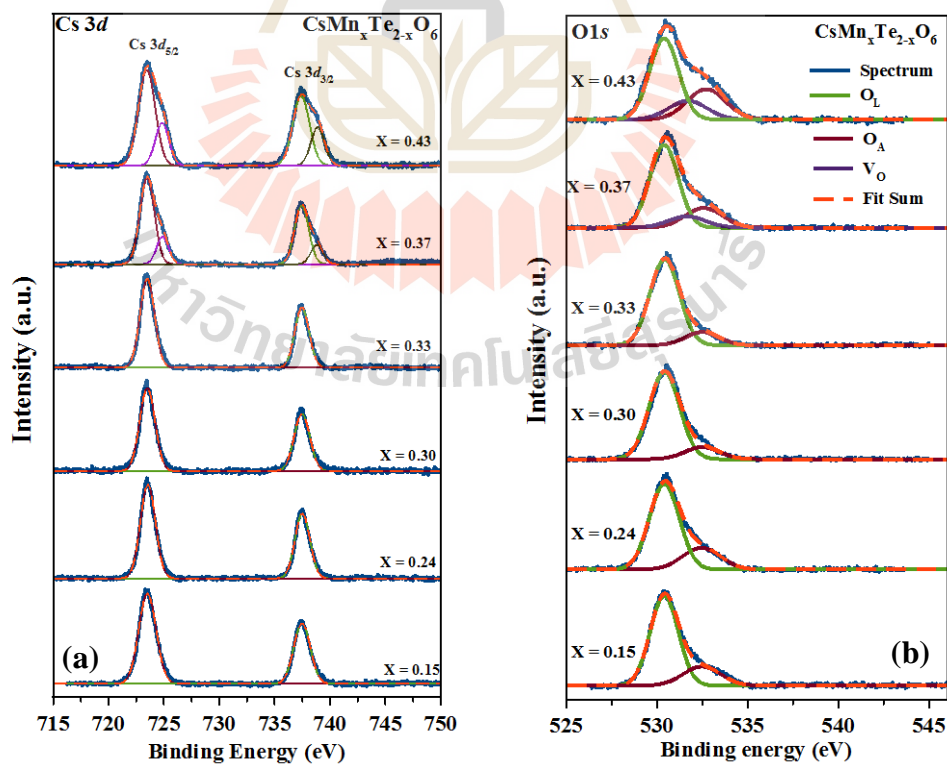


Figure 4.6 Cs 3d (a) O 1s (b) XPS spectra of $\text{CsMn}_x\text{Te}_{2-x}\text{O}_6$.

4.5.4 Electrical properties

Electronic conductivities of the samples were measured from 298 to 673 K and plotted according to the Arrhenius equation: $\sigma = Ae^{(-E_a/kT)}$ where A is pre-exponential constant, k is Boltzmann constant, E_a is activation energy, and T is absolute temperature as shown in Figure 4.7(a). The obtained activation energies of conduction are also plotted with Mn content as shown in Figure 4.7(b). The lowest activation energy of all samples in the series is $\text{CsMn}_{0.3}\text{Te}_{1.7}\text{O}_6$. The conductivities and activation energies clearly depend on the cell parameters. The smaller the unit cell parameters, the higher the conductivities. The same trend is previously reported in Siritanon et al., 2009. As reported by Siritanon et al (Siritanon et al., 2009), the type of M cations in $\text{Cs}(\text{M},\text{Te})_2\text{O}_6$ affects the conductivity of the compounds as some M cations can provide orbitals with appropriate energy to overlap with Te 5s at conduction band which increases the conductivity. The conductivity of $\text{CsMn}_{0.3}\text{Te}_{1.7}\text{O}_6$ is lower than that of previously reported $\text{CsGa}_{0.33}\text{Te}_{1.67}\text{O}_6$ despite having similar cell parameters because Mn 3d orbital is not as diffused as the s orbital of Ga. It is interesting to note that the Mn series in this work generally have smaller cell parameters than the W series (Siritanon et al., 2011). As a result, Mn series exhibit higher conductivities. Although oxygen vacancies can often improve electronic conductivity of oxides, it is not the case for this group of tellurium oxide pyrochlores. The $\text{CsTe}_2\text{O}_{6-x}$ series were not conducting (Siritanon et al., 2011) and $\text{CsMn}_x\text{Te}_{2-x}\text{O}_6$ samples with $x > 0.33$ do not show any improvement in the conductivities. In addition, $\text{CsMn}_x\text{Te}_{2-x}\text{O}_6$ have black color which indicates a more similar environment between Te^{4+} and Te^{6+} . The color reflects the intervalence charge transfer from $\text{Te}^{4+} 5s^2$ to $\text{Te}^{6+} 5s^0$ and $d-d$ transition of Mn (Kim et al., 2017).

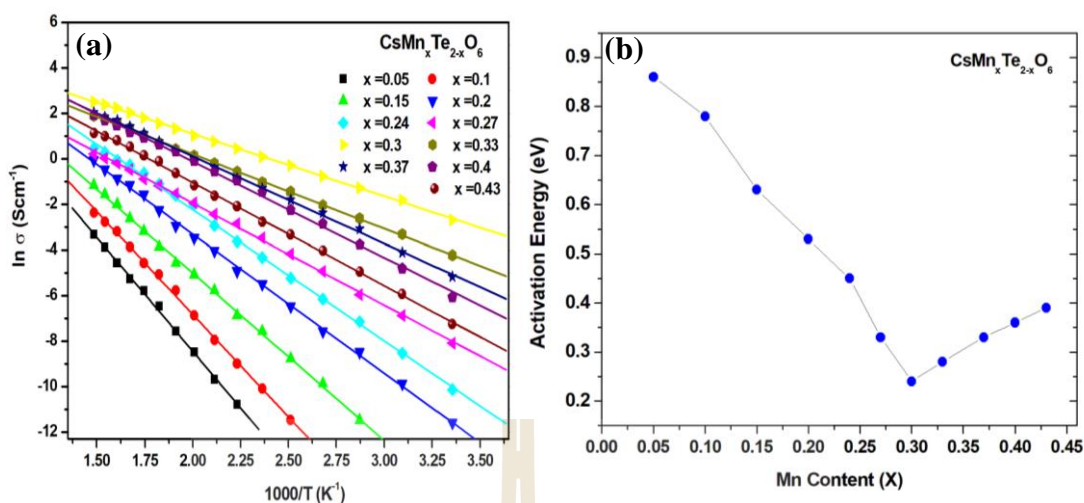


Figure 4.7 Arrhenius plots of electronic conductivities (a) and the obtained activation energy of conduction (b).

4.5.5 Electronic structure

The obtained XPS at valence band region (Figure 4.8), O K -edge XANES (Figure 4.9) and theoretical calculation (Figure 4.10) were used to study the electronic structure of $\text{CsMn}_x\text{Te}_{2-x}\text{O}_6$ cubic pyrochlore. XPS spectra at valence band region give useful information about the electronic band structure at occupied state of all samples. The valence band feature of all samples can be roughly separated into three regions. The bottom of valence band (denoted A in Figure 4.8(a) and Figure 4.10(c)) is mainly of Cs $5p$ state with small contribution from Te $5p$ and O $2p$ which is similar to the previous report (Van den Berghe et al., 2000; Waehayee et al., 2017). Hybridization between O $2p$, the Mn $3d$, and Te $5p$ results in the peak denoted B. The position of this peak slightly shifts toward higher energy when Mn content is increased. There are two factors that might affect B position, the degree of overlapping and the energy level of Mn $3d$, both of which are correlated with the unit

cell parameters and the environments around Te/Mn including Te/Mn-O distance and Te/Mn-O-Te/Mn angle. Furthermore, the presence of Mn^{4+} in samples with $x > 0.33$ also affected B position because the $3d$ of Mn^{4+} contribute to the top of the valence band as reported in (Fu et al., 2018; Hishida et al., 2013). A small shoulder (denoted C in Figure 4.8(a) and Figure 4.10) is most likely a result of Mn $3d$ and Te $5s$ states from Te^{4+} present in the samples. Therefore, the change in the intensity of peak C is related to the changes in Te^{4+} and Mn content of each sample. In addition, samples with $x = 0.37$ and 0.43 exhibit small tailing around C which might be caused by the oxygen vacancies (Lv et al., 2016).

O K -edge XANES spectra is the absorption edge of $1s$ to $2p$ transition in oxygen atom and relate to the conduction band of oxides (Balasubramanian et al., 2013; Pellegrin et al., 1997). Figure 4.9(a) displays O K -edge XANES of $\text{CsMn}_x\text{Te}_{2-x}\text{O}_6$ samples. The bottom of the conduction band, A^* , is identified to consist of Te $5s$ states with some contribution from Mn states (Figure 4.9(a) and Figure 4.10). This feature clearly becomes more intense with Mn content. Thus, it is most likely contributed by hybridization of Mn $3d$ and O $2p$ (Abbate et al., 1997; Balasubramanian et al., 2013; Pellegrin et al., 1997). The feature B^* corresponds to hybridization of Te $5s$ -O $2p$. The split-off conduction band is separated from a broad higher conduction band contributed by Mn $3d$ and Te $5p$ states which denoted C^* and D^* respectively. The strong contribution from Mn $3d$ is reflected by the slight increase in intensity of the peak in this region when Mn content increases. These peaks position agree well with the calculated DOS results. Furthermore, the first derivative plot (Figure 4.9(b)) shows a shift of conduction band minimum when Mn content changes.

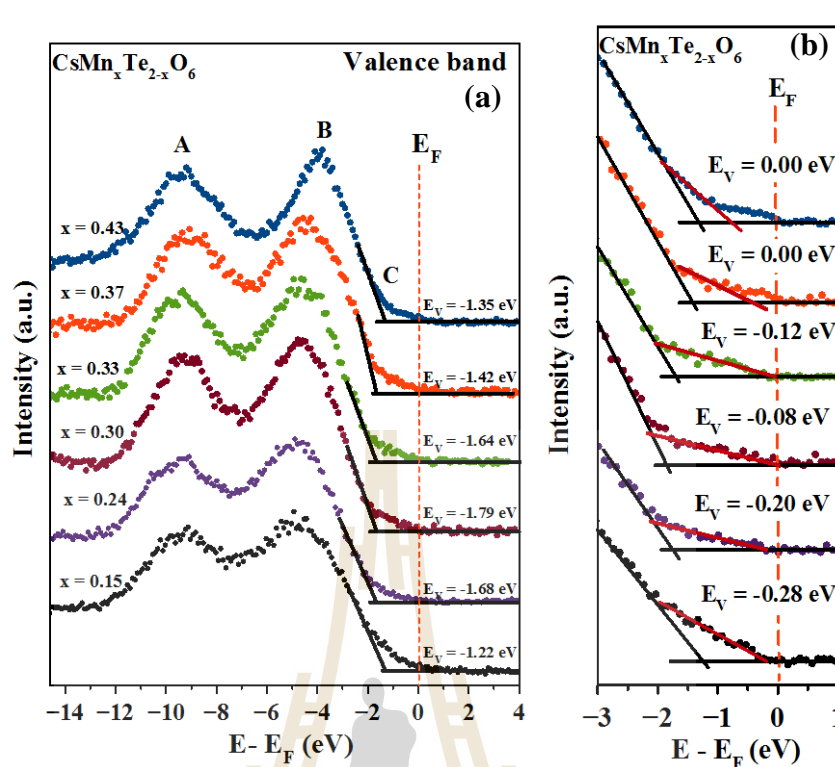


Figure 4.8 Valence band XPS (a) and XPS close-up near E_F (b) of $\text{CsMn}_x\text{Te}_{2-x}\text{O}_6$.

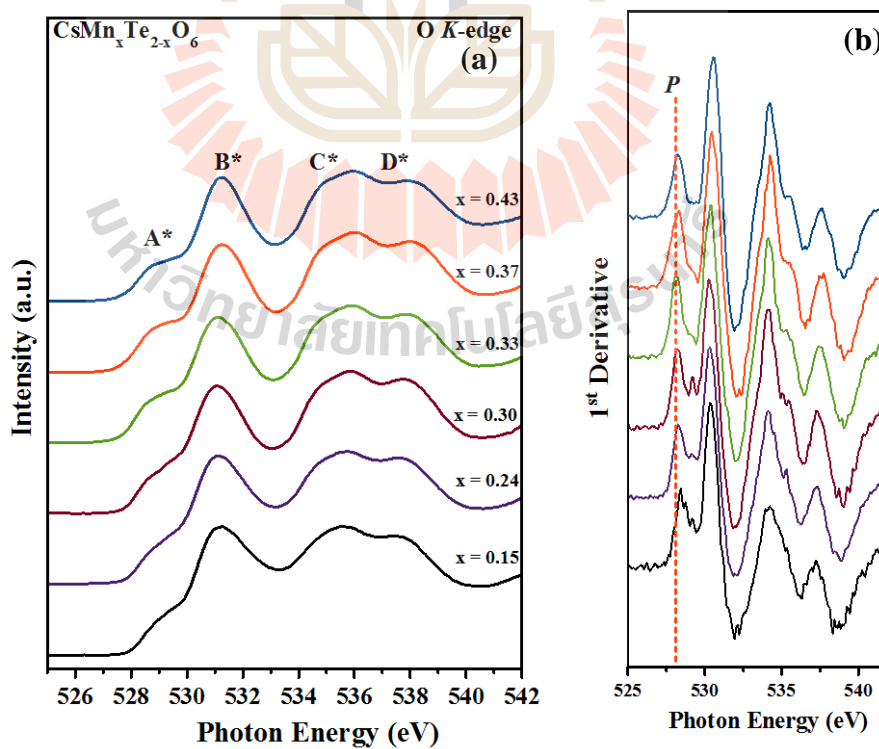


Figure 4.9 O K-edge spectra (a) and first derivatives (b) of $\text{CsMn}_x\text{Te}_{2-x}\text{O}_6$.

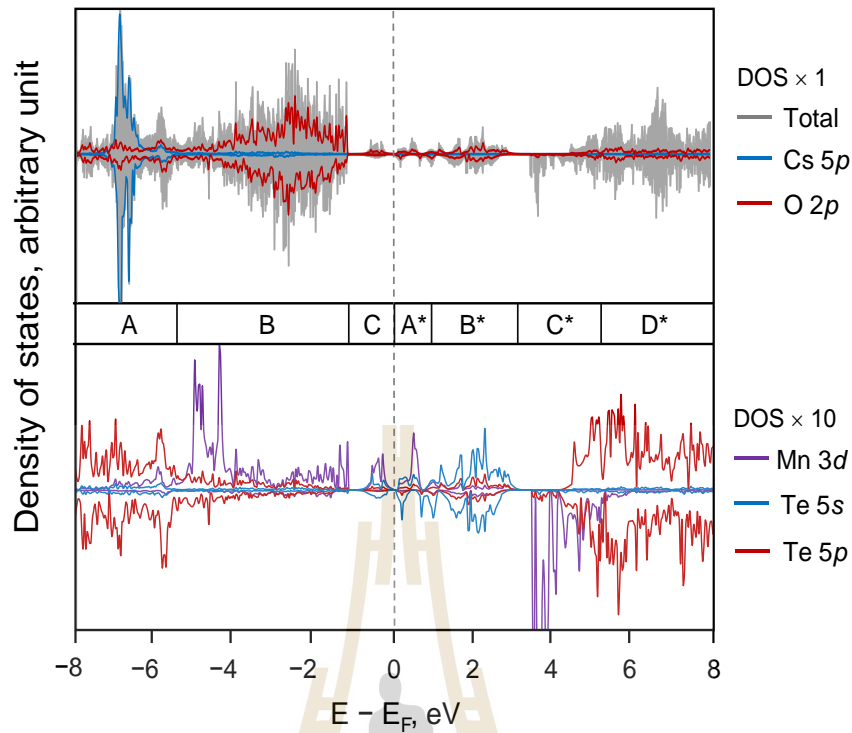


Figure 4.10 Calculated PDOS of the $\text{CsMn}_{0.25}\text{Te}_{1.75}\text{O}_6$ system. The energy of the PDOS are plotted with relative to the Fermi energy.

In addition, the calculated magnetization of $8 \mu\text{B}$ indicates that there are in total 8 unpaired electrons in the system implying a formation of two Mn^{3+} ions ($[\text{Ar}]3d^4$). Our calculated results are consistent with those of experimental observations that at lower range of Mn concentrations ($x < 0.33$ in $\text{CsMn}_x\text{Te}_{2-x}\text{O}_6$) the oxidation state of Mn is 3+. The calculated band gap of 0.2 eV is also consistent with the activation energies obtained from Arrhenius analysis for $x = 0.24, 0.30$; $E_a = 0.45$ and 0.24, respectively ((Figure 4.7(a))

4.4.6 Band structure

To explain the electronic properties of the samples, the simple schematic band structures of the compounds comparing to previous work (CsTe_2O_6

and $\text{CsAl}_{0.33}\text{Te}_{1.67}\text{O}_6$) were proposed based on the XPS at valence band region, O *K*-edge XANES and activation energy (Figure 4.11). As concluded in chapter III, CsTe_2O_6 is an intrinsic semiconductor while $\text{CsAl}_{0.33}\text{Te}_{1.67}\text{O}_6$ is an *n*-type semiconductor. The electronic conductivity of CsTe_2O_6 relates the activation of electrons from the valence band ($\text{Te}^{4+} 5s$) to the conduction band. On the other hand, $\text{CsAl}_{0.33}\text{Te}_{1.67}\text{O}_6$ is more conducting because of the low activation energy required to activate electrons in donor levels ($\text{Te}^{4+} 5s$). However, the band structures, especially the energy difference between the top of the valence band and the bottom of the conduction band ($E_c - E_v$) indicates that all samples in $\text{CsMn}_x\text{Te}_{2-x}\text{O}_6$ series are an intrinsic semiconductor.

In $\text{CsMn}_x\text{Te}_{2-x}\text{O}_6$ ($x < 0.33$), Te *5s* states have low energy that they overlap with Mn *3d* state and become part of the valence band. This situation is similar to that observed in CsTe_2O_6 although the hybridized states in $\text{CsMn}_x\text{Te}_{2-x}\text{O}_6$ have slightly higher energy because of the different structure. On the other hand, Te *5s* state in $\text{CsAl}_{0.33}\text{Te}_{1.67}\text{O}_6$ is considered a donor state whose energy is close to the conduction band minimum because Te^{4+} in octahedra is compressed by a smaller cell dimension. It should be noted that there are much more Te^{4+} in $\text{CsMn}_x\text{Te}_{2-x}\text{O}_6$ ($x < 0.33$) than in $\text{CsAl}_{0.33}\text{Te}_{1.67}\text{O}_6$. It is interesting that if the energy of Te *5s* band in $\text{CsMn}_x\text{Te}_{2-x}\text{O}_6$ move up to overlap with the conduction band, the materials will show a metallic-like property. Unfortunately, the number of Te^{4+} is correlated with the unit cell dimension and higher Te^{4+} content expands the unit cell, hence lowers its energy level. The correlation between cell parameters and activation energy of conduction is quite significant as a simple plot shown in Figure 4.12 is roughly linear. Note that this correlation is obvious because both parameters are from the same series of

compounds with similar electronic structure. However, when compare with other $\text{Cs}(\text{M},\text{Te})_2\text{O}_6$, other factors such as the energy level and diffusivity of M orbitals could result in some deviations.

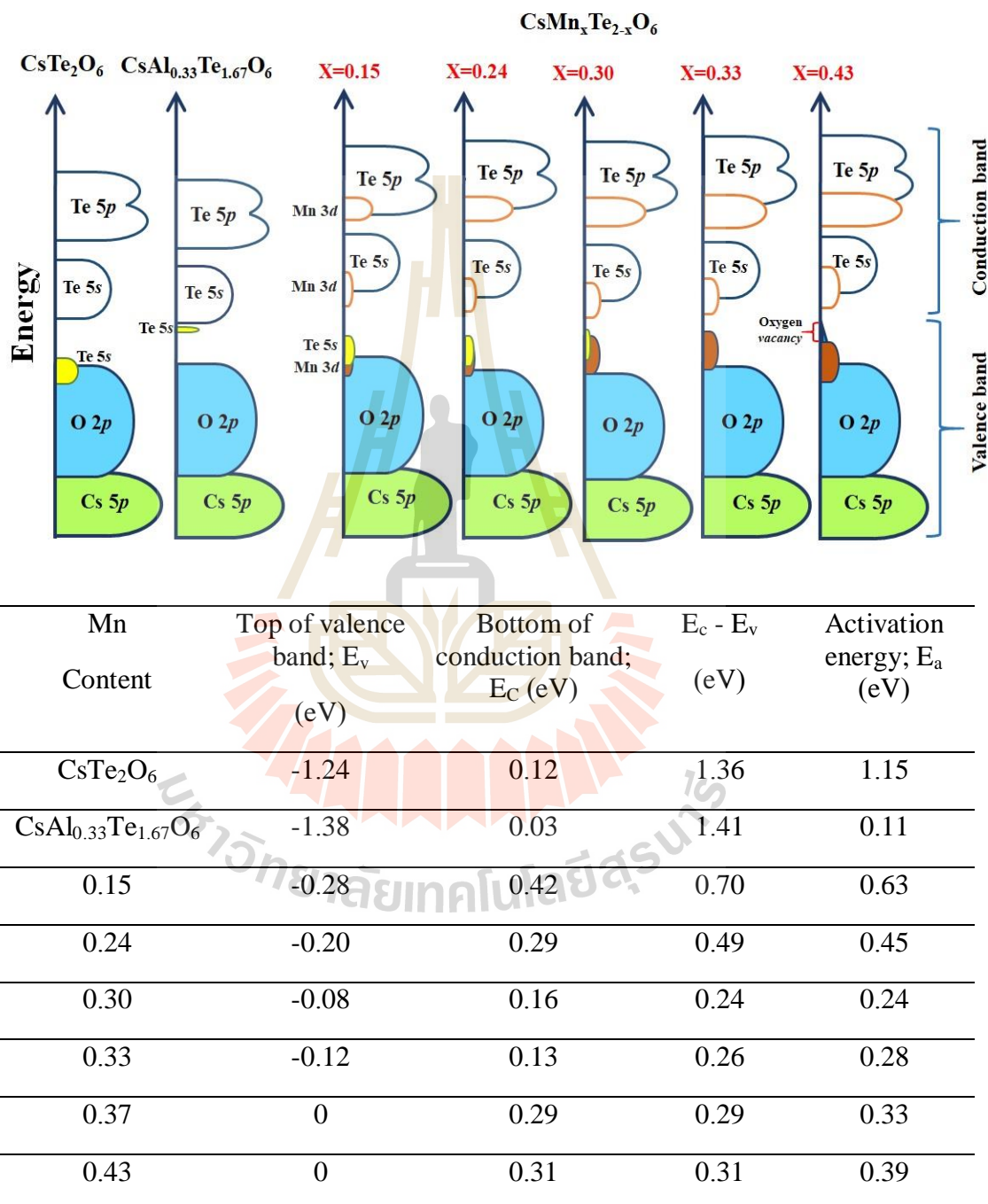


Figure 4.11 The proposed schematic band structures of $\text{CsMn}_x\text{Te}_{2-x}\text{O}_6$ compared to CsTe_2O_6 and $\text{CsAl}_{0.33}\text{Te}_{1.67}\text{O}_6$.

Because of the disappearance of Te^{4+} in $\text{CsMn}_{0.33}\text{Te}_{1.67}\text{O}_6$, its electronic behavior depends on the energy differences between the energy level of Mn $3d$ state and the conduction band minimum. Thus, the switching in the trend of electrical conductivity of these two schemes occurs at around $x = 0.30$ - 0.33 . Although occurrence oxygen vacancies in samples with $x > 0.33$ can raise valence band maximum, it does not increase the electrical conductivity because the conduction band minimum is also lifted.

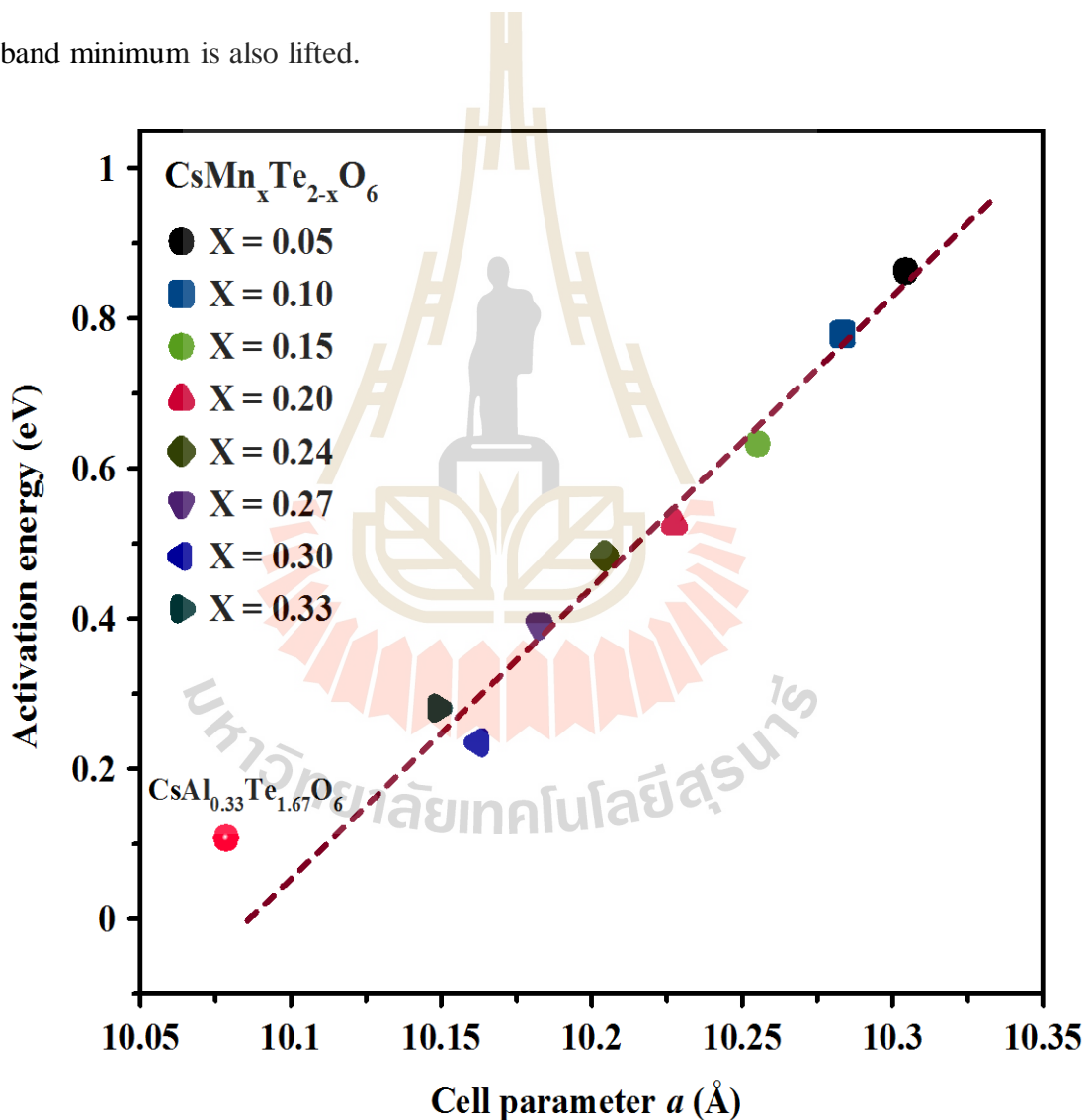


Figure 4.12 Plots of cell parameters versus activation energy of $\text{CsAl}_{0.33}\text{Te}_{1.67}\text{O}_6$ and $\text{CsMn}_x\text{Te}_{2-x}\text{O}_6$ ($x=0.05$ - 0.33).

4.6 Conclusion

The series of $\text{CsMn}_x\text{Te}_{2-x}\text{O}_6$ ($x = 0.05$ to 0.43) with defect pyrochlore structure have been successfully prepared by solid state reaction. While the CsTe_2O_6 compound is rhombohedral, substituting Te with 0.05 Mn into the lattice leads destroys the octahedra ordering resulting in a cubic structure. Based on the XPS and XANES results, the substitution can be represented by two different formulas. When x is lower than 0.33, Mn^{3+} replaces Te^{4+} resulting in $\text{Cs}^{1+}(\text{Mn}^{3+})_x(\text{Te}^{4+})_{0.5-(3x/2)}(\text{Te}^{6+})_{1.5+(x/2)}\text{O}_6$. On the other hand, Te^{6+} are replaced by Mn^{3+} and Mn^{4+} when x is higher than 0.33 as can be described by $\text{Cs}^{1+}(\text{Mn}^{3+/4+})_x(\text{Te}^{6+})_{2-x}\text{O}_{6-\delta}$. The switch between the two schemes results in a sudden change in the cell parameter trend and the activation energy of conduction. To explain the differences in electrical properties, XPS at valence band region and O K -edge XANES were employed to probe the electronic structures and propose the schematic band structure diagrams. Based on the proposed diagrams, it is clear that $\text{CsMn}_x\text{Te}_{2-x}\text{O}_6$ are different from previously reported n -type $\text{CsAl}_x\text{Te}_{2-x}\text{O}_6$. Although the number of Te^{4+} state is higher in $\text{CsMn}_x\text{Te}_{2-x}\text{O}_6$ ($x < 0.33$) samples, the Te 5s states overlap with Mn 3d-O 2p states and become part of the valence band leading to the intrinsic semiconducting behavior. In addition, the energy of the Te 5s states in $\text{CsMn}_x\text{Te}_{2-x}\text{O}_6$ ($x < 0.33$) samples shows a correlation with unit cell parameters. Thus, it is expected that high conductivity would be achievable by compressing the Te^{4+} -O bond. On the other hand, the disappearance of Te^{4+} and lifting of conduction band minimum in the samples with $x \geq 0.33$ are causing the switching of substitution mechanism which lower the conductivity, although the occurrence of oxygen vacancies in samples with $x > 0.33$ raise valence band maximum.

4.7 References

- Abbate, M., Cruz, D., Zampieri, G., Briatico, J., Causa, M., Tovar, M., and Morikawa, E. (1997). The electronic structure of CaMnO_x with $2.66 \leq x \leq 3.00$. **Solid State Communications**. 103(1): 9-13.
- Alsac, A., Yildiz, A., Serin, T., and Serin, N. (2013). Improved conductivity of Sb-doped SnO_2 thin films. **Journal of Applied Physics**. 113(6): 063701.
- Arun, B., Suneesh, M., Sudakshina, B., Akshay, V., Chandrasekhar, K., and Vasundhara, M. (2018). Effects of Mn site substitution on magnetic ordering and critical behavior in $\text{Nd}_{0.67}\text{Sr}_{0.33}\text{MnO}_3$ manganite. **Journal of Physics and Chemistry of Solids**. 123: 327-335.
- Asokan, K., Chen, Y., Pao, C., Tsai, H., Lee, C. O., Lin, C., Lin, C. H., Hsueh, H. C., Ling, D. C., Pong, W. F., Chiou, J. W., Tsai, M.-H., Peña, O., and Moure, C. (2009). Effect of Co, Ni, and Cu substitution on the electronic structure of hexagonal YMnO_3 studied by x-ray absorption spectroscopy. **Applied Physics Letters**. 95(13): 131901.
- Balasubramanian, P., Nair, H. S., Tsai, H., Bhattacharjee, S., Liu, M., Yadav, R., Chiou, J., Lin, H., Pi, T., Tsai, M., Elizabrth, S., Pao, C., Wang, B., Chuang, C., and Pong, W. (2013). Valence band electronic structure of $\text{Nd}_{1-x}\text{Y}_x\text{MnO}_3$ using X-ray absorption, photoemission and GGA+ U calculations. **Journal of Electron Spectroscopy and Related Phenomena**. 189: 51-55.
- Blöchl, P. E. (1994). Projector augmented-wave method. **Physical Review B**. 50(24): 17953.
- Cai, S., Li, Y., Chen, X., Ma, Y., Liu, X., and He, Y. (2016). Optical and electrical properties of Ta-doped ZnSnO_3 transparent conducting films by sol-gel. **Journal**

of Materials Science: Materials in Electronics. 27(6): 6166-6174.

Chen, Z., Li, W., Li, R., Zhang, Y., Xu, G., and Cheng, H. (2013). Fabrication of highly transparent and conductive indium–tin oxide thin films with a high figure of merit via solution processing. **Langmuir.** 29(45): 13836-13842.

Dudarev, S., Botton, G., Savrasov, S., Humphreys, C., and Sutton, A. (1998). Electron-energy-loss spectra and the structural stability of nickel oxide: An LSDA+ U study. **Physical Review B.** 57(3): 1505.

Dudric, R., Vladescu, A., Rednic, V., Neumann, M., Deac, I., and Tetean, R. (2014). XPS study on $\text{La}_{0.67}\text{Ca}_{0.33}\text{Mn}_{1-x}\text{Co}_x\text{O}_3$ compounds. **Journal of Molecular Structure.** 1073; 66-70.

Fu, D.-x., Liu, Y.-z., Zhang, H.-g., Xie, L., and Li, B. (2018). The evolution of magnetization switching of LuCrO_3 by the effect of Mn doping. **Journal of Alloys and Compounds.** 735: 1052-1062.

Garvie, L., and Craven, A. (1994). High-resolution parallel electron energy-loss spectroscopy of Mn $L_{2,3}$ -edges in inorganic manganese compounds. **Physics and Chemistry of Minerals.** 21(4): 191-206.

Groult, D., Pannetier, J., and Raveau, B. (1982). Neutron diffraction study of the defect pyrochlores $\text{TaWO}_{5.5}$, HTaWO_6 , $\text{H}_2\text{Ta}_2\text{O}_6$, and $\text{HTaWO}_6 \cdot \text{H}_2\text{O}$. **Journal of Solid State Chemistry.** 41(3): 277-285.

Hishida, T., Ohbayashi, K., Kobata, M., Ikenaga, E., Sugiyama, T., Kobayashi, K., Okawa, M., and Saitoh, T. (2013). Empirical relationship between x-ray photoemission spectra and electrical conductivity in a colossal magnetoresistive manganite $\text{La}_{1-x}\text{Sr}_x\text{MnO}_3$. **Journal of Applied Physics.** 113(23): 233702.

- Kawazoe, H., Yanagi, H., Ueda, K., and Hosono, H. (2000). Transparent *p*-type conducting oxides: design and fabrication of pn heterojunctions. **MRS Bulletin**. 25(8): 28-36.
- Kim, S. W., Saito, Y., Hasegawa, T., Toda, K., Uematsu, K., and Sato, M. (2017). Development of a novel nontoxic vivid violet inorganic pigment—Mn³⁺-doped LaAlGe₂O₇. **Dyes and Pigments**. 136: 243-247.
- Kresse, G., and Furthmüller, J. (1996). Efficiency of ab-initio total energy calculations for metals and semiconductors using a plane-wave basis set. **Computational Materials Science**. 6(1): 15-50.
- Kresse, G., and Hafner, J. (1993). Ab initio molecular dynamics for liquid metals. **Physical Review B**. 47(1): 558.
- Kresse, G., and Joubert, D. (1999). From ultrasoft pseudopotentials to the projector augmented-wave method. **Physical Review B**. 59(3): 1758.
- Li, J., Siritanon, T., Stalick, J. K., Sleight, A. W., and Subramanian, M. (2011). Structural studies and electrical properties of Cs/Al/Te/O phases with the pyrochlore structure. **Inorganic Chemistry**. 50(12): 5747-5754.
- Li, L., Feng, X., Nie, Y., Chen, S., Shi, F., Xiong, K., Ding, W., Qi, X., Hu, J., Wei, Z., Wan, L.-J., and Xia, M. (2015). Insight into the effect of oxygen vacancy concentration on the catalytic performance of MnO₂. **ACS Catalysis**. 5(8): 4825-4832.
- Li, Y., Yao, W., Zong, R., and Zhu, Y. (2016). Fabrication of Wide-Range-Visible Photocatalyst Bi₂WO_{6-x} nanoplates via Surface Oxygen Vacancies. **Scientific Reports**. 6: 19347.
- Marschall, R., Mukherji, A., Tanksale, A., Sun, C., Smith, S. C., Wang, L., and Lu, G.

- Q. M. (2011). Preparation of new sulfur-doped and sulfur/nitrogen co-doped CsTaWO₆ photocatalysts for hydrogen production from water under visible light. **Journal of Materials Chemistry**. 21(24): 8871-8879.
- Mikami, M., Ando, N., and Funahashi, R. (2005). The effect of Ag addition on electrical properties of the thermoelectric compound Ca₃Co₄O₉. **Journal of Solid State Chemistry**. 178(7): 2186-2190.
- Pellegrin, E., Tjeng, L., De Groot, F., Hesper, R., Sawatzky, G., Moritomo, Y., and Tokura, Y. (1997). Soft X-ray magnetic circular dichroism study of the colossal magnetoresistance compound La_{1-x}Sr_xMnO₃. **Le Journal de Physique IV**. 7(C2): C2-405-C402-408.
- Perdew, J. P., Burke, K., and Ernzerhof, M. (1996). Generalized gradient approximation made simple. **Physical Review Letters**. 77(18): 3865.
- Podgornov, E., Prosvirin, I., and Bukhtiyarov, V. (2000). XPS, TPD and TPR studies of Cs–O complexes on silver: their role in ethylene epoxidation. **Journal of Molecular Catalysis A: Chemical**. 158(1): 337-343.
- Rahimnejad, S., He, J. H., Chen, W., Wu, K., and Xu, G. Q. (2014). Tuning the electronic and structural properties of WO₃ nanocrystals by varying transition metal tungstate precursors. **RSC Advances**. 4(107): 62423-62429.
- Robin, M. B., and Day, P. (1968). Mixed valence chemistry-a survey and classification. **In Advances in Inorganic Chemistry and Radiochemistry**. (Vol. 10, pp. 247-422): Elsevier.
- Sato, H., Ido, T., Tajima, S., Yosida, M., Tanabe, K., and Uchida, S. (1991). Superconducting and normal states of Ba_{1-x}K_xBiO₃ studied by high quality thin films. **Physica C: Superconductivity**. 185: 1343-1344.

- Shannon, R. D. (1976). Revised effective ionic radii and systematic studies of interatomic distances in halides and chalcogenides. **Acta Crystallographica Section A**. 32(5): 751-767.
- Shannon, R. T., and Prewitt, C. T. (1969). Effective ionic radii in oxides and fluorides. **Acta Crystallographica Section B**. 25(5): 925-946.
- Shukla, D., Mollah, S., Kumar, R., Thakur, P., Chae, K., Choi, W., and Banerjee, A. (2008). Effect of Ti substitution on multiferroic properties of BiMn_2O_5 . **Journal of Applied Physics**. 104(3): 033707.
- Siritanon, T., Laurita, G., Macaluso, R. T., Millican, J. N., Sleight, A. W., and Subramanian, M. (2009). First observation of electronic conductivity in mixed-valence tellurium oxides. **Chemistry of Materials**. 21(23): 5572-5574.
- Siritanon, T., Li, J., Stalick, J. K., Macaluso, R. T., Sleight, A. W., and Subramanian, M. (2011). $\text{CsTe}_2\text{O}_{6-x}$: Novel Mixed-Valence Tellurium Oxides with Framework-Deficient Pyrochlore-Related Structure. **Inorganic Chemistry**. 50(17): 8494-8501.
- Siritanon, T., Sleight, A., and Subramanian, M. (2011). Compositionally controlled rhombohedral to cubic phase transition in $\text{CsTe}_{2-x}\text{W}_x\text{O}_6$ related to pyrochlore structure. **Materials Research Bulletin**. 46(12): 2494-2496.
- Subramanian, M., Aravamudan, G., and Rao, G. S. (1983). Oxide pyrochlores-a review. **Progress in Solid State Chemistry**. 15(2): 55-143.
- Sultan, K., Ikram, M., Gautam, S., Lee, H.-K., Chae, K. H., and Asokan, K. (2015). Electrical and magnetic properties of the pulsed laser deposited Ca doped LaMnO_3 thin films on Si (100) and their electronic structures. **RSC Advances**. 5(85): 69075-69085.

- Sun, C., Wang, Y., Zou, J., and Smith, S. C. (2011). A formation mechanism of oxygen vacancies in a MnO_2 monolayer: a DFT+U study. **Physical Chemistry Chemical Physics**. 13(23): 11325-11328.
- Thakur, P., Chae, K., Whang, C., Chang, G., Shukla, D., Mollah, S., and Kumar, R. (2008). X-ray Absorption and Emission Spectroscopic Studies of $\text{BiMn}_{2-x}\text{Ti}_x\text{O}_5$ ($0 \leq x \leq 0.5$). **Journal of Korean Physical Society**. 53: 1449.
- Tompsett, D. A., Middlemiss, D. S., and Islam, M. S. (2012). Importance of anisotropic Coulomb interactions and exchange to the band gap and antiferromagnetism of $\beta\text{-MnO}_2$ from DFT+U. **Physical Review B**. 86(20): 205126.
- Tompsett, D. A., Parker, S. C., Bruce, P. G., and Islam, M. S. (2013). Nanostructuring of $\beta\text{-MnO}_2$: The important role of surface to bulk ion migration. **Chemistry of Materials**. 25(4): 536-541.
- Van den Berghe, S., Laval, J.-P., Gaudreau, B., Terryn, H., and Verwerft, M. (2000). XPS investigations on cesium uranates: mixed valency behaviour of uranium. **Journal of Nuclear Materials**. 277(1): 28-36.
- Wahayee, A., Eknapakul, T., Chanlek, N., Kongnok, T., Rattanasuporn, S., Nakajima, H., Meevasana W., and Siritanon, T. (2017). Electrical properties of $(\text{Cs}_{1-x}\text{A}_x)\text{Al}_{0.33}\text{Te}_{1.67}\text{O}_6$ (A= K and Rb) mixed valence pyrochlores. **Journal of Alloys and Compounds**. 718: 215-222.
- Wahoud, F., Guillot, J., Audinot, J., Bertrand, P., Delcorte, A., and Migeon, H. (2014). Dielectric breakdown during Cs^+ sputtering of polyvinyl chloride. **Applied Surface Science**. 293: 85-89.
- Wang, X., Wang, X., Di, Q., Zhao, H., Liang, B., and Yang, J. (2017). Mutual effects

of fluorine dopant and oxygen vacancies on structural and luminescence characteristics of F doped SnO₂ nanoparticles. **Materials**. 10(12): 1398.

Wenas, W. W., Yamada, A., Takahashi, K., Yoshino, M., and Konagai, M. (1991).

Electrical and optical properties of boron-doped ZnO thin films for solar cells grown by metalorganic chemical vapor deposition. **Journal of Applied Physics**. 70(11): 7119-7123.

Zhang, K., Du, Y., Sushko, P., Bowden, M. E., Shutthanandan, V., Qiao, L., Cao, G.,

Gai, Z., Sallis, S., and Piper, L. Electronic and magnetic properties of epitaxial perovskite SrCrO₃ (001). (2015). Electronic and magnetic properties of epitaxial perovskite SrCrO₃ (001). **Journal of Physics: Condensed Matter**. 27(24): 245605.

Zhang, K. H., Du, Y., Papadogianni, A., Bierwagen, O., Sallis, S., Piper, L. F.,

Bowden, M. E., Shutthanandan, V., Sushko, P.V., and Chambers, S. A. (2015). Perovskite Sr-Doped LaCrO₃ as a New *p*-Type Transparent Conducting Oxide. **Advanced Materials**. 27(35): 5191-5195.

CHAPTER V

ENHANCEMENT PHOTOCATALYTIC ACTIVITY OF KNbTeO₆ DEFECT PYROCHLORES THROUGH BAND ENGINEERING

5.1 Abstract

To study the effects of Ag, Cu, and Sn substitutions on photocatalytic activity of KNbTeO₆ compounds, the KNbTeO₆ parent compound has been successfully prepared by solid state method. Its Ag, Cu, and Sn doped were obtained by facile ion exchange method. All of the samples were characterized by X-ray diffraction (XRD), Thermogravimetric analysis (TGA), Scanning electron microscope-energy dispersive X-ray spectroscopy (SEM-EDS), X-ray photoelectron spectroscopy (XPS), and UV-Vis diffuse reflectance spectroscopic (DRS). To describe the electronic structure of all compounds, we proposed simple schematic band structures of the compounds based on the XPS at valence band region and UV-Vis absorption spectra. The reduction of band gap energy in KNbTeO₆ from 3.38 eV to 2.76 (Ag-doped), 3.21 (Cu-doped), and 2.51 eV (Sn-doped), are attributed to the up of valence band caused by the formation of Ag 4*d*, Cu 3*d*, and Sn 5*s* states in each samples overlap with O 2*p* states at the top of the valence band. As a result, the Ag⁺, Cu²⁺, and Sn²⁺-doping exhibited higher photocatalytic activity than pure KNbTeO₆. However, the factor such as more surface adsorbed oxygen species, stronger light absorption in visible region, narrower band

gap energy, and wider bandwidth of valence band were supposed to be the reasons for the highest activity observed of Sn-doped sample. The mechanism of Methylene blue photodegradation was studied by using different quenchers in the presence of Sn^{2+} -doped KNbTeO_6 as photocatalyst. The hydroxyl radicals ($\bullet\text{OH}$) is major active species, while, photogenerated holes (h^+) and superoxide radicals (O_2^-) are minor active species in this photodegradation process.

5.2 Introduction

During the past decades, wastewater containing various dyes was one of the most important environmental issues. The semiconducting materials have been synthesized and studied to apply for the environmental remediation in a photodegradation process (Molla et al., 2016; Tian et al., 2012; Wu et al., 1999). Among all, photocatalytic degradation using oxides containing post-transition element compounds has attracted great attention. Many oxides containing post-transition metals have been reported to show photodegradation activity toward organic dyes. For example, BiSbO_4 , $\text{La}_2\text{Sn}_2\text{O}_7$, and Bi_2WO_6 have been used as efficient photocatalysts (Fu et al., 2005; Lin et al., 2006; Zeng et al., 2007).

It is well known that, good photocatalysts should have large absorption in the visible region, large separation of electron-hole pairs and suitable band potentials to produce active species (Ansari et al., 2016; Jitta et al., 2015; Weber et al., 2012). Incorporation of Ag^+ , Cu^{2+} , and Sn^{2+} in crystal lattice can create $\text{Ag } 4d$, $\text{Cu } 3d$, and $\text{Sn } 5s$ state near top of valence band leading to increase absorption in the visible light region (Guje et al., 2015; Sun et al., 2012). Recently, several researches about improving photocatalytic performance of KBB'O_6 defect pyrochlore structure using

facile ion exchange of K^+ with ions such as Ag^+ , Sn^{2+} , Cu^{2+} , Bi^{3+} , Sm^{3+} , Eu^{3+} , and Gd^{3+} have been reported (Guje et al., 2016; Guje, Gundeboina, Reddy, et al., 2016; Ravi et al., 2013). This high exchangeability is due to the fact that K^+ locate in large hexagonal tunnels which are built up from corner sharing networks of $B(B')O_6$ octahedra (Guje et al., 2016; Ravi et al., 2014). However, tellurium containing defect pyrochlores are less investigated in their photocatalytic properties.

To understand the structure-photocatalytic property relationships of tellurium containing defect pyrochlores, we studied the electronic structure of $KNbTeO_6$ and Ag^+ , Cu^{2+} , and Sn^{2+} substituted $KNbTeO_6$. Photodegradation activity of Methylene blue in the presence of these materials as catalysts is studied. In addition, photocatalytic mechanism in Methylene blue degradation is investigated with the use of appropriate quenchers.

5.3 Experiments

5.3.1 Preparation of $KNbTeO_6$

$KNbTeO_6$ parent compound was prepared by solid state method using KNO_3 (Carlo Erba, 99+%), Nb_2O_5 (Acros Organic, 99+%), and TeO_2 (Acros Organic, 99+%). Stoichiometric mixtures of the reactants were weighed and ground in an agate mortar. The mixed powder were pressed into pellets and heated at 550 °C for 5 h. After that, the samples were reground, pressed into pellets, and sintered at 650 °C for 24 h in air.

5.3.2 Preparation of Ag^+ , Cu^{2+} , and Sn^{2+} doped $KNbTeO_6$

Ion exchange method was used to prepare Ag, Cu, and Sn doped

KNbTeO₆ samples. About 1 g of KNbTeO₆ were added to 100 mL of 0.0225 M solution of AgNO₃, CuCl₂, or SnCl₂.2H₂O and stirred for 24 h at room temperature. The resultant solids were washed several times with double distilled water and dried in air.

5.3.3 Characterizations

Powder X-ray diffraction patterns were recorded by a Bruker D2 Phaser diffractometer (Cu K α radiation, $\lambda = 1.5406 \text{ \AA}$) for phase identification. The decomposition of absorbed and lattice water were investigated by thermogravimetric analysis (TGA) under nitrogen gas with a heating rate of 5 °C/min. The elemental composition of the samples were investigated by energy dispersive X-ray spectroscopy (EDS) using the Oxford Instrument, model X-Max 50 mm. X-ray photoelectron spectroscopy (XPS) were carried out at BL5.3: SUT-NANOTEC-SLRI, Synchrotron Light Research Institute, Thailand. The XPS spectra were recorded by a PHI5000 VersaProbe II XPS instruments (ULVAC-PHI, Japan) using Al K α monochromatic X-ray (1486.6 eV). The C 1s binding energy at 284.8 eV was used as a reference. Agilent UV-Vis-NIR spectrophotometer modeled Carry 5000 was used for optical diffuse reflectance spectroscopy (DRS). The diffuse reflectance (%R) spectra were recorded in the wavelength range of 200-2000 nm with the double beam mode.

5.3.4 Photocatalytic Test

The photocatalytic activity of all samples was tested by photodegradation of methylene blue (MB) under light exposure using 150W halogen lamp (The spectrum of halogen lamp is shown in Figure C2). The solutions were kept

at constant temperature of 27 °C during the test. Typically, a mixture of 50 mL of methylene blue solution (3 mg/mL) and 0.05g of catalysts was stirred in dark for 1 h to achieve an absorption-desorption equilibrium. At every 1 h, 5 mL of solution was collected and centrifuged to remove catalysts. The concentration of MB solution was determined by a UV-Vis spectrophotometer with the absorbance at 664 nm. The photodegradation efficiencies were calculated by

$$D = [(C_0 - C_f) / C_0] \times 100 \quad [1]$$

where D is percent degradation, C_0 and C_f are initial and final concentration of dye, respectively (Jitta, Guje, et al., 2015).

To quantitatively analyze hydroxyl radicals in the photocatalytic process, the photocatalytic hydroxylation of terephthalic acid (TA) was observed by the measurement of fluorescence intensity of 2-hydroxy-terephthalic acid (2-TAOH) with excitation energy at 315 nm (Li et al., 2017). The measurement procedure was as follows: TA was added into NaOH solution with a concentration of 1.0 mmol/L, to obtain a 0.25 mmol/L TA solution. Exactly 50 mg of the catalyst was added into 50 mL of TA solution. The mixture was stirred in dark for 1 h to achieve absorption-desorption equilibrium and ensure the uniform dispersion of the catalyst. Subsequently, the solution was irradiated by a 150 W halogen lamp. At a given time interval (0 h and 3 h), 10 mL of the reaction solution was sampled and the catalyst was removed by centrifugation. A fluorescence spectrophotometer was used to measure the PL spectrum of the reaction solution. In addition, we investigated the active species in photocatalytic reaction to studied photodegradation mechanism. The hydroxyl radicals ($\bullet\text{OH}$), holes (h^+) and superoxide radicals ($\text{O}_2^{\bullet-}$) were investigated

by using 0.2 mM of isopropanol ($\bullet\text{OH}$ scavenger), sodium oxalate (h^+ scavenger), and benzoquinone ($\text{O}_2\bullet^-$ scavenger) to the reactions (Jitta et al., 2015; Huang et al., 2014).

5.4 Results and discussion

5.4.1 Crystal structure

Powder X-ray diffraction (XRD) pattern of KNbTeO_6 (KNTO) and Ag, Cu and Sn doped- KNbTeO_6 (AgKNTO, CuKNTO, and, SnKNTO) were recorded for phase identification (Figure 5.1). All diffraction peaks of KNTO can be indexed as AB_2O_6 cubic defect pyrochlore with $\text{Fd}\bar{3}\text{m}$ space group, no impurity is observed (Guje et al., 2015; Guje et al., 2015; Jitta et al., 2015). Similarly, a single-phase AgKNTO, CuKNTO, and, SnKNTO with cubic defect pyrochlore structure were successfully obtained by ion exchange method. The unit cell parameters of KNTO, AgKNTO, CuKNTO, and SnKNTO were calculated by Le Bail refinement as summarized in Table 1. Although replacing K^+ (1.51 Å) with smaller Ag^+ (1.28 Å), Cu^{2+} (0.73 Å) and Sn^{2+} (1.27 Å) ions in lattice should lead to small unit cell parameters (Shannon, 1976), the obtained results do not follow this trend. The cell parameters of AgKNTO, CuKNTO and SnKNTO are slightly larger than that of KNTO. The most probable explanation is the incorporation of water in the crystal lattice during the ion exchange reaction (Guje et al., 2016; Jitta et al., 2015).

Thus, TGA technique was used to identify the presence of lattice water. As reported in previous works, the loss of adsorbed water is observed at temperature 50-250 °C, while weight loss at around 250-600 °C corresponds to both adsorbed and lattice water (Guje et al., 2016; Guje et al., 2015). In this work, the loss of both adsorbed and lattice water was observed at temperature 50-500 °C (Figure 5.2).

The presence of both absorbed and lattice water about 1.5-4.5% are close to previously reported values (Guje et al., 2016; Guje et al., 2015). It is normal to have water in the defect pyrochlore because the structure contains lots of vacant sites that can accommodate water molecules (Jitta et al., 2015).

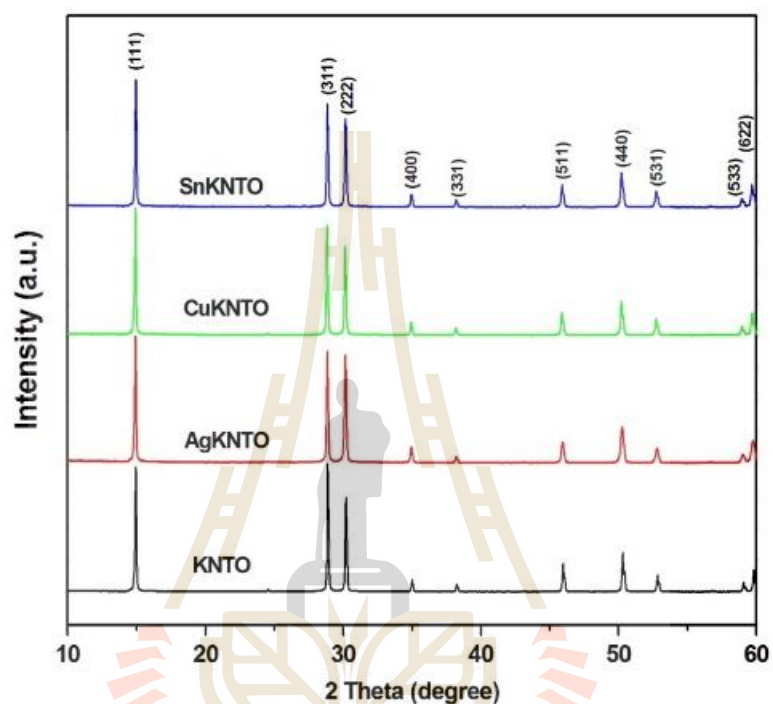


Figure 5.1 Powder X-ray diffraction patterns of KNT0, AgKNT0, CuKNT0, and SnKNT0.

Table 5.1 Cell parameter (a) and elemental composition of all compounds.

Compounds	Cell parameter a (Å)	*Composition
KNT0	10.250	KNbTeO_6
AgKNT0	10.250	$\text{K}_{0.8}\text{Ag}_{0.2}\text{NbTeO}_6$
CuKNT0	10.267	$\text{K}_{0.8}\text{Cu}_{0.1}\text{NbTeO}_6$
SnKNT0	10.280	$\text{K}_{0.7}\text{Sn}_{0.15}\text{NbTeO}_6$

*calculated from energy dispersive X-ray spectroscopy (EDS) elemental mapping

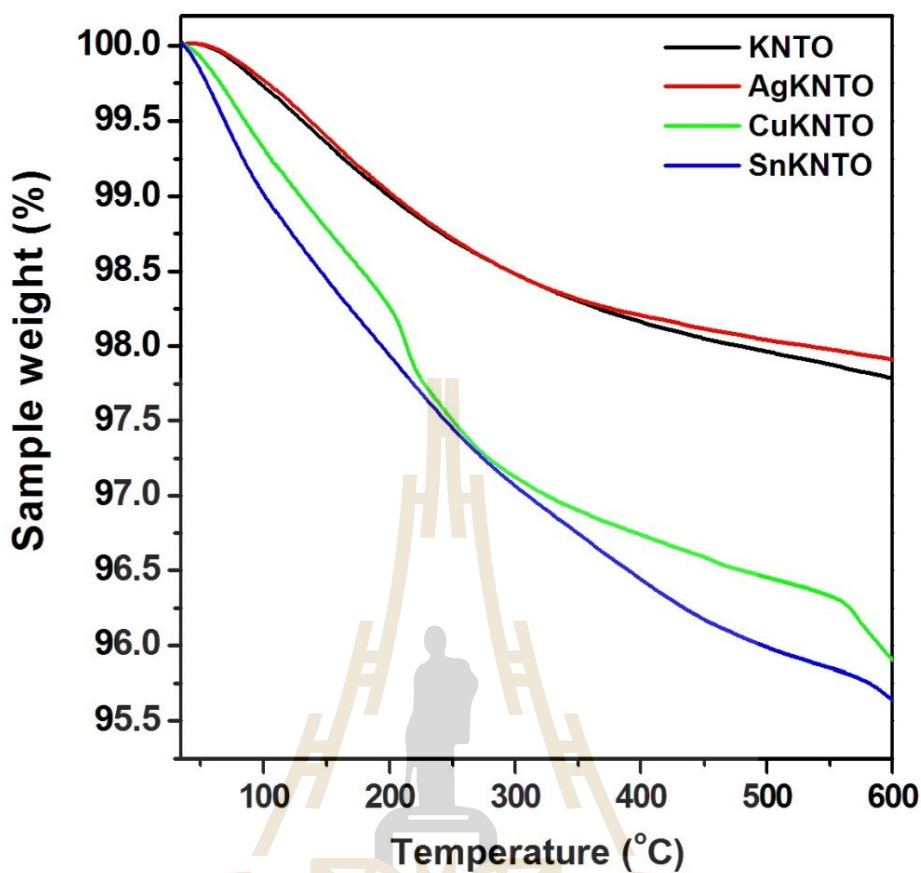


Figure 5.2 The TGA profiles of KNTO, AgKNTO, CuKNTO, and SnKNTO.

5.5.2 Morphology

SEM images of KNTO, AgKNTO, CuKNTO, and SnKNTO (Figure 5.3) show irregularly discontinuous lumps shape without significant differences particle sizes which indicates that there are no changes in the morphology and particle size after ions exchange. EDS elemental mapping was used to confirm the presence of each elemental. EDS mapping images of all compounds are shown in Figure 5.4. According to the mapping, all elements are homogeneously distributed in the samples. While KNTO contains K, Nb, and Te as expected, the doped samples additionally contain doping elements. In addition, the presence of K in doped samples suggests

5.4.3 X-ray photoelectron spectroscopy (XPS).

XPS was used to study the elemental composition and oxidation states of elements (Figure 5.5). The obtained binding energies of K $2p$ XPS spectra of all compounds (Figure 5.6(a)) are characteristics of K^+ (Atuchin et al., 2012; Moggia et al., & Cornaglia, 2003). The presence of K $2p$ XPS spectra in all samples indicates that K is only partially exchanged with Ag, Cu, and Sn. Figure 5.6(b) show the Ag $3d$, Cu $2p$, and Sn $3d$ XPS spectra of AgKNTO, CuKNTO, and SnKNTO. The Ag $3d$ core level spectra with binding energy about 367.5 and 373.6 eV confirms the +1 oxidation state of Ag (Kruczek et al., 2006). The Cu $2p_{3/2}$ and Cu $2p_{1/2}$ spectra located at 933.2 and 953.2 eV suggest Cu^{2+} (Xu et al., 2013). The binding energy at about 486.6 and 495.0 eV for Sn $3d_{5/2}$ and Sn $3d_{3/2}$ spectra, respectively are characteristics of Sn^{2+} (Wang et al., 2013). It is interesting to note that the elemental analysis based on EDS (Table 5.1) gives compositions with charge neutrality. Additionally, it seems that at this studied condition, only about 20% of K^+ can be exchanged and the oxidation state of the exchanging ions determines how much each will be in the lattice.

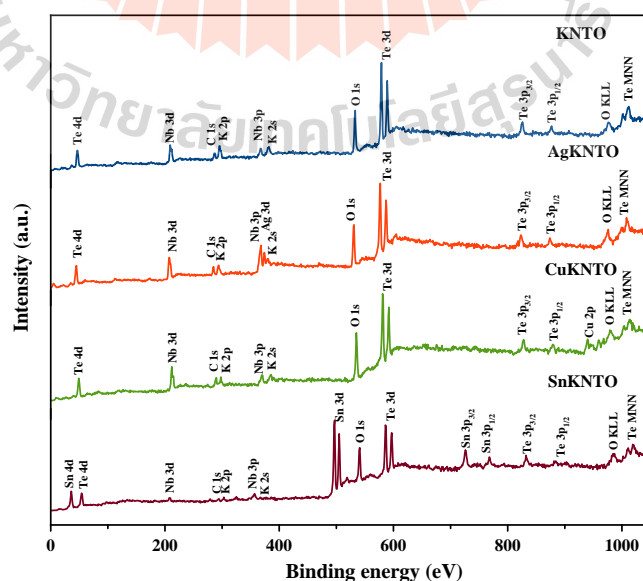


Figure 5.5 Survey XPS spectra of KNTO, AgKNTO, CuKNTO, and SnKNTO.

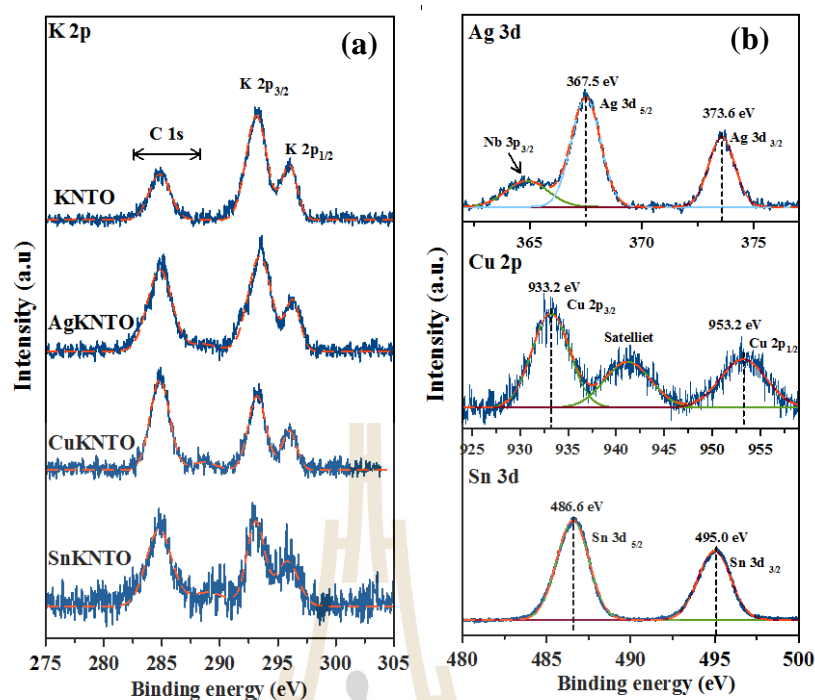


Figure 5.6 K 2p (a) and Ag 3d, Cu 2p and Sn 3d (b) XPS spectra of KNTO, AgKNTO, CuKNTO, and SnKNTO.

The Nb 3d XPS spectra of all compounds are shown in Figure 5.7(a). The binding energy at about 207.3-207.4 and 210.0-210.1 eV are attributed to the Nb⁵⁺ 3d_{5/2} and 3d_{3/2} respectively (Liu et al., 2016; Qamar et al., 2015). The binding energy values of Te 3d_{5/2} and Te 3d_{3/2} observed at 576.4-576.8 and 586.8-587.2 eV (Figure 5.7(b)), respectively, indicate that Te of all compounds is in +6 oxidation state (Sathiya et al., 2013). The observation of O 1s spectrum (Figure 5.8) is asymmetric and can be deconvoluted into lattice oxygen (O_L) located at binding energy around 530.4 – 530.7 eV (Lee et al., 2014; Mekki et al., 2005) and surface adsorbed oxygen species (O_{ad}) located at higher binding energy peaks, such as carbonyl species (C 1s peak showed also a small component at 286-289 eV), hydroxyl species, adsorbed molecular water and oxygen (Chen et al., 2018; Liu et al., 2016). However, the slight

shift towards higher binding energy of Nb 3d, Te 3d, and O_L after ion exchange could be attributed to be the different environment and lattice distortion (Su et al., 2012). As previously reported, replacing with smaller cation at A site of AB₂O₆ defect pyrochlore which leads to the lattice distortion (Garcia-Martin et al., 1991; Thorogood et al., 2009).

The presence of hydroxyl species, molecular water, and oxygen on the surface of the catalyst has a positive effect on enhancement of photocatalysis (Jun et al., 2015; Veldurthi et al., 2014). Generally, photoexcited holes were trapped by surface adsorbed water and generate hydroxyl radical while surface adsorbed oxygen trapped photoexcited electron to produce superoxide radical. Therefore, having a lot of hydroxyl, molecular waters, and oxygen on the surface can improve the formation of the active species.

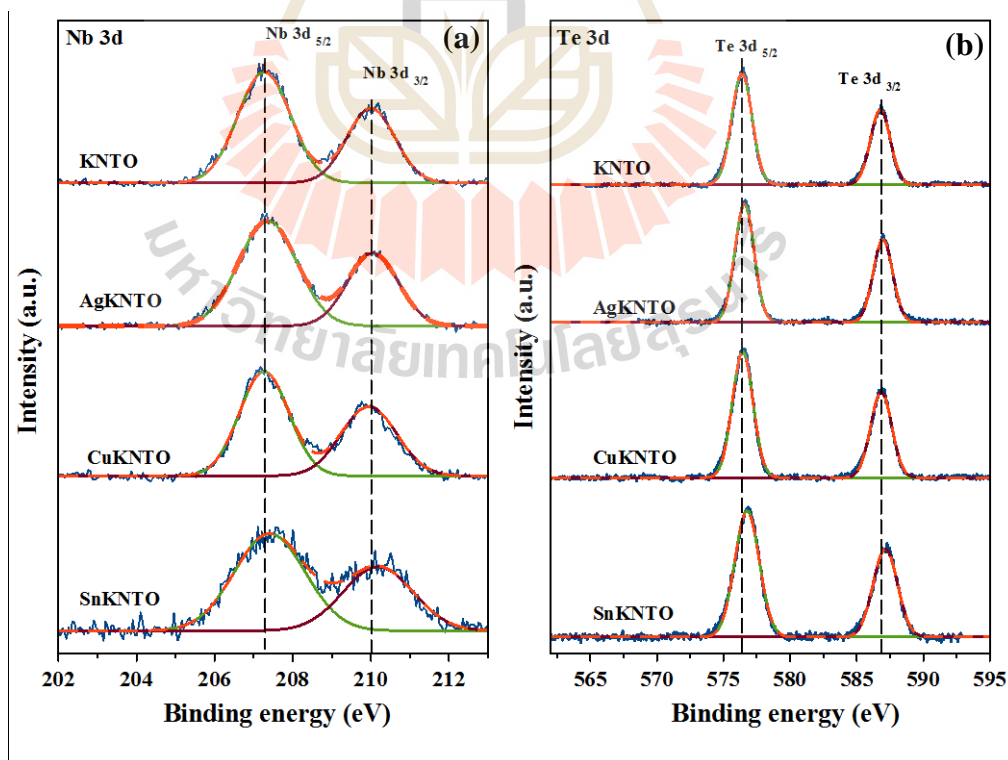


Figure 5.7 Nb 3d (a) and Te 3d (b) XPS spectra of KNTO, AgKNTO, CuKNTO, and SnKNTO.

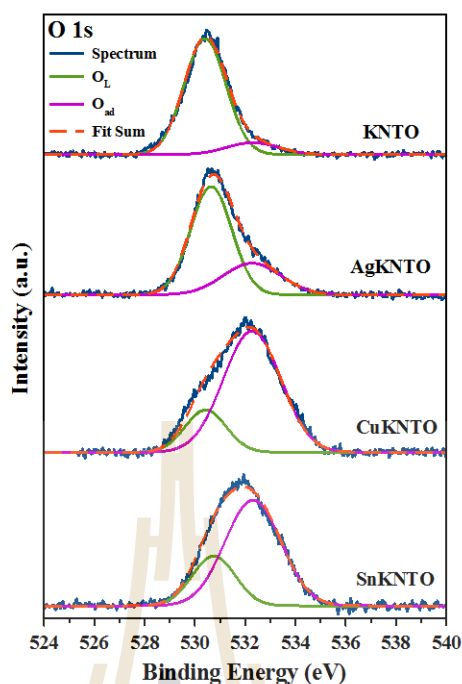


Figure 5.8 O 1s XPS spectra of KNTO, AgKNTO, CuKNTO, and SnKNTO.

XPS spectra at valence band region give useful information about the electronic band structure. To study the valence band feature, the spectra of all compounds were recorded as shown in Figure 5.9. The valence band of KNTO, denoted A, is predominantly from the hybridization of O 2*p*, Nb 4*d*, and Te 5*s* (Kruczek et al., 2006; Norman and Botana, 2017). Comparing to KNTO, the shape of valence band of AgKNTO, CuKNTO, and SnKNTO are different due to owning the domination of guest ions orbitals (Ag 4*d*, Cu 3*d*, and Sn 5*s*) which hybridizes with O 2*p*, Nb 4*d*, and Te 5*s* states. A small shoulder at the top of valence band is observed in the substituted samples which result in wider bandwidth comparing to KNTO and cause a shift in the top of valence band position toward Fermi level (E_F). These shoulder are contributed by Sn 5*s*, Cu 3*d* and Ag 4*d*, similar observations are also observed in previous works (Harb et al., 2014; Hosogi et al., 2008; Mahmood et al., 2014).

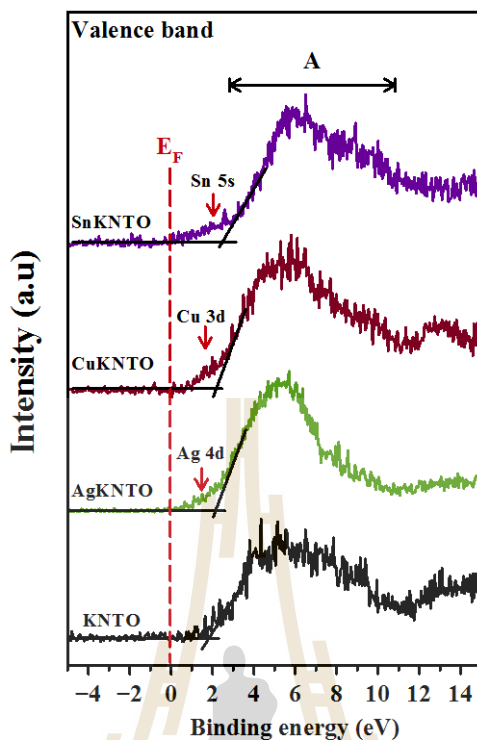


Figure 5.9 XPS at Valence band of KNTO, AgKNTO, CuKNTO, and SnKNTO.

5.4.4 Optical properties

The UV-Vis absorption of the KNTO, AgKNTO, CuKNTO, and SnKNTO are shown in Figure 5.10(a). Clearly, the red-shift of optical absorption edge was observed from the ion exchanged compounds. Doping with Ag^+ , Cu^{2+} and Sn^{2+} can increase absorption in the visible light region, which affects the sample color (inset of Figure 5.10(a)). The band gap energies of the samples are estimated from the extrapolation of the plot of $(K\hbar\nu)^{1/2}$ versus photon energy ($\hbar\nu$) (Figure 5.10(b)) (Guje et al., 2015; Jitta et al., 2015; Ravi et al., 2013), where K is reflectance transformed according to Kubelka-Munk function $[K = (1-R)^2/2(R)]$. In this function, $R = (\%R_{\text{sample}}/\%R_{\text{standard}})$ (Morales et al., 2007). The band gap energy value of KNTO, AgKNTO, CuKNTO, and SnKNTO are 3.38, 2.76, 3.21, and 2.51 eV, respectively.

Based on the XPS at valence band region and UV-Vis absorption spectra, it is obvious that the significant red-shift of the optical absorption edge in ion-exchanged samples are attributed to the shift of the valence bands as a result of Ag 4*d*, Cu 3*d*, and Sn 5*s* states. In addition, hybridization of Ag 4*d*, Cu 3*d*, or Sn 5*s* and O 2*p* orbitals broadens the valence band (Kurra et al., 2019; Veldurthi et al., 2014) which to increases the mobility of photogenerated holes in valence band (Hosogi et al., 2008).

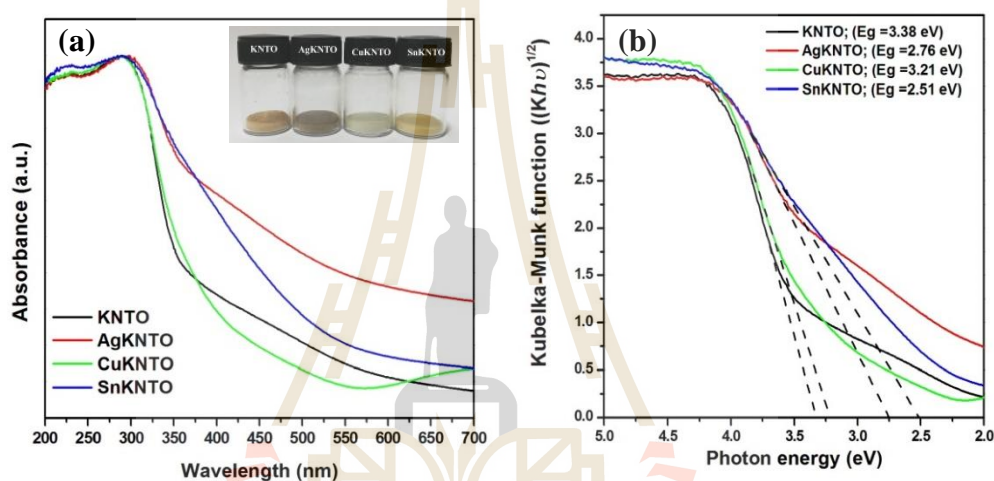


Figure 5.10 UV-Vis absorption spectra (a), sample color (inset), and Kubelka-Munk plot (b) of KNTO, AgKNTO, CuKNTO, and SnKNTO.

5.4.5 Photocatalytic activity

The photocatalytic performance of KNTO, AgKNTO, CuKNTO, and SnKNTO was investigated by methylene blue (MB) photodegradation under UV-Visible light irradiation. Figure 5.11(a) shows photocatalytic activity of all compounds compared with blank (MB). We found that Ag⁺, Cu²⁺, and Sn²⁺-doped KNbTeO₆ exhibit significantly higher photocatalytic performance than pure KNbTeO₆ (Figure 5.11(b)).

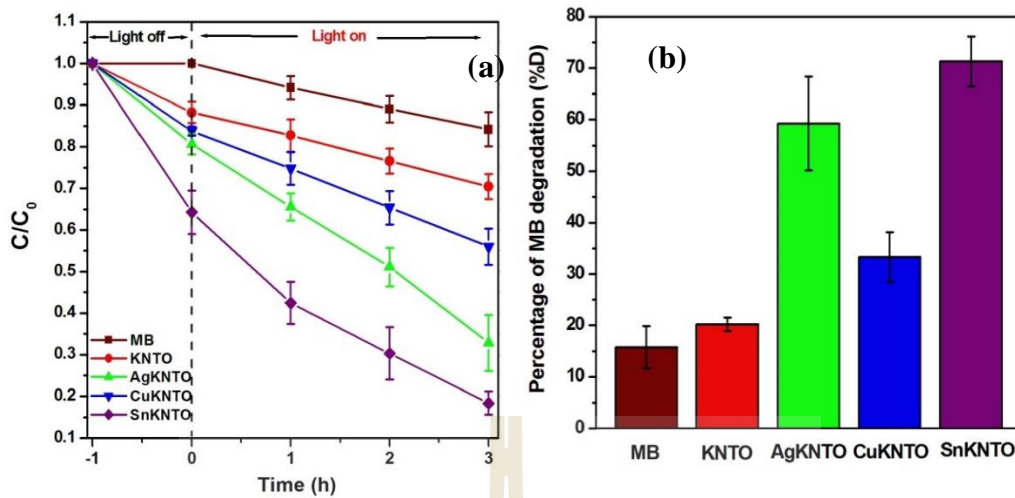


Figure 5.11 The photocatalytic activity (a) and the percentage MB degradation after 3 h of UV-Visible light irradiation (b) of KNTQ, AgKNTQ, CuKNTQ, and SnKNTQ.

In addition, the pseudo first order kinetics (Langmuir–Hinshelwood model) was used to investigate the reaction kinetics of the MB photodegradation process (Figure 5.12), as shown in the following equation (Ravi et al., 2013; Wang et al., 2016):

$$\ln(C_0/C) = k_{app}t \quad [1]$$

where C_0 is the initial concentration of the MB (mg/L), C is MB concentration at time t , (mg/L), and k_{app} is the rate constant of the apparent pseudo first order reaction (h^{-1}). The half-life time of the pseudo first order reaction ($t_{1/2}$) can be calculated by (Ravi et al., 2013).

$$t_{1/2} = \ln 2 / k_{app} \quad [2]$$

The rate constant and half-life time values of all samples for MB photodegradation are shown in Table 5.2. From the result, it can be conclude that the

SnKNTO, AgKNTO, and CuKNTO compounds display higher rate constants than KNTO, respectively. It means that SnKNTO compound has higher photocatalytic efficiency than KNTO, CuKNTO, and AgKNTO, respectively.

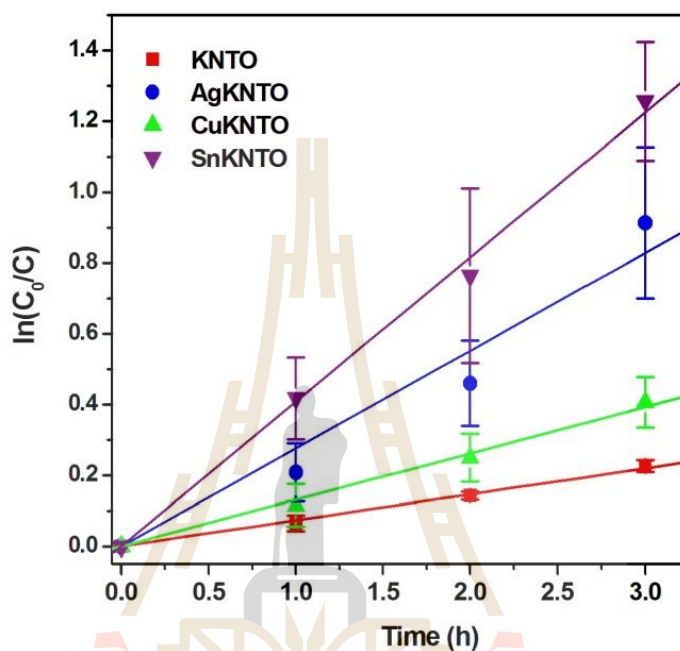


Figure 5.12 Kinetics plot for MB photodegradation in the presence of KNTO, AgKNTO, CuKNTO, and SnKNTO.

Table 5.2 The apparent pseudo first order rate constant (k_{app}), half-life time ($t_{1/2}$) and correlation coefficient (R^2) of KNTO, AgKNTO, CuKNTO, and SnKNTO.

Photocatalyst	k_{app} (h^{-1})	$t_{1/2}$ (h)	R^2
KNTO	0.073	9.44	0.996
AgKNTO	0.280	2.48	0.955
CuKNTO	0.132	5.26	0.994
SnKNTO	0.413	1.68	0.997

The photodegradation performance shows obvious correlation with the band gap energy. Catalysts with lower band gap energies and broader valence band shows higher efficiency (Jitta et al., 2015; Ravi et al., 2014; Ravi et al., 2013). However, the higher surface adsorbed hydroxyl, water, and oxygen also play roles in photocatalytic performance of catalysts because the photogenerated electron and hole can react easily with surface adsorbed oxygen species to form hydroxyl and superoxide radicals (Huang et al., 2014). In a photocatalytic process, when light is irradiated on the catalysts, holes and electrons are generated in the valence band and conduction band, respectively. These holes migrate to the surface of the catalyst and reacts with hydroxyl and water to form hydroxyl radicals. On the other hand, electrons in the conduction band on the catalyst surface can reduce molecular oxygen to form superoxide radical. Some superoxide radical can be neutralized by protons in water and finally form hydroxyl radical. It is well known that $\bullet\text{OH}$ radical is a very powerful chemical oxidant in the photocatalytic oxidation of organic pollutants and it is an important indication of photocatalysts efficiency. Hence, we investigate the generation and concentration of $\bullet\text{OH}$ radicals in the photocatalytic process using the photocatalytic hydroxylation of terephthalic acid (TA). Terephthalic acid (TA) reacts with $\bullet\text{OH}$ radical to form 2-hydroxy terephthalic acid (TAOH) which gives luminescence when excited by photon with appropriate energy (Li et al., 2017). Figure 5.13 displays the photoluminescence of aqueous TA solutions in the presence of KNTO, AgKNTO, CuKNTO, and SnKNTO catalysts under visible light irradiation after 3 h. The fluorescence intensity indicate the concentration of $\bullet\text{OH}$ radicals. Among all catalysts, SnKNTO shows highest PL intensity which can be attributed to the highest concentration of $\bullet\text{OH}$ radicals. This result is consistent with photoactivity

results.

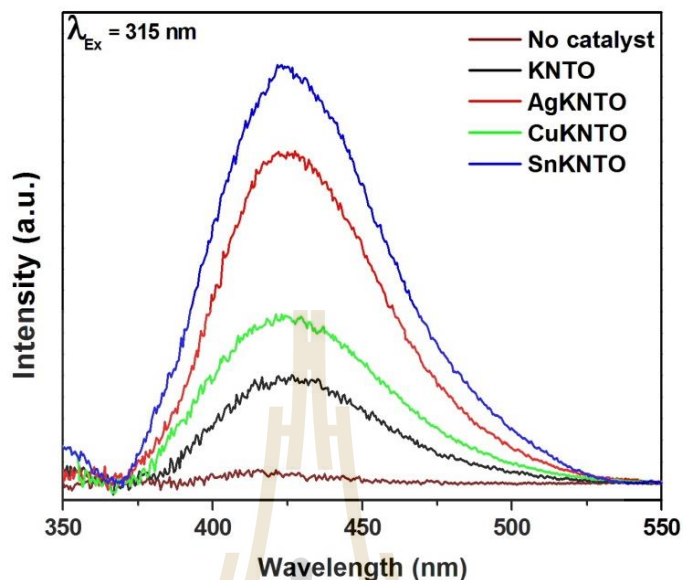


Figure 5.13 Fluorescence of TAOH with visible light irradiated KNTO, AgKNTO, CuKNTO, and SnKNTO suspensions ($\lambda_{\text{Ex}} = 315 \text{ nm}$).

It is clear that the higher photocatalytic activity of Sn^{2+} , Ag^+ , and Cu^{2+} -doped, is due to the narrower band gap energy and the stronger light absorption in visible region leading to more photoexcited electron-hole pairs and higher active species. However, the increase bandwidth of valence band and the higher surface adsorbed water (supported by TGA and O 1s XPS) also play critical roles in photocatalytic performance of SnKNTO. As mentioned above, the wider bandwidth of valence band can increased the lifetime of photogenerated electron-hole pairs separation. It is well known that photocatalysts have small band gap energy and better electron-hole pairs separation can generate more number of electron-hole pairs, leading to higher photocatalytic activity.

5.4.6 Possible photocatalytic mechanism

The detection of active species during photocatalytic reaction could give insight to the photocatalytic mechanism. In this work, isopropanol (IPA), sodium oxalate ($\text{Na}_2\text{C}_2\text{O}_4$), and benzoquinone (BQ) were used as hydroxyl radicals ($\bullet\text{OH}$), holes (h^+) and superoxide radicals ($\text{O}_2\bullet^-$) scavengers, respectively (Huang et al., 2014). The photocatalytic degradation of MB over SnKNTO in the presence of different scavengers is shown in Figure 5.14. The results show that, the percentage of MB degradation after 3 h was found to be about 31%, 45%, and 47% when IPA, $\text{Na}_2\text{C}_2\text{O}_4$, and BQ were added, respectively. Thus, hydroxyl radicals ($\bullet\text{OH}$) is the major active species for photodegradation of MB over SnKNTO under UV-Visible light irradiation. On the other hand, photogenerated holes (h^+) and superoxide radicals ($\text{O}_2\bullet^-$) are minor active species in this process.

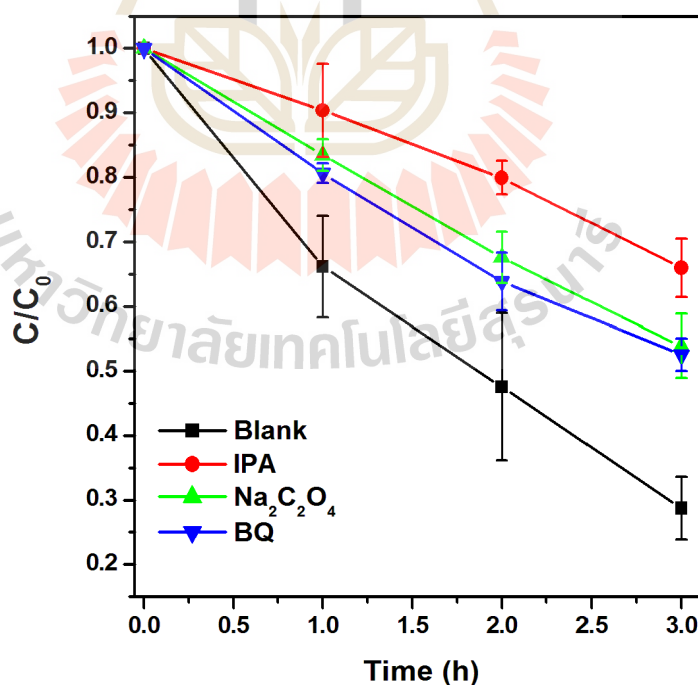


Figure 5.14 The photocatalytic degradation of MB over SnKNTO in the presence of different scavengers.

Furthermore, band position is another important factor for photocatalysis. The relationship between bottom of conduction band (E_{CB}) and band gaps (E_g) for oxide semiconductors consisting d^0 and d^{10} metal ions that was reported by Scaife as shown in the equation: (Scaife, 1980).

$$E_{CB} = 2.94 - E_g \quad [3]$$

In semiconducting oxides, valence bands are usually formed with O $2p$ orbitals. The potential difference in the conduction bands is mainly attributed from the difference of band gaps. We speculate that the same case takes place in KNTO because the compound contain $(\text{Nb}^{5+}/\text{Te}^{6+})\text{O}_6$ octahedra. From the observed parameters, it appears that KNTO has E_g of 3.38 eV, and the valence band is at 2.94 V, consisting of only O $2p$. Therefore, the conduction band will be at -0.44 V, which is contributed by Nb and Te. The potential of the conduction band minimum of SnKNTO should be similar to that of KNTO because they have the same pyrochlore structure and main components (Nb/Te) (Hosogi et al., 2008). The presence of Sn $5s$ orbitals form new valence bands at a more negative level than the O $2p$ orbitals. Consequently, the band gap of SnKNO was 0.87 eV narrower than that of KNTO (Figure 5.15). Thus, the CB potential of SnKNO is more negative to the redox potentials of $\text{O}_2/\text{O}_2^{\bullet-}$ (-0.33V vs. NHE; at pH=7), and the photogenerated electrons can reduce O_2 to generate $\text{O}_2^{\bullet-}$. On the other hand, the VB potential of SnKNTO is more positive than the redox potentials of $\text{OH}^-/\bullet\text{OH}$ (+1.9V vs. NHE; at pH=7) but more negative than that of $\bullet\text{OH}/\text{H}_2\text{O}$ (+2.73V vs. NHE; at pH=7), indicating that the photogenerated holes in the CB of SnKNTO can oxidize OH^- to form $\bullet\text{OH}$ radicals but cannot oxidize H_2O to produce $\bullet\text{OH}$ radicals (Al-Fahdi et al., 2019; Ma et al., 2018; Wardman, 1989; Wood, 1988).

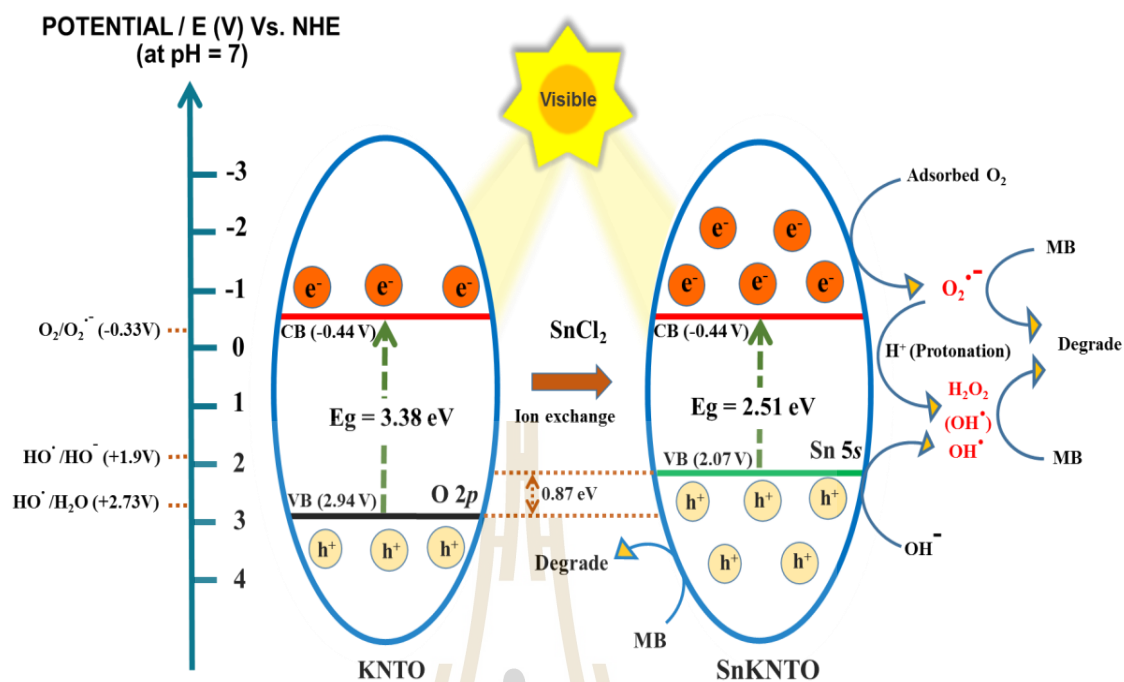


Figure 5.15 The proposed band potential and mechanism of MB photodegradation over SnKNTO photocatalyst.

Accordingly, the photocatalytic mechanism of SnKNTO is proposed. As shown in Figure 5.15, formation of Sn 5s level on the top of valence band effectively lifts the top of valence band and cause a red-shift on the optical absorption edge. In this case, more electrons and holes are created at conduction and valence band of SnKNTO, respectively. Therefore, photocatalytic performance of SnKNTO is improved when compare with KNTO. The MB photodegradation process is shown in the following reactions: (Lin et al., 2014; Reza et al., 2016; Xia et al., 2018)





The first step is the excitation of electrons from valence band to conduction band, leaving holes in the valence band. In the valence band, the separated h^+ migrates to the surface and is trapped by surface-adsorbed hydroxyl to produce hydroxyl radical ($\cdot OH$). On the other hand, O_2 acts as the electron acceptor to trap the photoexcited electrons, thus leading to $O_2^{\bullet-}$ formation. Moreover, $O_2^{\bullet-}$ can be protonated to yield hydroperoxyl radical ($\cdot HO_2$), form hydrogen peroxide (H_2O_2), and finally to hydroxyl radical ($\cdot OH$) active species (Lin et al., 2014; Reza et al., 2016; Xia et al., 2018). Finally, the produced active species ($\cdot OH$ and $O_2^{\bullet-}$) react with MB to degrade them. In addition, MB are also directly oxidized by h^+ at the valence band of SnKNTO (Guo et al., 2016; Lin et al., 2014; Reza et al., 2016).

5.5 Conclusion

$KNbTeO_6$ parent and Ag^+ , Cu^{2+} and Sn^{2+} -doped $KNbTeO_6$ compounds have been successfully prepared by solid state and facile ion exchange method, respectively. The incorporation of Ag, Cu, and Sn into the $KNbTeO_6$ lattice after ion exchange was investigated by X-ray photoelectron spectroscopy (XPS) and energy dispersive X-ray spectroscopy (EDS) techniques. The red-shift of the optical

absorption edge of ion exchanged compounds are attributed to the shift of valence band caused by the hybridization of Ag 4*d*, Cu 3*d*, and Sn 5*s* states with O 2*p* states at the top of the valence band. As a result, they exhibit higher photocatalytic performance than pure KNbTeO₆ under UV-Visible light irradiation. In this research, SnKNTO compound displays the highest efficiency. It is due to narrower band gap energy, stronger light absorption in visible region, a lot of surface adsorbed oxygen species, and wider valence band. The mechanism of Methylene blue photodegradation was studied by using quenchers in the presence of Sn²⁺-doped KNbTeO₆ as a photocatalyst. It is found that the hydroxyl radicals ($\bullet\text{OH}$) is major active species, while, photogenerated holes (h^+) and superoxide radicals ($\text{O}_2\bullet^-$) are minor active species for this photodegradation process.

5.6 Reference

- Al-Fahdi, T., Al Marzouqi, F., Kuvarega, A. T., Mamba, B. B., Al Kindy, S. M., Kim, Y., and Selvaraj, R. (2019). Visible light active CdS@TiO₂ core-shell nanostructures for the photodegradation of chlorophenols. **Journal of Photochemistry and Photobiology A: Chemistry**. 374: 75-83.
- Ansari, S. A., Khan, M. M., Ansari, M. O., and Cho, M. H. (2016). Nitrogen-doped titanium dioxide (N-doped TiO₂) for visible light photocatalysis. **New Journal of Chemistry**. 40(4): 3000-3009.
- Atuchin, V., Kesler, V., Meng, G., and Lin, Z. (2012). The electronic structure of RbTiOPO₄ and the effects of the A-site cation substitution in KTiOPO₄-family crystals. **Journal of Physics: Condensed Matter**. 24(40): 405503.

- Chen, C.-C., Wang, F.-H., Chang, S.-C., and Yang, C.-F. (2018). Using oxygen plasma pretreatment to enhance the properties of F-doped ZnO films prepared on polyimide substrates. **Materials**. 11(9): 1501.
- Fu, H., Pan, C., Yao, W., and Zhu, Y. (2005). Visible-light-induced degradation of rhodamine B by nanosized Bi₂WO₆. **The Journal of Physical Chemistry B**. 109(47): 22432-22439.
- Guje, R., Gundeboina, R., Kadari, R., Sreenu, K., Reddy, C., Malathi, M., and Vithal, M. (2016). Synthesis, characterization and photocatalytic activity studies of tellurium containing defect pyrochlores, MSn_{0.5}Te_{1.5}O₆ (M= K, Ag, Cu_{0.5} and Sn_{0.5}). **Indian Journal of Chemistry**. 55A: 1174-1181.
- Guje, R., Gundeboina, R., Reddy, J. R., Veldurthi, N. K., Kurra, S., and Vithal, M. (2016). Synthesis, Characterization and Photocatalytic Activity of Ag⁺ and Sn²⁺-Doped KTi_{0.5}Te_{1.5}O₆. **Photochemistry and photobiology**. 92(2): 223-230.
- Guje, R., Ravi, G., Palla, S., Rao, K. N., and Vithal, M. (2015). Synthesis, characterization, photocatalytic and conductivity studies of defect pyrochlore KM_{0.33}Te_{1.67}O₆ (M= Al, Cr and Fe). **Materials Science and Engineering: B**. 198: 1-9.
- Guje, R., Shrujana, P., Veldurthi, N. K., Gundeboina, R., Kappera, N. R., and Muga, V. (2015). Synthesis, characterisation and photocatalytic activity of Ag⁺-and Sn²⁺-substituted KSbTeO₆. **Chemical Papers**. 69(2): 269-278.
- Guo, M., He, Q., Wang, A., Wang, W., and Fu, Z. (2016). A novel, simple and green way to fabricate BiVO₄ with excellent photocatalytic activity and its methylene blue decomposition mechanism. **Crystals**. 6(7): 81.
- Harb, M., Masih, D., and Takanabe, K. (2014). Screened coulomb hybrid DFT

- investigation of band gap and optical absorption predictions of CuVO_3 , CuNbO_3 and $\text{Cu}_5\text{Ta}_{11}\text{O}_{30}$ materials. **Physical Chemistry Chemical Physics**. 16(34): 18198-18204.
- Hosogi, Y., Shimodaira, Y., Kato, H., Kobayashi, H., and Kudo, A. (2008). Role of Sn^{2+} in the band structure of SnM_2O_6 and $\text{Sn}_2\text{M}_2\text{O}_7$ (M= Nb and Ta) and their photocatalytic properties. **Chemistry of Materials**. 20(4): 1299-1307.
- Huang, H., Liu, K., Chen, K., Zhang, Y., Zhang, Y., and Wang, S. (2014). Ce and F comodification on the crystal structure and enhanced photocatalytic activity of Bi_2WO_6 photocatalyst under visible light irradiation. **The Journal of Physical Chemistry C**. 118(26): 14379-14387.
- Jitta, R. R., Guje, R., Veldurthi, N. K., Prathapuram, S., Velchuri, R., and Muga, V. (2015). Preparation, characterization and photocatalytic studies of N, Sn-doped defect pyrochlore oxide $\text{KTi}_{0.5}\text{W}_{1.5}\text{O}_6$. **Journal of Alloys and Compounds**. 618: 815-823.
- Jitta, R. R., Gundeboina, R., Veldurthi, N. K., Guje, R., and Muga, V. (2015). Defect pyrochlore oxides: as photocatalyst materials for environmental and energy applications-a review. **Journal of Chemical Technology & Biotechnology**. 90(11): 1937-1948.
- Jun, D., Qi, W., ZHONG, S., Xin, G., Jiao, L., Haizhi, G., Wenlong, Z., hailong, P., and Jianguo, Z. (2015). Effect of hydroxyl groups on hydrophilic and photocatalytic activities of rare earth doped titanium dioxide thin films. **Journal of Rare Earths**. 33(2): 148-153.
- Kruczek, M., Talik, E., and Kania, A. (2006). Electronic structure of AgNbO_3 and NaNbO_3 studied by X-ray photoelectron spectroscopy. **Solid State Communications**.

137(9): 469-473.

Kurra, S., Venkataswamy, P., Ravi, G., Sudhakar Reddy, C., Jaganmohan Reddy, B., and Vithal, M. (2019). Enhancement of Photocatalytic Activity of Sodium Bismuth Titanate by Doping with Copper, Silver, and Tin Ions. **Zeitschrift für Anorganische und Allgemeine Chemie**. 645: 529–536.

Lee, K., Kim, J., Mok, I.-S., Na, H., Ko, D.-H., Sohn, H., Lee, S., and Sinclair, R. (2014). RESET-first unipolar resistance switching behavior in annealed Nb₂O₅ films. **Thin Solid Films**. 558: 423-429.

Li, J., Ni, G., Han, Y., and Ma, Y. (2017). Synthesis of La doped Bi₂WO₆ nanosheets with high visible light photocatalytic activity. **Journal of Materials Science: Materials in Electronics**. 28(14): 10148-10157.

Lin, H., Ye, H., Chen, S., and Chen, Y. (2014). One-pot hydrothermal synthesis of BiPO₄/BiVO₄ with enhanced visible-light photocatalytic activities for methylene blue degradation. **RSC Advances**. 4(21): 10968-10974.

Lin, X. P., Huang, F. Q., Wang, W. D., and Zhang, K. L. (2006). A novel photocatalyst BiSbO₄ for degradation of methylene blue. **Applied Catalysis A: General**. 307(2): 257-262.

Liu, X., Que, W., Xing, Y., Yang, Y., Yin, X., and Shao, J. (2016). New architecture of a petal-shaped Nb₂O₅ nanosheet film on FTO glass for high photocatalytic activity. **RSC Advances**. 6(12): 9581-9588.

Ma, J., Wang, F., and Mostafavi, M. (2018). Ultrafast Chemistry of Water Radical Cation, H₂O^{•+}, in Aqueous Solutions. **Molecules**. 23(2): 244.

Mahmood, A., Ramay, S. M., Rafique, H. M., Al-Zaghayer, Y., and Khan, S. U.-D. (2014). First-principles study of electronic, optical and thermoelectric

- properties in cubic perovskite materials AgMO_3 ($M = \text{V, Nb, Ta}$). **Modern Physics Letters B**. 28(10): 1450077.
- Mekki, A., Khattak, G., and Wenger, L. (2005). Structural and magnetic properties of $\text{MoO}_3\text{-TeO}_2$ glasses. **Journal of Non-Crystalline Solids**. 351(30-32): 2493-2500.
- Moggia, J., Milt, V. G., Ulla, M., and Cornaglia, L. M. (2003). Surface characterization of Co, K/La₂O₃ catalysts used for the catalytic combustion of diesel soot. **Surface and Interface Analysis**. 35(2): 216-225.
- Molla, A., Sahu, M., and Hussain, S. (2016). Synthesis of tunable band gap semiconductor nickel sulphide nanoparticles: Rapid and round the clock degradation of organic dyes. **Scientific Reports**. 6: 26034.
- Morales, A. E., Mora, E. S., and Pal, U. (2007). Use of diffuse reflectance spectroscopy for optical characterization of un-supported nanostructures. **Revista Mexicana de Física**. 53(5): 18-22.
- Botana, A. and Norman, M. (2017). Electronic structure of CuTeO_4 and its relationship to cuprates. **Physical Review B**. 95: 115123.
- Qamar, M., Abdalwadoud, M., Ahmed, M., Azad, A.-M., Merzougui, B., Bukola, S., Yamani, Z., and Siddiqui, M. (2015). Single-Pot Synthesis of $\langle 001 \rangle$ -Faceted N-Doped Nb_2O_5 /Reduced Graphene Oxide Nanocomposite for Efficient Photoelectrochemical Water Splitting. **ACS Applied Materials & Interfaces**. 7(32): 17954-17962.
- Ravi, G., Palla, S., Veldurthi, N. K., Reddy, J., Padmasri, H., and Vithal, M. (2014). Solar water-splitting with the defect pyrochlore type of oxides $\text{KFe}_{0.33}\text{W}_{1.67}\text{O}_6$ and $\text{Sn}_{0.5}\text{Fe}_{0.33}\text{W}_{1.67}\text{O}_6 \cdot x\text{H}_2\text{O}$. **International Journal of Hydrogen Energy**.

39(28): 15352-15361.

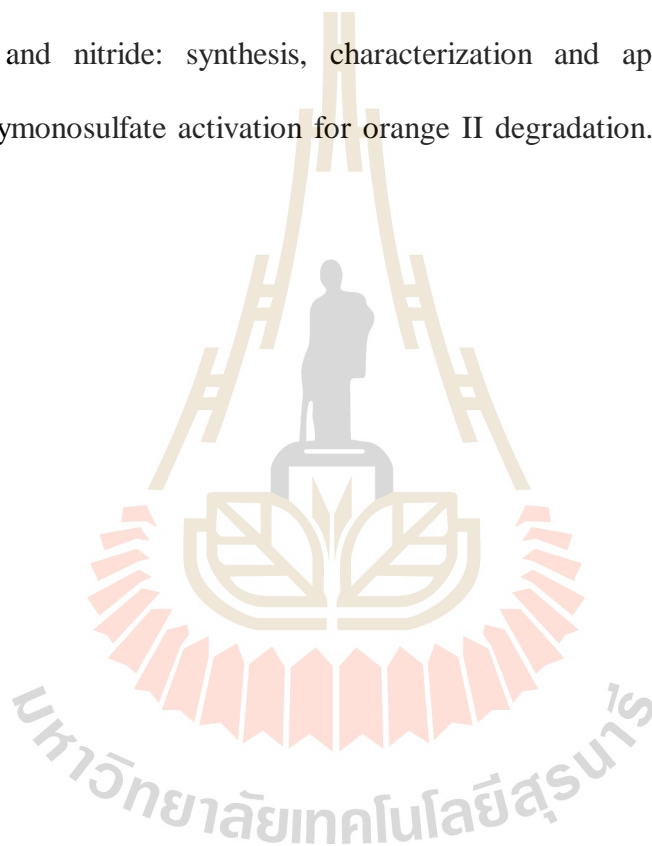
- Ravi, G., Veldurthi, N. K., Prasad, M. D., Muniratnam, N., Prasad, G., and Vithal, M. (2013). Preparation, optical, and photocatalytic studies of defect pyrochlores: $\text{KCr}_{0.33}\text{W}_{1.67}\text{O}_6$ and $\text{A}_x\text{Cr}_{0.33}\text{W}_{1.67}\text{O}_6 \cdot n\text{H}_2\text{O}$. **Journal of Nanoparticle Research**. 15(9): 1939.
- Reza, K. M., Kurny, A., and Gulshan, F. (2016). Photocatalytic degradation of methylene blue by magnetite H_2O_2 + UV Process. **International Journal of Environmental Science and Development**. 7(5): 325.
- Sathiya, M., Ramesha, K., Rousse, G., Foix, D., Gonbeau, D., Guruprakash, K., Prakash, A. S., Doublet, M. L., and Tarascon, J.-M. (2013). $\text{Li}_4\text{NiTeO}_6$ as a positive electrode for Li-ion batteries. **Chemical Communications**. 49(97): 11376-11378.
- Scaife, D. J. (1980). Oxide semiconductors in photoelectrochemical conversion of solar energy. **Solar Energy**. 25(1): 41-54.
- Shannon, R. D. (1976). Revised effective ionic radii and systematic studies of interatomic distances in halides and chalcogenides. **Acta Crystallographica Section A**. 32(5): 751-767.
- Tian, C., Zhang, Q., Wu, A., Jiang, M., Liang, Z., Jiang, B., and Fu, H. (2012). Cost-effective large-scale synthesis of ZnO photocatalyst with excellent performance for dye photodegradation. **Chemical Communications**. 48(23): 2858-2860.
- Uma, S., Singh, J., and Thakral, V. (2009). Facile room temperature ion-exchange synthesis of Sn^{2+} incorporated pyrochlore-type oxides and their photocatalytic activities. **Inorganic Chemistry**. 48(24): 11624-11630.

- Veldurthi, N. K., Ravi, G., Reddy, J. R., Palla, S., Muniratnam, N. R., Prasad, G., and Vithal, M. (2014). Facile Ion-Exchange Synthesis and Visible Light Photocatalytic Studies of Cu^{2+} , Sn^{2+} , and Ag^+ -Substituted $\text{LiMg}_{0.5}\text{Ti}_{0.5}\text{O}_2$. **Journal of the American Ceramic Society**. 97(6): 1829-1836.
- Wang, H., Dou, K., Teoh, W. Y., Zhan, Y., Hung, T. F., Zhang, F., Xu, J., Zhang, R., and Rogach, A. L. (2013). Engineering of Facets, Band Structure, and Gas-Sensing Properties of Hierarchical Sn^{2+} -Doped SnO_2 Nanostructures. **Advanced Functional Materials**. 23(38): 4847-4853.
- Wardman, P. (1989). Reduction potentials of one-electron couples involving free radicals in aqueous solution. **Journal of Physical and Chemical Reference Data**. 18(4): 1637-1755.
- Weber, A. S., Grady, A. M., and Koodali, R. T. (2012). Lanthanide modified semiconductor photocatalysts. **Catalysis Science & Technology**. 2(4): 683-693.
- Wood, P. M. (1988). The potential diagram for oxygen at pH 7. **Biochemical Journal**. 253(1): 287-289.
- Wu, T., Lin, T., Zhao, J., Hidaka, H., and Serpone, N. (1999). TiO_2 -assisted photodegradation of dyes. 9. Photooxidation of a squarylium cyanine dye in aqueous dispersions under visible light irradiation. **Environmental Science & Technology**. 33(9): 1379-1387.
- Xia, Y., He, Z., Lu, Y., Tang, B., Sun, S., Su, J., and Li, X. (2018). Fabrication and photocatalytic property of magnetic $\text{SrTiO}_3/\text{NiFe}_2\text{O}_4$ heterojunction nanocomposites. **RSC Advances**. 8(10): 5441-5450.
- Xu, D., Fan, D., and Shen, W. (2013). Catalyst-free direct vapor-phase growth of

$Zn_{1-x}Cu_xO$ micro-cross structures and their optical properties. **Nanoscale Research Letters**. 8(1): 46.

Zeng, J., Wang, H., Zhang, Y., Zhu, M. K., and Yan, H. (2007). Hydrothermal synthesis and photocatalytic properties of pyrochlore $La_2Sn_2O_7$ nanocubes. **The Journal of Physical Chemistry C**. 111(32): 11879-11887.

Zhu, K., Jin, C., Klencsár, Z., Ganeshraja, A., and Wang, J. (2017). Cobalt-iron oxide, alloy and nitride: synthesis, characterization and application in catalytic peroxymonosulfate activation for orange II degradation. **Catalysts**. 7(5): 138



CHAPTER VI

CONCLUSIONS

In this thesis, many tellurium containing defect pyrochlores oxides have been synthesized and investigated in an attempt to study their electronic and photocatalytic properties.

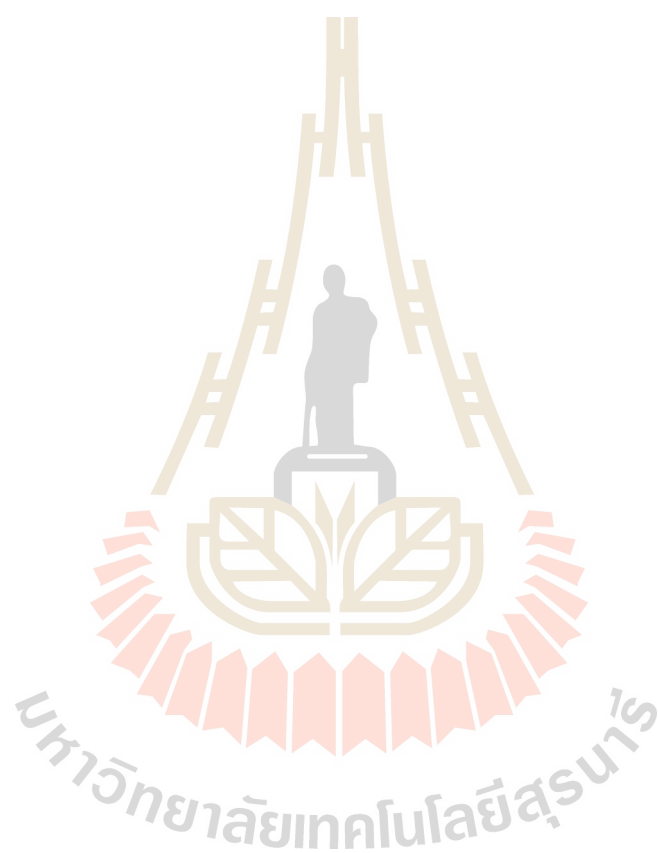
$\text{Cs}(\text{M},\text{Te})_2\text{O}_6$ were recently reported as a mixed valence pyrochlores which show *n*-type semiconducting behavior due to $\text{Te}^{4+}/\text{Te}^{6+}$ mixed valency. It was reported that smaller M cations reduce cell parameters which increases the conductivity. However, the role of Cs in these compounds is unclear and the mechanism of conduction had not been proved experimentally. In this work, $\text{CsAl}_{0.33}\text{Te}_{1.67}\text{O}_6$ is chosen to study the effects of cation at Cs position by Rb and K substitutions. Despite the smaller cell parameters of the compounds when Cs is replaced with smaller Rb and K, the conductivities at room temperature are decreased. UV-Vis spectra, XPS spectra at valence band region and activation energies of conduction are used to propose the band structure diagrams which suggest that the conductivities were determined by the energy difference between the defect levels originated from Te^{4+} and the bottom of conduction band.

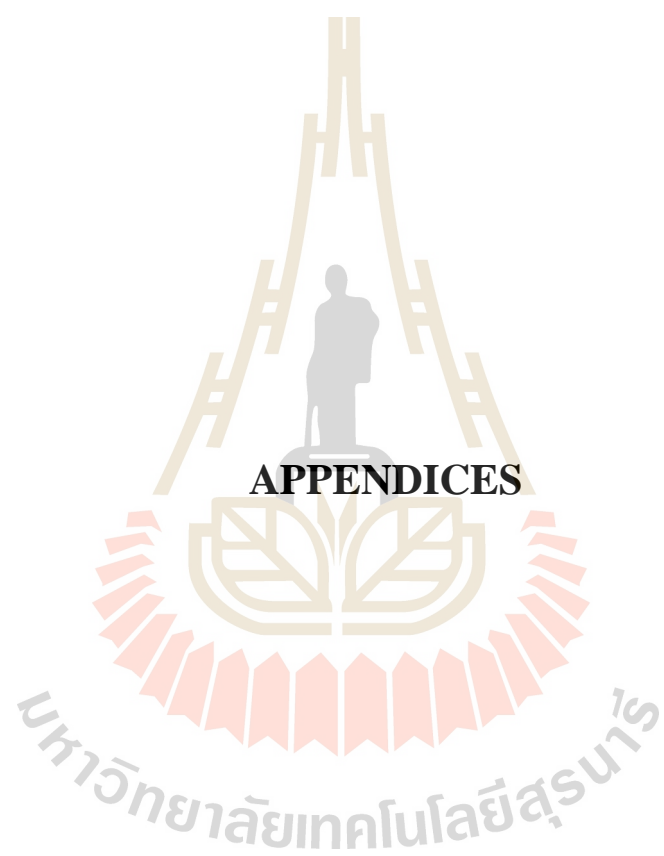
On the other hand, $\text{CsMn}_x\text{Te}_{2-x}\text{O}_6$ with $x = 0.05 - 0.43$ are chosen to investigate the effects of M metal on the structure and electronic properties of $\text{Cs}(\text{M}, \text{Te})_2\text{O}_6$. It is found that substituting Te in CsTe_2O_6 with as small as 2.5% Mn changes the structure from rhombohedral to cubic symmetry. Based on results from

XANES and XPS the compounds can be presented as $\text{Cs}^{1+}(\text{Mn}^{3+})_x(\text{Te}^{4+})_{0.5-(3x/2)}(\text{Te}^{6+})_{1.5+(x/2)}\text{O}_6$ for $x \leq 0.33$ and $\text{Cs}^{1+}(\text{Mn}^{3+/4+})_x(\text{Te}^{6+})_{2-x}\text{O}_{6-\delta}$ for $x > 0.33$. The switch between the two schemes, at $x = 0.33$, results in a sudden change in the cell parameter trend and the activation energy of conduction. Based on the proposed band diagram, the Te 5s states overlap with Mn 3d-O 2p states and become part of the valence band in compounds with $x < 0.33$. Compounds with $x > 0.33$ contain small amount of oxygen vacancies whose states contribute to the top of the valence band. Nevertheless, all compounds are considered intrinsic semiconductors. Based on the investigation, the unit cell parameters are strongly correlated with the energy levels of Te 5s states. Despite having high Te^{4+} content in the lattice, they are stabilized by the large cell parameters and the compounds do not exhibit n-type character.

Many $\text{ABB}'\text{O}_6$ defect pyrochlores are promising candidates for photocatalytic properties and have been widely developed for photocatalysts application. It is well known that ion exchange with other cations for K^+ in $\text{KBB}'\text{O}_6$ results in a narrow band gap which leads to high photocatalytic activity under visible light. However, photocatalytic properties of tellurium containing defect pyrochlores are not widely investigated. Therefore, this thesis aims to study the modification of band gap energy and its effects on the photocatalytic activity of KNbTeO_6 defect pyrochlore oxides. Ag^+ , Cu^{2+} , and Sn^{2+} are substituted in K site of KNbTeO_6 compounds to modify the band gap energy. The electronic structure of all compounds was proposed based on the X-ray photoelectron spectroscopy at valence band region and UV-Vis absorption spectra. The contribution of Ag 4d, Cu 3d, and Sn 5s states in doped samples results in a shift of valence band maximum, which reduces the band gap energy leading to more active species generation and reduce

the band gap energy leading to more active species generation and consequently improved higher photocatalytic activity.





APPENDIX A

XPS ANALYSIS, X-RAY DIFFRACTION, AND RESISTIVITY

A1 XPS calculation of Te^{4+} and Te^{6+} contents

To obtain the Te^{4+} and Te^{6+} contents, the fitting analysis of Te $3d_{5/2}$ XPS were performed and the obtained peak areas of both peaks were used for the calculation as follows:

$$\text{Te}^{4+} \text{ content} = \left[\frac{(\text{peak area of Te(IV)})}{(\text{peak area of Te(IV)}) + (\text{peak area of Te(VI)})} \right] \times \text{Total Te contents}$$

$$\text{Te}^{6+} \text{ content} = (\text{Total Te content}) - (\text{Te}^{4+} \text{ content})$$

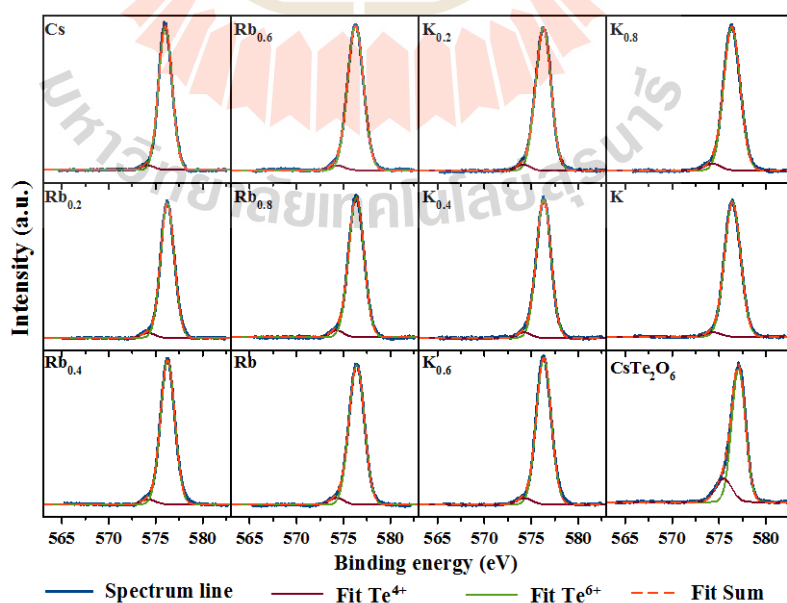


Figure A1 Te $3d_{5/2}$ XPD fitting of $\text{Cs}_{1-x}\text{A}_x\text{Al}_{0.33}\text{Te}_{1.67}\text{O}_6$ (A= Rb and K) and CsTe_2O_6 .

A2 X-ray diffraction of $\text{AAl}_x\text{Te}_{2-x}\text{O}_6$ (A = Cs, Rb, and K).

X-ray diffraction (XRD) was used to investigate the phase purity of $\text{AAl}_x\text{Te}_{2-x}\text{O}_6$ (A = Cs, Rb, and K) with varied Al contents. The results indicate that only samples with $x = 0.33$ can be indexed as AB_2O_6 cubic defect pyrochlore structure without impurity.

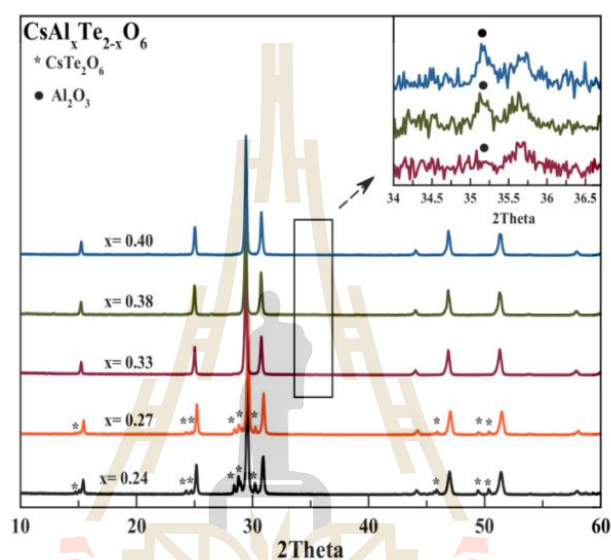


Figure A2 XRD pattern of $\text{CsAl}_x\text{Te}_{2-x}\text{O}_6$.

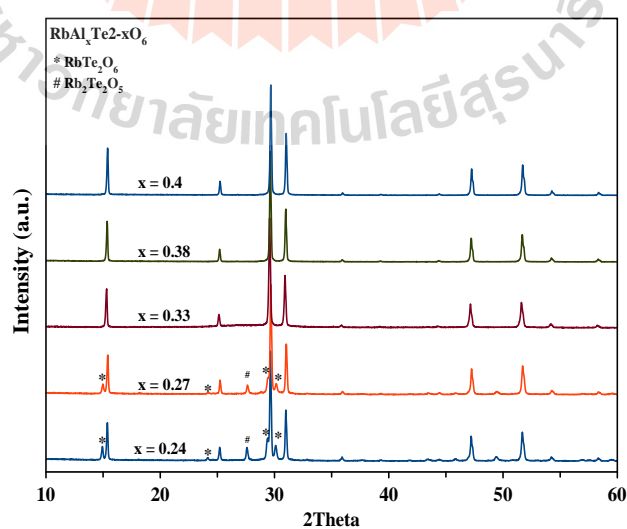


Figure A3 XRD pattern of $\text{RbAl}_x\text{Te}_{2-x}\text{O}_6$

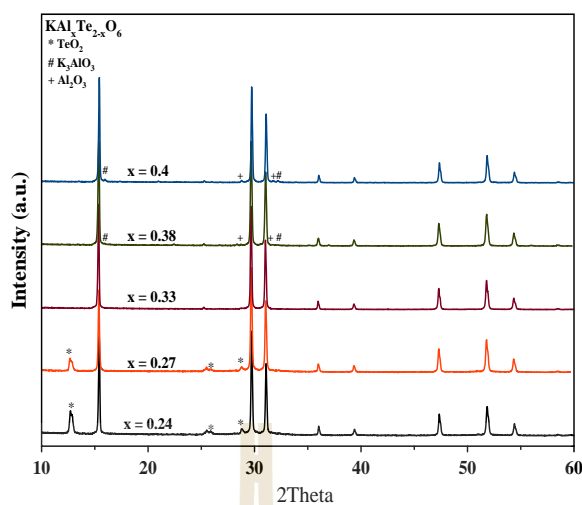


Figure A4 XRD pattern of $\text{KAl}_x\text{Te}_{2-x}\text{O}_6$.

A3 Resistivity of $\text{AAI}_x\text{Te}_{2-x}\text{O}_6$ (A = Cs, Rb, and K)

Resistivity at room temperature of the $\text{AAI}_x\text{Te}_{2-x}\text{O}_6$ (A = Cs, Rb, and K) were measured by four-probe method. Note that only $\text{KAl}_x\text{Te}_{2-x}\text{O}_6$ sample with $x = 0.33$ exhibit measurable resistivity, the resistivity of other samples are too high to be measured with the current technique.

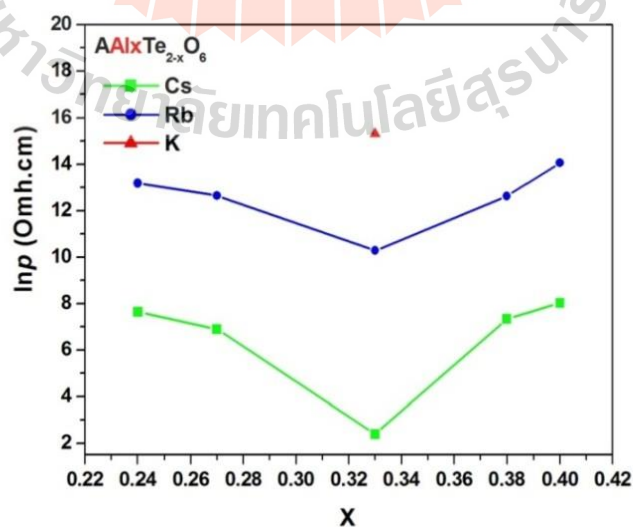


Figure A5 Resistivity at room temperature of the $\text{AAI}_x\text{Te}_{2-x}\text{O}_6$ (A = Cs, Rb, and K).

APPENDIX B

XPS AND TEM ANALYSIS OF $\text{CsMn}_x\text{Te}_{2-x}\text{O}_6$

B1 XPS of Mn 2p and Te 3d

The Mn 2p and Te 3d XPS were recorded to support XANES results. It is known that Mn 2p_{3/2} peak of Mn³⁺ (641.2-641.7 eV) and Mn⁴⁺ (642.1-642.6 eV) are close to each other that the interpretation of Mn states based on the binding energies is difficult. Thus, the spin-orbital splitting of Mn 2p_{3/2} and Mn 2p_{1/2} was used to identify the oxidation states of manganese ions in the samples. As displayed in Figure B1, such an energy separation between Mn 2p_{1/2} and Mn 2p_{3/2} (ΔE of Mn 2p) are about 11.99 - 12.03 eV for samples with $x \leq 0.33$ which indicates Mn³⁺. For samples with $x > 0.33$, on the other hand, ΔE of Mn 2p decrease to 11.80-11.81 eV suggesting mixture of Mn³⁺ and Mn⁴⁺. The Mn 2p XPS results agree well with those of previously obtained XANES spectra. The observed intensities also agree with the nominal compositions. The Te 3d spectra (Figure B2) obviously show asymmetric peaks for samples with $x = 0.15 - 0.30$. Thus, they are fitted into two components, one belongs to Te⁴⁺ and the other Te⁶⁺. On the other hand, the samples with $x > 0.30$ show symmetric peaks which are fitted into only Te⁶⁺. The fitting results are summarized in Table B1

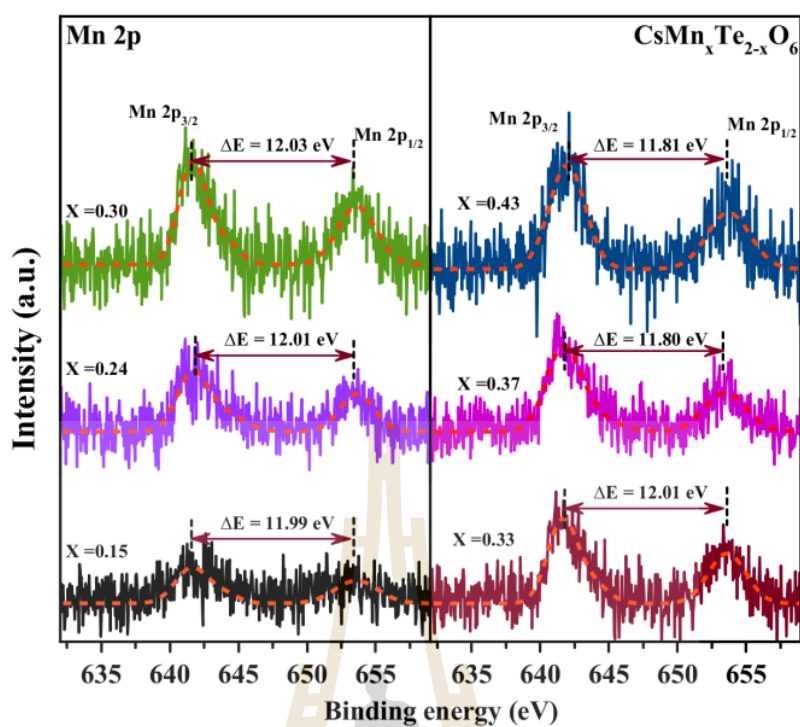


Figure B1 Mn $2p$ XPS spectra of $\text{CsMn}_x\text{Te}_{2-x}\text{O}_6$.

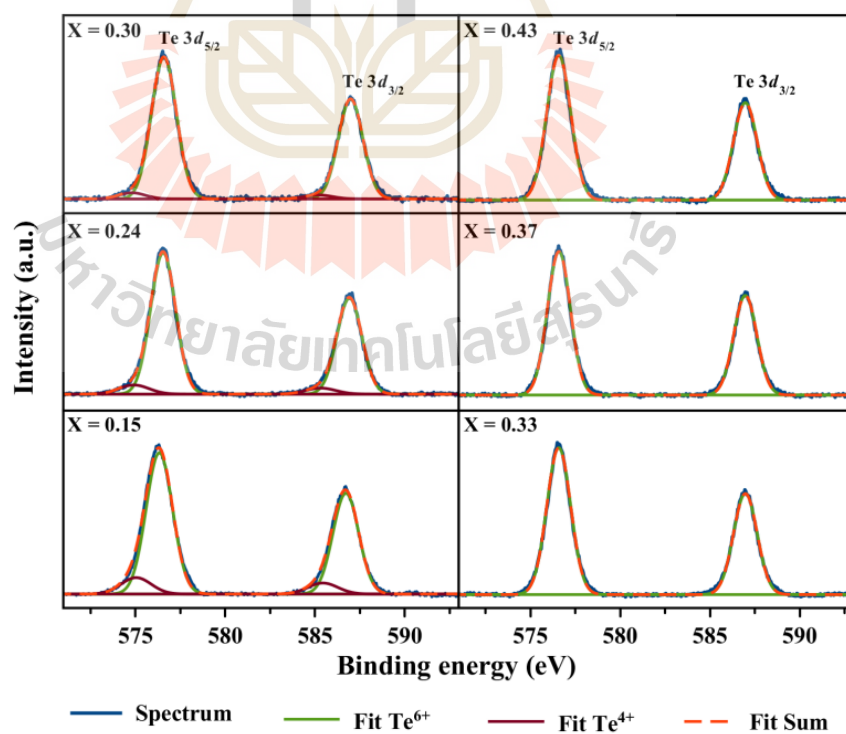
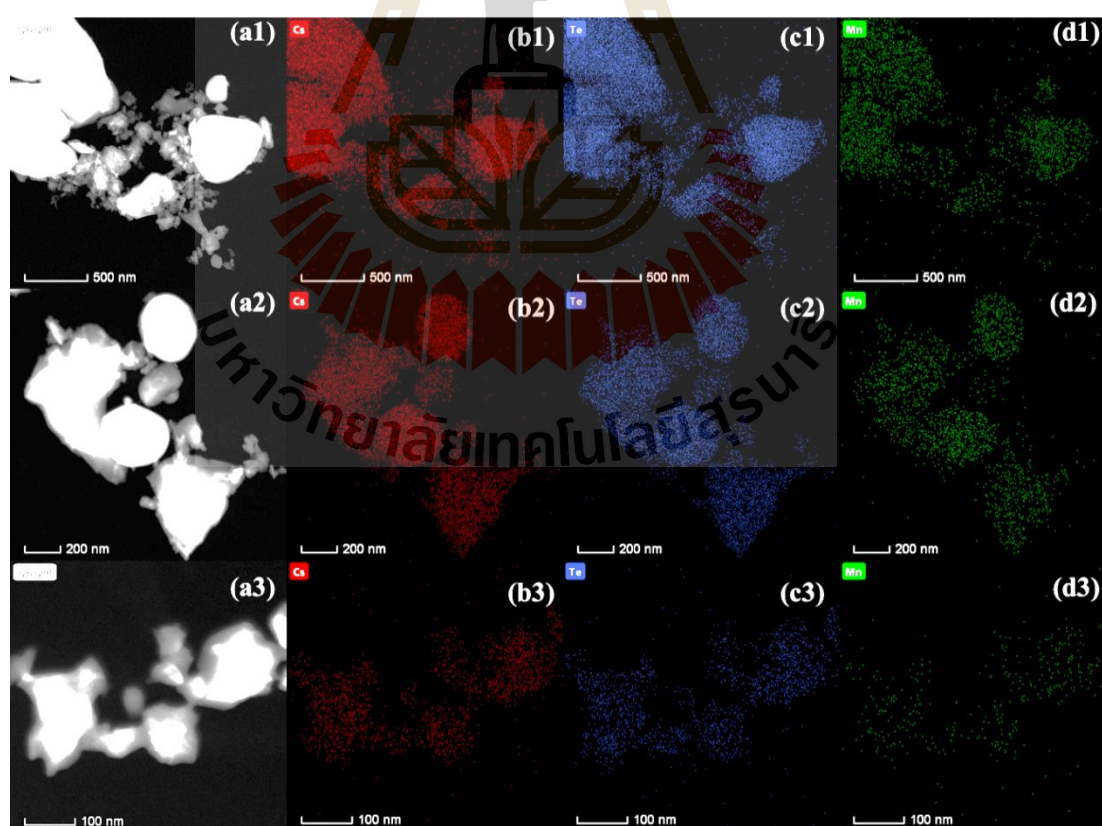


Figure B2 Te $3d$ XPS spectra of $\text{CsMn}_x\text{Te}_{2-x}\text{O}_6$.

Table B1 Summary of Te components based on Te $3d_{5/2}$ XPS spectra.

Mn content	Te ⁶⁺		Te ⁴⁺		Te Content Te ⁶⁺ : Te ⁴⁺
	B.E. (eV)	FWHM (eV)	B.E. (eV)	FWHM (eV)	
0.15	576.34	1.73	575.04	1.97	1.63 : 0.22
0.24	576.55	1.63	574.92	1.98	1.63 : 0.13
0.30	576.59	1.64	574.80	1.75	1.62 : 0.08
0.33	576.58	1.56	-	-	1.67 : 0.00
0.37	576.59	1.51	-	-	1.63 : 0.00
0.43	576.58	1.57	-	-	1.57 : 0.00

B2 TEM analysis in a different area of CsMn_{0.43}Te_{1.57}O₆**Figure B3** TEM analysis in a different area of CsMn_{0.43}Te_{1.57}O₆. (a) STEM imaged and (b-d) the corresponding Cs, Te, and Mn elemental mappings, respectively.

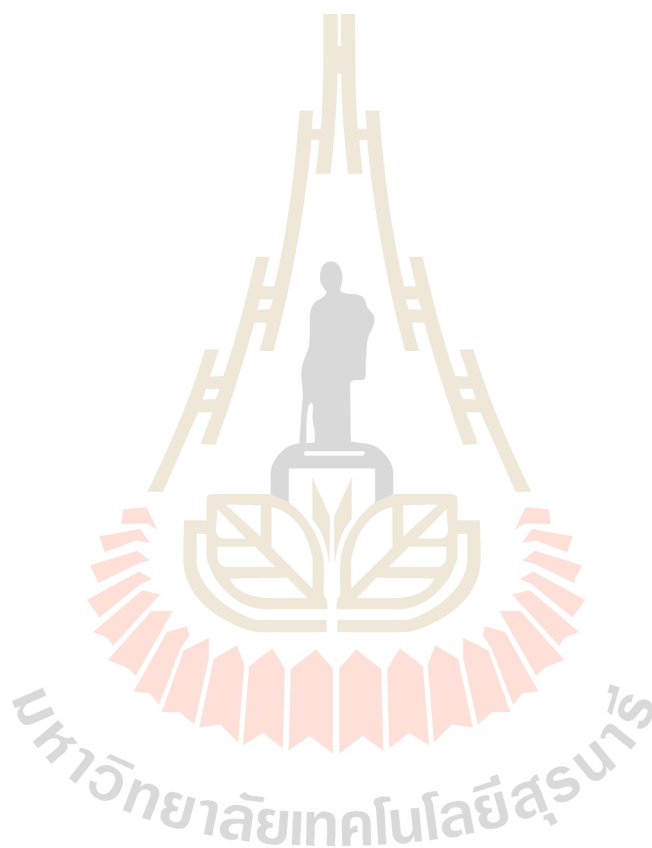
From Cs 3d XPS result, samples with $x > 0.33$ display a shoulder at a slightly higher binding energy which may be characteristic of small Cs metallic cluster. TEM and the energy dispersive X-ray spectroscopy (EDS) elemental mapping were used to investigate the small Cs metallic cluster. According to the mapping of $\text{CsMn}_{0.43}\text{Te}_{1.57}\text{O}_6$, all elements are homogeneously distributed in the samples. This indicates that the Cs metallic clusters are not present in samples with $x > 0.33$.

References

- Deng, J., Farid, M. A., Zhang, M., Yang, A., Zhang, H., Zhang, H., and Sun, J. (2017). Enhancement of Ferroelectricity for Orthorhombic $(\text{Tb}_{0.861}\text{Mn}_{0.121})\text{MnO}_{3-\delta}$ by Copper Doping. **Inorganic Chemistry**. 56(6): 3475-3482.
- Heredia, A., García, M. Q., Mazariego, J. P., and Escamilla, R. (2010). X-ray diffraction and Raman spectroscopy on $\text{Gd}_2(\text{Ti}_{2-y}\text{Tey})\text{O}_7$ prepared at high pressure and high temperature. **Journal of Alloys and Compounds**. 504(2): 446-451.
- Luo, X., Lee, W.-T., Xing, G., Bao, N., Yonis, A., Chu, D., Lee, J., Ding, J., Li, S., and Yi, J. (2014). Ferromagnetic ordering in Mn-doped ZnO nanoparticles. **Nanoscale Research Letters**. 9(1): 625.
- Oku, M., Hirokawa, K., and Ikeda, S. (1975). X-ray photoelectron spectroscopy of manganese-oxygen systems. **Journal of Electron Spectroscopy and Related Phenomena**. 7(5): 465-473.
- Sartz, W. E., Wynne, K. J., and Hercules, D. M. (1971). X-ray photoelectron spectroscopic

investigation of Group VIA elements. **Analytical Chemistry**. 43(13): 1884-1887.

Sathiya, M., Ramesha, K., Rouse, G., Foix, D., Gonbeau, D., Guruprakash, K., Prakash, A. S., Doublet, M. L., and Tarascon, J.-M. (2013). $\text{Li}_4\text{NiTeO}_6$ as a positive electrode for Li-ion batteries. **Chemical Communications**. 49(97): 11376-11378.



APPENDIX C

XANES SPECTRA, PHOTOCATALYTIC TEST, AND HYDROXYL RADICAL GENERATION

C1 XANES spectra of Nb and Te L_3 -edge

Nb and Te L_3 -edge spectra were carried out to support the chemical state of Nb and Te species in the catalysts from XPS results. Figure C1 shows the XANES spectra at the Nb and Te L_3 -edge of KNTO, AgKNTO, CuKNTO, and SnKNTO with comparison to standard materials with different oxidation states. From the Nb and Te L_3 -edge XANES spectra, the absorption edge matches that of the Nb_2O_5 and KTTO (KTaTeO_6 ; Te^{6+}) standard. This result indicates that the valency of Nb and Te in these catalysts is Nb^{5+} and Te^{6+} ion, respectively.

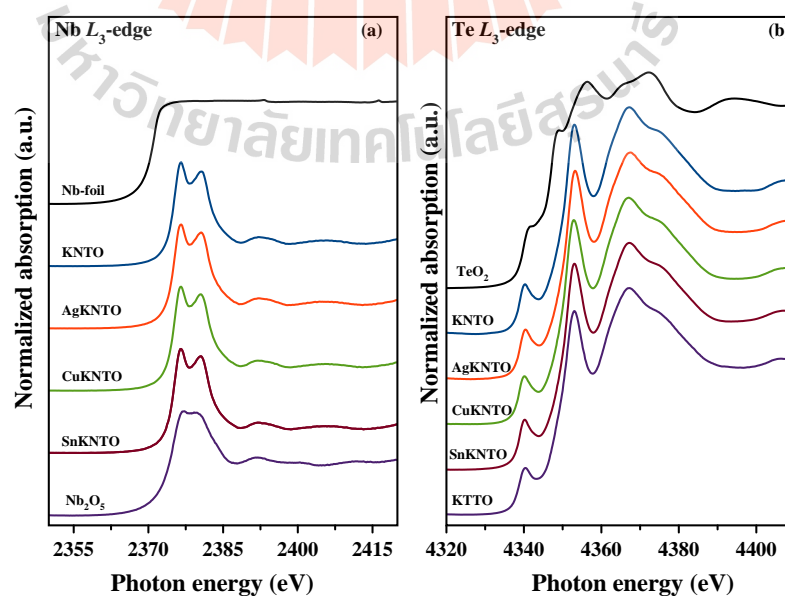


Figure C1 XANES spectra of Nb (a) and Te (b) L_3 -edge.

C2 Photocatalytic test system

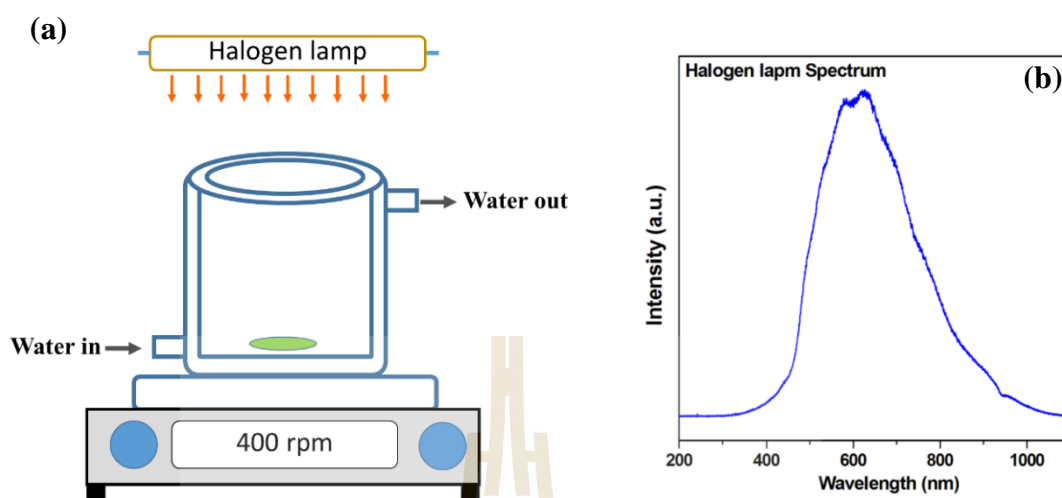


Figure C2 Reactor for photocatalytic test (a) and the spectrum of halogen lamp (b).

C3 UV-Vis spectrum and calibration curve of methylene blue

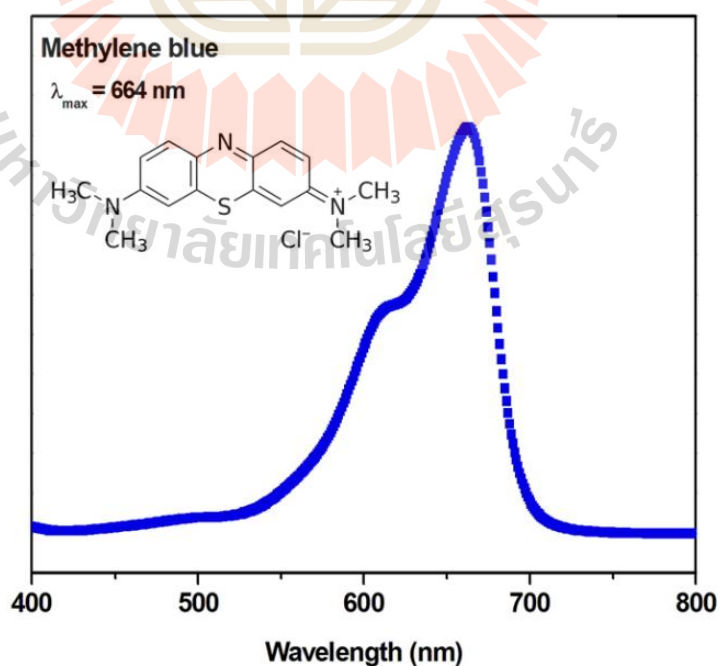


Figure C3 UV-Vis spectrum ($\lambda_{\max} = 664 \text{ nm}$) and structure of methylene blue (inset).

The experiment of MB photodegradation in this work, we tested under light exposure using 150W halogen lamp (Figure C2). The concentration of MB solution was determined by a UV-Vis spectrophotometer with the absorbance at 664 nm and compared with calibration curve (Figure C3).

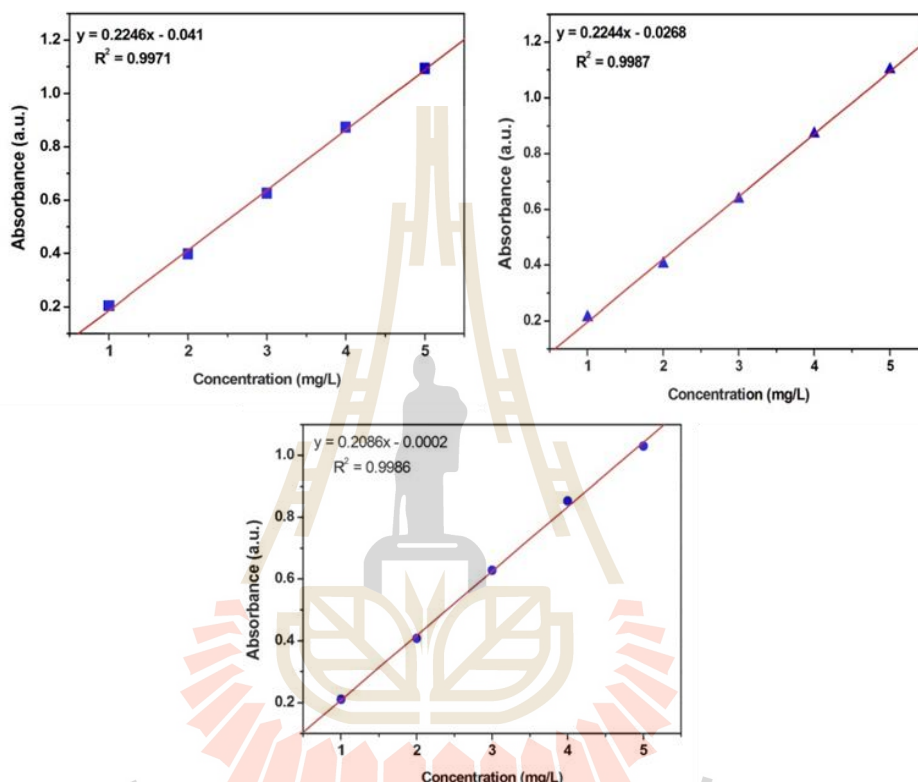


Figure C3 Calibration curve of methylene blue for all three sets of photodegradation.

C4 The \bullet OH radicals generated on photocatalyst

The \bullet OH radicals generated on the irradiated samples were measured by fluorescence spectrometry. To determine \bullet OH radicals generation of photocatalyst, terephthalic acid (TA) was used as an \bullet OH scavenger. Terephthalic acid reacts with \bullet OH to produce highly fluorescent product, 2-hydroxyterephthalic acid, as shown in Figure C4.

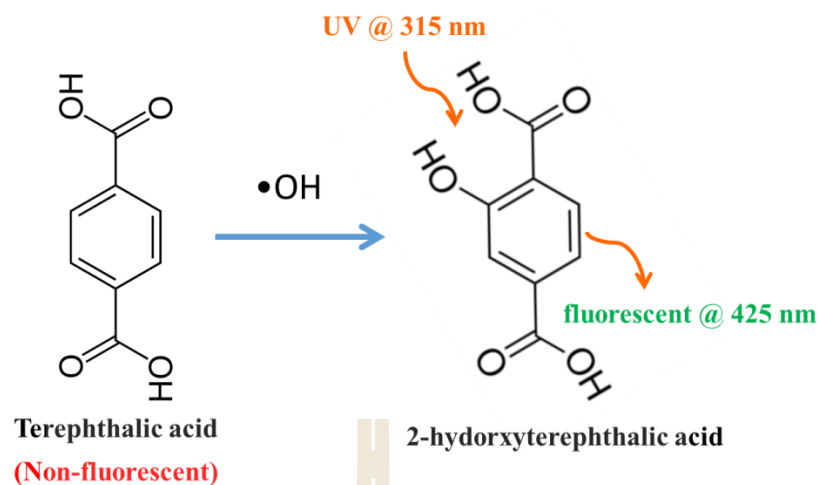


Figure C4 Formation of fluorescent 2-hydroxyterephthalic acid via the reaction of $\bullet\text{OH}$ radicals with terephthalic acid.

References

- Singh, H., Sinha, A., Ghosh, H., Singh, M., Rajput, P., Prajapat, C, and Ravikumar, G. (2014). Structural investigations on $\text{Co}_{3-x}\text{Mn}_x\text{TeO}_6$; ($0 < x \leq 2$); High temperature ferromagnetism and enhanced low temperature anti-ferromagnetism. **Journal of Applied Physics**. 116(7): 074904.
- Wang, B., Zhao, Y., Banis, M. N., Sun, Q., Adair, K. R., Li, R., Sham, T.-K., and Sun, X. (2018). Atomic layer deposition of lithium niobium oxides as potential solid-state electrolytes for lithium-ion batteries. **ACS Applied Materials & Interfaces**. 10(2): 1654-1661.
- Li, J., Ni, G., Han, Y., and Ma, Y. (2017). Synthesis of La doped Bi_2WO_6 nanosheets with high visible light photocatalytic activity. **Journal of Materials Science: Materials in Electronic**. 28(14): 10148-10157.

CURRICULUM VITAE

Name Mr. Anurak Waehayee

Education

2010-2013 B.Sc. (Chemistry) Thaksin University, Thailand

2014-2018 Ph.D. Candidate (Chemistry) at Suranaree
University of Technology, Thailand

Publications

Waehayee, A., Eknapakul, T., Chanlek, N., Kongnok, T., Rattanasuporn, S., Nakajima, H., Meevasana W., and Siritanon, T. (2017). Electrical properties of $(\text{Cs}_{1-x}\text{A}_x)\text{Al}_{0.33}\text{Te}_{1.67}\text{O}_6$ (A = K and Rb) mixed valence pyrochlores. **Journal of Alloys and Compounds**. 718: 215-222. (Impact factor (2017): 3.133)

Waehayee, A., Chanlek, N., Kidkhunthod, P., Nakajima, H., Suthirakun, S., and Siritanon, T. (2019). Electronic band structure and conduction mechanism of mixed valence $\text{Te}^{4+}/\text{Te}^{6+}$ pyrochlore oxides. **Physical Review B**. 100: 045132 (Impact factor (2017-2018): 3.813)